University of Sheffield

Modelling physical location based factors of photovoltaic viability

Author:

Yimin WANG

Department of

Mathematics and Statistics

Supervisors:

Prof. Róbert ERDÉLYI

Prof. Edward HANNA

A thesis submitted to the University of Sheffield for the degree of

Doctor of Philosophy

May 25, 2014

Acknowledgements

Abstract

The aim of this thesis is to model physical location based factors of photovoltaic (PV) viability, including geographical location, dominated climate factors, urban terrain shading and PV panel technologies. We analyze ground measurements from thirteen UK Met Office British weather stations, and ten further weather stations in the US operated by National Solar Radiation Data Base for evidence of climatic effects on annual and seasonal solar radiation over the last 40 years. The impact of the North Atlantic Oscillation on winter solar radiation in the British Isles is explored.

We evaluate the accuracies of four solar radiation models - the PVGIS model, UKCP09 model, Liu and Jordan model and Page model - against ground measurements from these thirteen UK Met Office British weather stations.

A three-dimensional (3D) SOlar RAdiation Model (SORAM) is presented for evaluating the potential direct and diffuse solar radiation aggregated at a point location in an urban area. By using ray-tracing algorithm, SORAM is capable of taking into account terrain shading. We also present a mobile application that has the same aim as SORAM. However, instead of using a 3D city map, the embedded shading detection algorithm is based on image processing.

An analytical model of externally-coated, rectangular and cylindrical luminescent solar concentrators (LSCs) have been developed. These LSCs are able to estimate the residual intensity as a function of wavelength, concentration of luminescent dye and device dimension.

Contents

List of Figures

List of Tables

Chapter 1

Introduction

1.1 Background and brief review

The Sun accounts for, directly or indirectly, almost all of the energy on the Earth (Lang, 1995). Solar radiation such as radiant light and heat from the Sun, together with secondary solar-powered resources such as wind, wave power, hydroelectricity and biomass, has been utilized by humans since ancient times. The most pellucid example could be coal or oil, for which represents sunlight trapped in plants and compressed into fossil fuel many millions of years ago (Lang, 1995).

Solar technologies are generally classified as active or passive, depending on the way they collect, convert and distribute solar energy. Active solar techniques consist of the use of photovoltaic (PV) panels, which is the most common means of capturing the solar energy, and solar thermal collectors. Passive solar techniques include making use of special siting, design or choosing building materials with a favorable thermal mass or light-dispersion properties, and designing spaces that naturally circulate air. Some solar applications achieve space heating and cooling using solar architecture, day lighting, potable water via distillation and disinfection, solar hot water, solar cooking and high-temperature process heating for industrial purposes.

There is an increasing demand for renewable energy, and solar PV is a sustainable

energy source (Pearce, 2002). In this thesis, we focus on the application of solar PV. Solar PV is a method of converting solar radiation into direct current electricity based on the photovoltaic effect. The climate change, locational and technological aspects seriously affect the application of PV. Therefore, the following factors, which are the Sun's property, the Earth's climate system, climate models, solar radiation model and its application to 3-D urban planning and PV module technologies, are investigated at the start of this project.

1.1.1 The Sun

(i) The structure of the Sun and solar activity

The Earth receives about 170 PW of incoming solar radiation (or insolation, i.e. a measure of solar radiation energy received on a given surface area in a given time) at the upper atmosphere (an average throughout the year of 342 W m^{-2}), 31% of which is immediately reflected back into space by clouds, by the atmosphere, and by the Earth's surface (IPCC, 2001). The remaining 235 W m^{-2} is partly absorbed by the atmosphere but most (168 W m^{-2}) warms the Earth's surface: the land and the oceans. Finally, when reaching the Earth's surface, approximately half the 168 W m^{-2} insolation is in the visible part of the electromagnetic spectrum, and most of the other half is in the near-infrared portion, with a small fraction in the near-ultraviolet (IPCC, 2001). The Earth's surface returns that heat to the atmosphere, partly as infrared radiation, partly as sensible heat (i.e. it happens with a change of temperature between bodies) and partly as latent heat (i.e. heat exchange is hidden. For example, during melting of ice, the temperature of the ice and liquid is unchanged until all the ice has melted.).

To look deep down inside the Sun, helioseismology was developed, which uses observations of oscillations in the visible solar gases to detect low-pitched sound waves. As shown in Figure 1.1, the Sun is a massive ball of gas, whose core contains just half the mass, and in about one fifteenth of its volume, but generates 99% of the

energy (Mestel, 1984). The radiative zone encircling the core and occupying up to 71.3% of the Sun's radius, is a relatively quiet region. The energy is then transferred by the turbulent motion of hot gas in the outer convective zone, which lies above the radiative zone. Radiation takes about 1.7×10^5 years, on average to go through from the Sun's core to the overlying convection zone. Beyond the convection zone is the external solar atmosphere, which comprise three different physical layers. The lowest layer is the photosphere (or visible sphere). It is relatively dense, non-transparent and emits most of the visible solar radiation. A thinner and more limpid chromosphere lies above it.
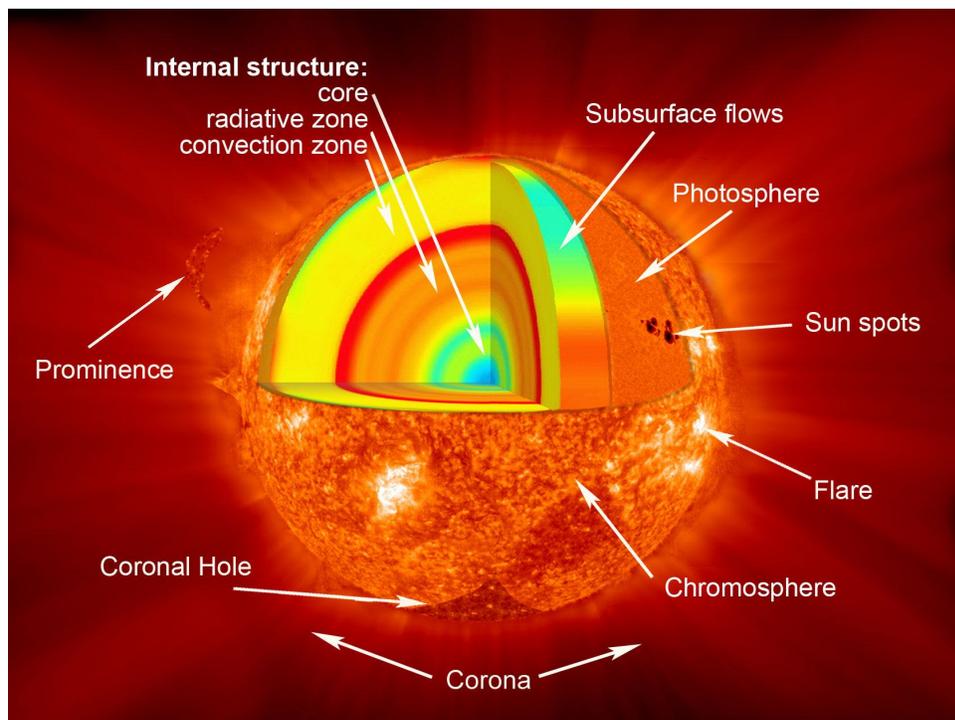
Figure 1.1: Structure of the Sun (Geyserland, 2014)

Sunspots are harbingers of magnetic activity that are often seen within the photosphere. They show up due to the lower temperature than their vicinities, but actually can deliver more energy to the Sun's atmosphere because they are huge vortexes of hot gas, interfering with the terrestrial plasma environment, causing magnetic substorms, auroral activity, and influencing many key aspects of modern society from

telecommunications to the electrical power grid (Lang, 2005). Across the visible solar surface, catastrophic and powerful events can produce transient brightening, called solar flares, which can be observed in the outer space. The source of its energy is believed to be the magnetic field, and it is released by magnetic reconnection (Lang, 2005). The corona, which is made up of plasma, is constructed by closed strong magnetic fields located in the outer solar atmosphere, normally above sunspots. The confined solar atmosphere can abruptly and violently erupt bubbles of gas and magnetic fields called coronal mass ejections (CMEs). A large CME can be composed of a billion tons of plasma and magnetic field that is capable of being accelerated to several million miles per hour (Zell, 2013). Coronal holes are areas where the Sun's corona is darker, cooler and has lower-density plasma than average. These coronal holes are located in open unipolar magnetic fields on the Sun's surface, and extend deep into the solar system. The solar wind, which is a stream of charged particles, is known to travel along these open magnetic field lines, and is composed of electrons and protons that can escape the Sun's gravity due to the corona's high temperature (Hathaway, 2012). It diverts the Earth's magnetic field lines into an elongated cavity, known as the magnetosphere (Bard and Frank, 2006). The Earth's dipolar magnetic field protects us from the Sun's violent activity. Solar energetic particles are high-energy charged particles. When a CME cloud or solar flare are discharged into the solar wind, high-velocity solar energetic particles can be generated. Since these solar energetic particles are charged, they must follow the magnetic field lines that suffuse the space between the Sun and the Earth (Zell, 2013).

(ii) The Sun-Earth connection

Space Weather depicts the dynamic conditions in the Earth's outer space environment, which involves all events on the Sun, in the solar wind, in near-Earth space, in the Earth's upper atmosphere that affect all the technological systems and human life (Zell, 2013).

Solar activity relative to Space Weather can be mainly classified as four compo-

nents: solar flares, CMEs, high-speed solar wind and solar energetic particles (Zell, 2013).

1. Solar flares are constituted of photons. They may impact on the Earth's atmosphere/magnetosphere only when they occur on the side of the Sun facing Earth. Solar flares can emit X-rays and UV radiation that may affect the Earth's ionosphere and long-range radio waves.

2. CMEs can be erupted in any direction and follow that direction. They affect the Earth only when the eruption of the CME cloud is pointing at the Earth. They can result in electrical power blackouts of entire cities;

3. Solar wind is a stream of charged particles, containing mostly electrons and protons. In the direction opposite the Sun, the Earth's magnetic field is pulled way out into space, making it look like a comet. In the tail region of the comet, many different electrical disturbances occur, which can accelerate particles to very high speeds and energies. The solar wind is considered responsible for fluctuations in celestial radio waves observed on the Earth;

4. Solar energetic particles (SEPs) are high-energy charged particles. They consist of protons, electrons, helium ions and HZE ions. SEPs are accelerated at shock waves driven out by fast CMEs. SEPs affect radio transmission and chemistry of the upper atmosphere and ozone layer of the Earth (Reames et al., 2001).

Moreover, since there is a clear effect of space weather on Earth's environment (Zell, 2013), and sunspots are an excellent corollary of extra-terrestrial irradiance (Bigg, 2003), we investigate the relationship between sunspot numbers and solar radiation received on the Earth in Chapter 2 of this thesis.

1.1.2   The Earth climate system

This study aims to delineate the factors that have impact on the variation of solar radiation on the Earth, and to quantify the variation. Global radiation is classified as

the direct, diffuse and ground-reflected radiation on a surface. Direct radiation is the solar radiation received from the Sun without having been scattered or absorbed by the atmosphere. Diffuse radiation is the solar radiation that has been scattered from direct radiation by Earth's atmosphere. As a cloudless sky becomes more turbid, the diffuse radiation increases while direct radiation decreases. Ground-reflected radiation is the radiation received on an inclined surface and reflected from the ground, and is proportional to the global radiation, the mean ground albedo and a fraction of the ground viewed by an inclined surface.

With increasing demand for highly efficient PV technology, we need improved knowledge of all components of the usable solar radiation (global/direct/diffuse radiation) in order to predict and optimise solar PV applications. Not only the global radiation but also diffuse and direct radiation are important for estimating global radiation received on a slope plane surface or a cylindrical solar concentrator that are currently commonly used in industry. This is especially true for places with significant cloud cover, like the UK where diffuse fraction (diffuse over global radiation) ranges from 58% in summer to 69% in winter. The ground-reflected radiation is normally negligible compared with global radiation (HEMI, 2000), so it is therefore ignored in this thesis.

In the Earth climate system, there are a number of factors affecting the amount of global, direct and diffuse radiation. Probably the three most important of these factors are:

1. **Geographic location**- since solar radiation varies largely according to different latitudes, geographic location is a vital factor to consider. For example, in the UK, regardless of month, the south coast area is generally the sunniest place. The highest recorded monthly sunshine total was 384 hours at Eastbourne in July 1911 (Prior and Tempest, 2010). There are on average in excess of 1,850 hours a year of bright sunshine on the south coast of England but less than 1,100 hours across Scotland (Prior and Tempest, 2010);

6

2. **Topography** - this refers to two terms in connection with PV systems: first, reflected radiation is affected by topography through ground albedo, or ground reflectance. Mountains, rivers and snow have quite different albedos. Second, one type of shading problem is caused by topography (another two types are dictated by architectural factors and other collectors in a multi-row array for adjoining rows). For example, most solar power stations are built in desert regions, first because there is normally sufficient solar radiation with little cloud and other shelter such as trees and buildings, and second because such areas normally have unlimited constraints for fixing PV panels. However, it is difficult to find totally unshaded surfaces in urban areas, and this can result in high losses of system performance;

3. **Local meteorology** - besides latitude and longitude, local meteorology may also be affected by local terrain or related topographical features such as oceans, mountains, lakes, vegetation cover and cityscapes. For example, in the UK, it is generally sunnier towards the south of the UK, especially on the eastern side nearest continental Europe, than in the west towards Ireland where North Atlantic weather systems tend to predominate for much more of the time.

In order to find out and show the relationships between the above-mentioned factors and solar radiation, we analyse historical measured data in Chapters 2 & 3. In Chapter 2, we analyze ground measurements from thirteen UK Met Office British weather stations that have long-term record of both global and diffuse radiation, and ten further weather stations in the US operated by the National Solar Radiation Data Base. We investigate the seasonal/annual correlations between global and diffuse radiation. We also evaluate correlations between solar radiation and sunspot numbers and cloud cover conditions that is a major reason for decreasing the amount of direct radiation and a dominant factor on the diffuse proportion (Young and Smith, 1983). Other climatic phenomena have also been investigated. Davy and Troccoli (2012) examined the effect of ENSO (El Niño/La Niña) variability on Australian irradiance

availability. Jerez et al. (2013) considered the influence of North Atlantic Oscillation (NAO) on renewable energy in Southern Europe. Understanding the effect on solar radiation of such planetary-scale oscillations helps reduce uncertainties in PV output prediction. The impact of NAO has been investigated in various areas of power generation and demand (e.g. Ely et al., 2013) as well as in hydrology (Burt and Howden, 2013) or ecology (Zhai et al., 2013). In Chapter 3, we evaluate more closely the relationship between NAO and solar radiation over the UK.

1.1.3 Climate models

Although global radiation data are commonly recorded, direct and diffuse radiation are rarely available due to their high cost; there are, for example, ~ 50 British weather stations currently measuring global radiation over the past few decades, but only thirteen have measured diffuse radiation. Horizontal direct and diffuse radiation data are required for estimating global radiation on a tilted PV module. Moreover, knowing the proportions of direct and diffuse radiation helps develop new PV technology for the optimization of PV yield.

For improving the capability of climate prediction on the Earth, a better understanding of the whole climate system is required, thus climate models appeared. Based on a mathematical approximation, climate models are computer-based simulations used to recreate the chemical and physical processes which can drive Earth's climate (NOAA, 2014). In the late 1960s, National Oceanic and Atmospheric Administration (NOAA) developed the first general circulation climate model, which combined both oceanic and atmospheric processes (NOAA, 2014). Similarly, solar radiation models are used to predict the amount of solar irradiance that can be collected at a location on the Earth. Concerns about the accuracy of solar radiation models have increased due to the recent explosion of interest in renewable and solar electricity generation (Clarke et al., 2007a). Many solar radiation models for evaluating global, diffuse radiation and converting global radiation incident on a horizontal

surface to that received by a sloping surface have been developed.

For decisions on adapting to medium- to long-term climate change (until the 2080s), the UK Climate Projections 2009 (UKCP09) report, which is based on l961-1990 ground measurements, is widely used. Probabilistic projections of climate change were produced as part of UKCP09. Climate projections are used by planners and decision-makers in many impact studies. These projections represent not just the climate itself but also technologies, economics, demography and so on. Models cannot exactly reproduce the real climate system, but there is still enough similarity between them and the real world to provide plausible projections of future climate changes. Each climate scenario produced by the UKCP09 model is supported by evidence, based on current understanding of climate science and observations. Therefore, it is possible to check whether or not the probabilistic estimates of UKCP09 are robust to reasonable variations within these assumptions (Murphy et al., 2009).

Ground-station measurements naturally provide the most accurate solar-radiation data of high temporal resolution, e.g. every fifteen minutes, hourly or daily, but normally with a low spatial resolution. Furthermore, the solar radiation sensor may be covered with dirt, frost or snow or shaded by obstacles like buildings and/or trees (PVGIS, 2010). Therefore, the method of solar radiation estimation using satellites has been developed by PVGIS (2010), based on 1998-2010 measurements. The idea is that the satellites measure extraterrestrial irradiance, from which is subtracted: (i) both the visible and infrared light reflected by the Earth and clouds, which are measured by the satellite as well; and (ii) the parts absorbed by the atmosphere and clouds, which are not easily derived from satellite observations and are thus estimated using radiative transfer models (Kiehl and Trenberth, 1997). Problems and biases of the satellite method include snow cover, varying terrain in mountain areas and low Sun angle (PVGIS, 2010).

Many hourly and monthly solar radiation models have been evaluated in Noorian et al. (2008), Perez et al. (1990b), Ineichen (2008) and Rehman (1999). We validated four typical monthly solar radiation models for retrieving both global and diffuse

radiation including the UKCP09 and PVGIS models, as well as two regression models, which are the Liu and Jordan (1962) and Page (1961) models in Chapter 4. We choose both ground-based (UKCP09) and satellite-based (PVGIS) models. These two models can be used to simulate both global and diffuse radiation. We also chose the widely used Liu and Jordan (1962) and Page (1961) models, which can only provide diffuse radiation based on the given global radiation, for comparison with the UKCP09 and PVGIS models.

1.1.4 Solar radiation model and its application to 3-D urban planning

The above-mentioned solar radiation models do not take into consideration the effects caused by urban shading, such as buildings and trees. However, a sustainable city is required to generate a large part of its energy consumption from renewable energy sources. Large-scale PV solar-energy installations are considered to be a potential solution for future cities (Hofierka and Kanuk, 2009). PV systems connected to the electricity grid can help with peak shaving, minimize transmission and distribution losses (da Silva Jardim et al., 2008). Besides the effective solar irradiance, terrain shading also has an important impact on the efficiency of PV modules (Melo et al., 2013). Several solar-radiation software tools, models and algorithms have been established, e.g. ArcGIS (2012), Šuri and Hofierka (2004), Hofierka and Zlocha (2012), PVSYST (2013), PV*Sol (2013), Perpinan (2012), Navarte and Lorenzo (2008), Lorenzo et al. (2011), Fartaria and Pereira (2013), Melo et al. (2013), Redweik et al. (2013), Orioli and Gangi (2012) and Yoo (2011). They all have certain limits as described in Chapter 5, where we construct a Three-dimensional (3D) SOlar RAdiation Model (SORAM) to overcome those limits. By providing the 3D coordinates of obstacles (e.g. the positions and heights of all buildings and trees) in an area, SORAM can predict the amount of solar radiation received at any position within the area, taking into account terrain shading and any given slope and azimuth of a PV module. A

ray-tracing method is used in SORAM to determine whether a solar ray (direct or diffuse) can reach a PV cell location in this area (Shirley et al., 2005; Mena-Chalco, 2010). The well-known Perez et al. (1990a) model has been adapted to include the contribution of each diffuse ray. Moreover, SORAM can also calculate the optimal slope and azimuth of PV installations.

Although SORAM can aid the optimisation of large-scale PV installations (e.g. city-wide), it requires the 3D coordinates of obstacles to be specified. Without this information, for a location of interest, an image-processing based method can be applied. Quaschning and Hanitsch (1998) and Orioli and Gangi (2012) have developed methods that can evaluate the surroundings of a PV module by describing the terrain-shading profile. A Shading Detection Algorithm (SDA) based on image processing for estimating terrain shading conditions of a PV module is developed in Chapter 6. We then combine SDA and SORAM to develop an complete working app that is applicable to use on a smart phone. We also validate our results from SORAM and this mobile app against the Perez et al. (1990a) model, and against the global radiation measurement from pyranometers surrounded by real urban obstacles.

1.1.5 PV module technologies

A PV panel or PV module is a packaged interconnected assembly of solar cells that converts light (solar radiation) into electric current based on the photoelectric effect. The most commonly used material nowadays for PV panels are typically categorized into mono-crystalline, multi-crystalline and thin-film (the latter consists of both amorphous and microcrystalline silicon film). These three kinds of material are listed in order of both cost and efficiency from high to low. Thus cost and performance needs to be compromised depending on the required usage: e.g. cost may play a major role in home use while performance predominates when PV panels are used in satellites due to limited space and the extremely high cost of failure. Moreover, mono-crystalline and multi-crystalline silicon PV modules are normally used

for rooftop panels because they need sufficient sunshine to be trigged. On the other hand, amorphous silicon PV modules can be installed on vertical walls since they are relatively less demanding for sunshine.

Solar panels made from mono-crystalline or poly-crystalline silicon typically have an average efficiency of 14%, with the best commercially available panels at 20%. In Europe, a typical insolation ranges from 2 kWh m^{-2} per day in northern climates to 6 kWh m^{-2} per day in the sunniest regions, as shown in Figure 1.2 (EEA, 2007). Thus, an installation of a typical power of 150 W solar panel, of about a square meter in size, is expected to produce 150 W × 6-7 hrs (where 6-7 hrs means the daily sunshine duration) or approximately equal to 1kWh m^{-2} every day on average.
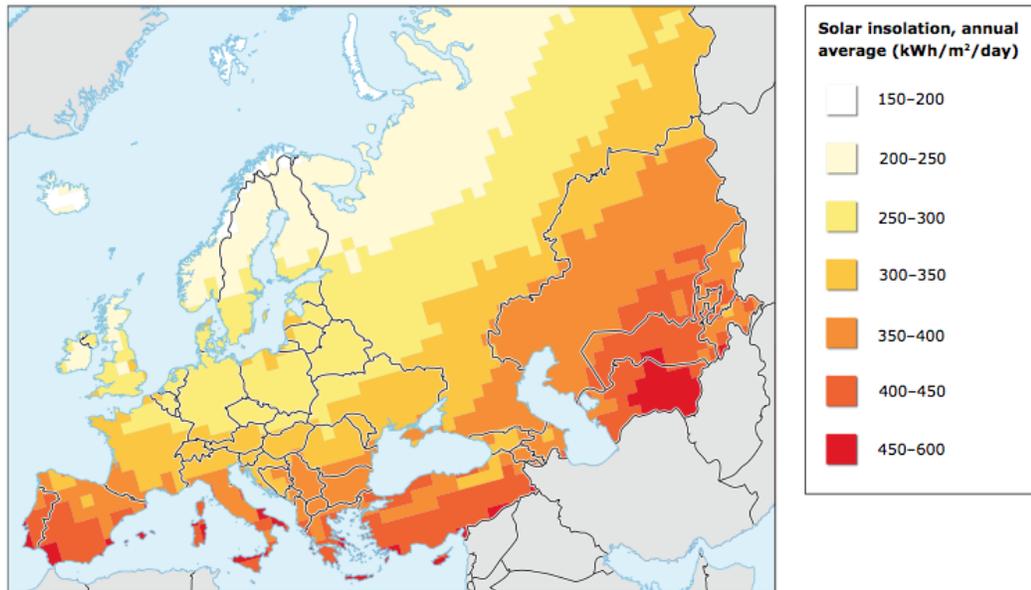
Figure 1.2: Annual average solar insolation in Europe (EEA, 2007)

Modern solar PV panels were first developed commercially for NASA and the space race in the 1950's. With no moving parts, solar PV is a silent and reliable method of producing electricity in remote locations. Up to 2010, more than 100 countries have used the electricity generated by solar PV, which is the fastest growing power-generation technology in the world. Between 2004 and 2009, grid-connected PV capacity increased at an annual average rate of 60%, about 21 GW of annual

increase in capacity (REN21, 2010). Such installations can be ground-mounted (may be integrated with farming and grazing) or built into the roof or walls of a building, referred to as Building Integrated Photovoltaics (BIPV). Off-grid installations occupy another $3-4$ GW (REN21, 2010). Thanks to the developing technology and manufacturing improvements, the cost of the material of PV panels has reduced significantly since the first solar cells were made (Swanson, 2009). Net metering and financial incentives, for example, Feed-In Tariffs (FITs) in the UK, have supported solar PV applications in many countries.

In order to reduce the cost of the PV conversion of sunlight, luminescent solar concentrators (LSCs), which are a hybrid amorphous silicon and mono-crystalline (or poly-crystalline) silicon, are introduced and investigated. These can potentially convert a wide spectrum of solar energy to electricity using highly efficient PV cells. The LSC host material may be any shape of plastic doped with luminescent dye. Proper selection of the luminescent dye species and positions results in efficient matching of the spectrum of the concentrated solar beam to the maximum sensitivity wavelength area of the PV cells applied. The LSCs are much less expensive than a conventional module because the solar cells which mainly made from silicon are located just on its edges rather than the whole collecting face, and so these cells reduce the cost of a conventional module by up to 70%. However, LSCs are not yet commercially viable because their optical efficiency remains too low and they are photochemically unstable (McIntosh et al., 2007).

For the main principle of the LSCs, first an incident ray is transmitted into the plastic and absorbed by the luminescent dye molecules, which emit luminescent light in all directions. Then a significant portion of the photons of the ray can be emitted at a sufficiently oblique angle to be totally-internally reflected at the plastic interface and be led toward the edges as the refractive index of the plastic is much higher than that of the external medium, normally air. Finally, the luminescent photons are absorbed and their energy is converted into electricity by a PV cell (Soti et al., 1996). In Chapter 7, we develop numerical spectral-based simulation of rectangular

and cylindrical 2-layer luminescent solar concentrators. We also evaluate four types of luminescent dye, four concentrations of dyes, different lengths of concentrator and five solar cells.

1.2 Aims and objectives

To perform the study of modelling physical location based factors of photovoltaic viability, specific research aims have been identified below:

Aims 1: To analyse the observed solar radiation data of the recent 30 years in UK and US associated with sunspot numbers, cloud cover and NAO index. Predominant factors that affect global and its components diffuse and direct radiation are explored, taking into account variations in geographic location and local meteorology. The relationships between solar radiation and sunspot numbers, cloud cover and the NAO index are investigated.

Aims 2: To build a solar radiation model. A 3D mathematical SOlar RAdiation Model (SORAM) is developed to predict solar radiation (global, diffuse and direct radiation) incident on each point of an urban area, and to evaluate terrain shading based on a ray-tracing algorithm.

Aims 3: To embed SORAM into a smart phone. Instead of ray-tracing algorithm, construct an algorithm for evaluating shading conditions by image processing. The software typically consists of a user friendly interface, and requires a database of solar radiation to be invoked. The inputs of the software are designated latitude, the type of technology of the PV panels, elevation and azimuth of the PV panels and shading conditions; the output is the solar radiation to be obtained and the converted electricity of this particular location by month, season or year depending on the choice made.

Aims 4: To build a mathematical model to predict/optimise photon flux gain out of two-layer rectangular and cylindrical luminescent solar concentrators (LSC) based on the visible spectrum. Four luminescent dyes

and various concentrations of these dyes are analysed and reported. Length and solar cells attached at the edges of LSCs have also been investigated.

1.3 Outlines of the Thesis

This thesis is composed of eight chapters. Following the contents page, Chapter 1 is the introductory chapter, which gives the background, objectives and outlines of this thesis. The main work of the thesis is presented in Chapters 2-7. Finally in Chapter 8, conclusions are drawn and suggestions are given for further work.

In Chapter 2, the observed solar radiation data in UK and US for the recent decades are analysed together with sunspot numbers and cloud cover conditions. The NAO index, which is the local meteorology affecting UK's solar radiation distribution is investigated in Chapter 3. In Chapter 4, four solar radiation models, which can supply global/direct/diffuse radiation data, are evaluated. In order to accurately evaluate terrain shading, daily solar radiation data are not sufficient. Hourly or sub-hourly solar radiation data are required. Therefore, a solar radiation model called SORAM is constructed and described in Chapter 5. In Chapter 6, a shading detection algorithm based on image processing is developed. This algorithm is then combined with SORAM to form a complete application that can be used on a smart phone. In Chapter 7, LSCs is investigated for the optimization analysis. The Sun-Earth and Sun-PV-module trigonometric relationships can be found in the Appendices A-D. My publications are displayed in Appendix E.

Chapter 2

Climate change

Abstract

Horizontal direct and diffuse radiation data are required in order to estimate hourly/monthly global radiation on a given tilted surface and for optimizing the structure of a range of photovoltaic (PV) panels. Although global radiation data are commonly measured, direct and diffuse radiation data are not readily available due to their high cost; there are, for example, about 50 British weather stations currently reporting global radiation over the past few decades, but only three and thirteen have recorded direct and diffuse radiation, respectively.

We analyze ground measurements from these thirteen UK Met Office British weather stations that have recorded diffuse radiation, and ten further weather stations in the US operated by National Solar Radiation Data Base (NSRDB) for evidence of climatic effects on annual and seasonal solar radiation over the last 40 years. We found the British diffuse and US global/diffuse/direct radiation correlate significantly with - although show much greater ($\sim$ 77 times) amplitude than - the 11-year solar cycle, while British global/direct radiation do not show such a correlation. The greater amplitude indicates a large modulation of solar radiation by cloud cover.

This work has been submitted to the *Journal of Climate* (Wang et al., 2014c). The authors are: Yimin Wang, Edward Hanna and Róbert Erdélyi.

2.1 Introduction

Global solar radiation received on a horizontal surface is the sum of the direct, diffuse and ground-reflected radiation. The ground-reflected radiation at a location from surrounding topographic features is trivial compared with global radiation and is therefore ignored in this study (HEMI, 2000).

Modelling the effects of direct radiation (i.e. that part of the solar radiation which propagates straight through to the Earths surface) is considered more straightforward than modelling diffuse or global radiation, because the direct component is readily defined from the position of the Sun (solar declination, hour angle) relative to the surface (latitude, slope of surface, azimuth angle), and this can be expressed in straightforward geometric terms (Benford and Bock, 1939). However, energy is redistributed from direct radiation to the diffuse component as a result of absorption and dispersion processes and clouds in the atmosphere (Myers, 2003). Therefore, the same factors making the modelling of diffuse or global radiation complex also act on the direct radiation.

Regarding global radiation, concerns are mainly focused on the solar irradiance in the wavelength (λ) range of 0.25 to 3.0 μm, which is primarily composed of visible (0.38 μm $< \lambda <$ 0.78 μm) and the infrared ($\lambda > 0.78\mu$m) parts of the spectrum, because this contains most of the energy radiated by the Sun (Duffie and Beckman, 1991). Cloud cover (via absorption and reflection) is a major reason for the reduction of the amount of direct radiation, and is the dominant factor on the diffuse proportion (Young and Smith, 1983). In Britain, just a few weather stations measure diffuse radiation (BADC, 2012), so a detailed spatial analysis is difficult.

We analyse annual- and seasonal-average data of ground-observed solar (global, diffuse and direct) radiation, and attempt to explain their pronounced variations over

time through comparisons with solar activity and cloud-cover data.

2.2 Methodology and dataset

Changes in annual/seasonal global and diffuse radiations are studied based on observed data from 1952-2010 for thirteen British weather stations and 1961-2005 for ten US weather stations.

Global radiation for both British and US weather station is measured using a pyranometer mounted horizontally facing upwards; diffuse radiation is measured by a horizontally mounted pyranometer shaded from the direct radiation from the Sun. The ring shades the pyranometer from part of the diffuse radiation, and a correction for this shading is necessary (Steven and Unsworth, 1980).

All the weather stations used in this chapter are in rural areas, meaning that urbanization is unlikely to have a significant impact on our results.

2.2.1 UK Met Office weather stations

The British in situ radiation data used in this project are from the UK Met Office (UK Meteorological Office, 2006). Weather-station metadata are given in Table 2.1, and their locations are shown in Figure 2.1.

The Baseline Surface Radiation Network (BSRN) sensors at Camborne and Lerwick are mounted on trackers which follow the Sun and use shading balls to shade the domes: as these balls only block the Sun and not an additional part of the sky, there is no shade ring error for these two weather stations diffuse radiation data.

The standard Met Office shade ring dimensions are width 50 mm and radius 254 mm. Steven and Unsworth (1980) found that the shade-ring correction (depend on latitude and time of year) improves the clear-sky shade ring error. After correction, the errors range from $\sim 9\%$ to $\sim 30\%$. Actual figures for the correction factors applied for each station are available from Met Office Quality Control section in Edinburgh,

Figure 2.1: Locations of British weather stations and their regions: NScot is north Scotland; SScotNIre is south Scotland and north Ireland; NW Eng is northwest England; NE Eng is northeast England; SE Eng is southeast England; and SW Eng & Jersey is southwest England and Jersey.

Table 2.1: British weather stations measuring solar radiation that were used in this study, including station ID number, name, geographic area, latitude, longitude, elevation and periods of record of diffuse solar radiation.

Station ID	Station name	Geographic area	Latitude (deg)	Longitude (deg)	Elevation (m)	Period
9	Lerwick	Shetland	60.14	-1.18	82	1952/01-2009/12
54	Stornoway Airport	Western Isles	58.21	-6.32	15	1982/10-1996/12
433	Hemsby	Norfolk	52.69	1.69	13	1981/04-1996/12
435	Brooms Barn	Norfolk	52.26	0.57	75	1982/04-1999/10
554	Sutton Bonington	Nottinghamshire	52.84	-1.25	43	1983/04-1998/12
562	Finningley	South Yorkshire	53.48	-1.01	10	1982/11-1995/09
744	East Malling	Kent	51.29	0.45	33	1982/07-1997/12
1023	Eskdalemuir	Dumfriesshire	55.31	-3.21	236	1956/01-2002/12
1096	Aughton	Lancashire	53.55	-2.91	54	1981/11-1996/03
1105	Hazelrigg	Lancashire	54.01	-2.77	95	1982/07-1997/12
1395	Camborne	Cornwall	50.22	-5.33	87	1989/04-2009/12
1450	Aldergrove	Antrim	54.66	-6.22	63	1968/10-1999/12
1575	Jersey: Airport	Jersey	49.21	-2.20	84	1968/01-2005/11
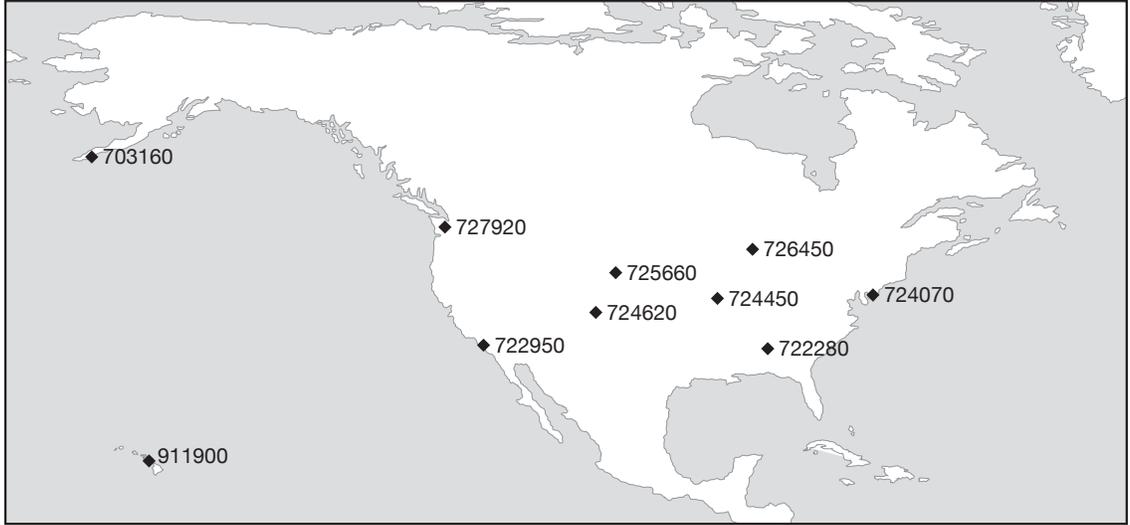
Figure 2.2: Locations of US weather stations used in this study.

UK (Met. Office, pers. comm. 2012).

2.2.2 US National Solar Radiation Data Base (NSRDB)

We summarise details of the US weather stations used in this study in Table 2.2, and show their locations in Figure 2.2.

When all three of the solar radiation elements are available (global, direct and diffuse radiation), redundancy can be used to further reduce the uncertainty of the data. This is accomplished by calculating the global component from the direct normal and diffuse ones,

$$K_{tc} = K_n + K_d \tag{2.1}$$

and by comparing the calculated global radiation (K_{tc}) with the measured global radiation (K_t). This comparison provides a direct indication of the accuracy of all three measurements. It is possible that offsetting measurement errors could partially invalidate this comparison. Nevertheless, when hourly values of global horizontal, direct normal, and diffuse horizontal agree within a specified error limit, the lowest

Table 2.2: US weather stations measuring solar radiation that were used in this study, including station ID number, name, geographic area, latitude, longitude, elevation and periods of record of solar radiation. There are two columns in Station ID. The first column is for the record 1961-1990 and the second column 1991-2005.

Station ID	Station name	Geographic area	Latitude (deg)	Longitude (deg)	Elevation (m)	Period
13876/722280	Birmingham	Alabama (Region F)	33.57	86.75	192	1961-2005
25624/703160	Cold Bay	Alaska	55.20	162.72	29	1961-2005
23174/722950	Los Angeles Intl Arpt	California (Region D)	33.93	118.40	30	1961-2005
22516/911900	Kahului Intl Arpt	Hawaii	20.90	156.43	15	1961-2005
03945/724450	Columbia Regional Airp	Missouri (Region E)	38.82	92.22	272	1961-2005
93730/724070	Atlantic City Intl Arpt	New Jersey (Region C)	39.45	74.57	18	1961-2005
14898/726450	Green Bay Austin Straubel Int	Wisconsin (Region B)	44.48	88.13	209	1961-2005
24227/727920	Olympia Airport	Washington (Region A)	46.97	122.90	63	1961-2005
23061/724620	Alamosa San Luis Valley Rgnl	Colorado (Region D)	37.43	105.87	2296	1961-2005
24028/725660	Scottsbluff W B Heilig Field	Nebraska (Region B)	41.87	103.60	1202	1961-2005

possible uncertainty for solar radiation data can be assigned.

The results of the work of Myers et al. (1989) and Wells (1992) yielded the following optimum uncertainties for the measurement of the three major elements of solar radiation using thermopile pyranometers and pyrheliometers: the error of global horizontal is $\pm 5\%$, direct normal is $\pm 3\%$ and diffuse horizontal is $\pm 7\%$.

2.2.3 Statistical data analysis

The observed annual mean daily solar radiation used in this thesis are computed from monthly averages based on daily values for at least 20 days within each month.

All correlation and wavelet analysis results are evaluated according to the 95% confidence level. 5-point running means were used to smooth the annual observed data in order to highlight important low-frequency patterns.

Relationships of global, diffuse and direct radiation with solar activity, solar irradiance and cloud cover conditions are explored using correlation and wavelet analyses.

2.3 Variation of solar radiation and climate change

2.3.1 British global/diffuse radiation and cloud cover

Figure 2.3 shows annual average daily diffuse fractions (diffuse over global radiation) for various British weather stations from the observed data. From this figure, we can see that the diffuse fractions decrease during spring and summer, while they increase during autumn and winter. An averaged diffuse fraction of British weather stations seasonally ranges from $64 \pm 8\%$ in summer to $79 \pm 4\%$ in winter (8% and 4% are standard deviation for British weather stations used in this study), due to often-prevailing cloud cover in this predominantly maritime climate, making proper consideration and modelling of diffuse radiation particularly important for British PV system development. The diffuse fractions for the US weather stations range on average from $49 \pm 15\%$ in summer to $43 \pm 15\%$ in winter, reflecting the more

Table 2.3: Correlation coefficients (r values) between annual/ seasonal diffuse and global radiation, with significant ($p \leq 0.05$) correlations denoted in bold.

Station ID	Geographic area	Winter	Spring	Summer	Autumn	Annual
9	Shetland	**0.60**	**0.41**	**0.28**	0.16	**0.27**
54	Western Isles	**0.66**	-0.07	0.52	0.27	**0.81**
433	Norfolk	**0.86**	0.18	0.19	0.13	**0.62**
435	Suffork	**0.76**	-0.01	-0.08	0.48	0.32
554	Nottinghamshire	0.62	0.25	-0.08	0.06	-0.10
562	South Yorkshire	**0.62**	0.44	0.20	**0.84**	**0.75**
744	Kent	**0.83**	-0.27	0.02	-0.06	-0.29
1023	Dumfriesshire	**0.77**	**0.34**	**0.29**	**0.73**	**0.32**
1096	Lancashire	**0.72**	0.13	0.30	-0.30	0.50
1105	Lancashire	0.86	**0.59**	0.25	-0.09	**0.64**
1395	Cornwall	0.34	-0.34	-0.10	-0.11	0.45
1450	Antrim	**0.51**	**0.49**	-0.21	0.23	0.01
1575	Jersey	**0.48**	-0.32	0.25	**0.76**	0.26

continental climate.

To understand the relationship between global radiation and its diffuse component in Britain, we use correlation analysis. Correlation coefficients (r values) for available periods of record for various British weather stations, with significant values highlighted, are summarized in Table 2.3, where winter, spring, summer and autumn denote December to February, March to May, June to August, and September to November respectively. 92% of the weather stations have a statistically significant correlation between the global and diffuse radiation in winter. The global-diffuse radiation relation is generally much weaker in the other three seasons and for annual values. This is consistent with the result inferred from Figure 2.3, which shows that the diffuse radiation fraction is greater in winter.

To understand why British global and diffuse radiation are most strongly correlated in winter, we consider that weather conditions tend to be cloudier on average during winter (cf. Figure 2.3) and Prior and Tempest (2010). We computed the correlation between global (or diffuse) radiation and cloud cover for four British weather stations, which have recorded both radiation and cloud-cover data for substantial coincident time periods, with significant values highlighted (Table 2.4).
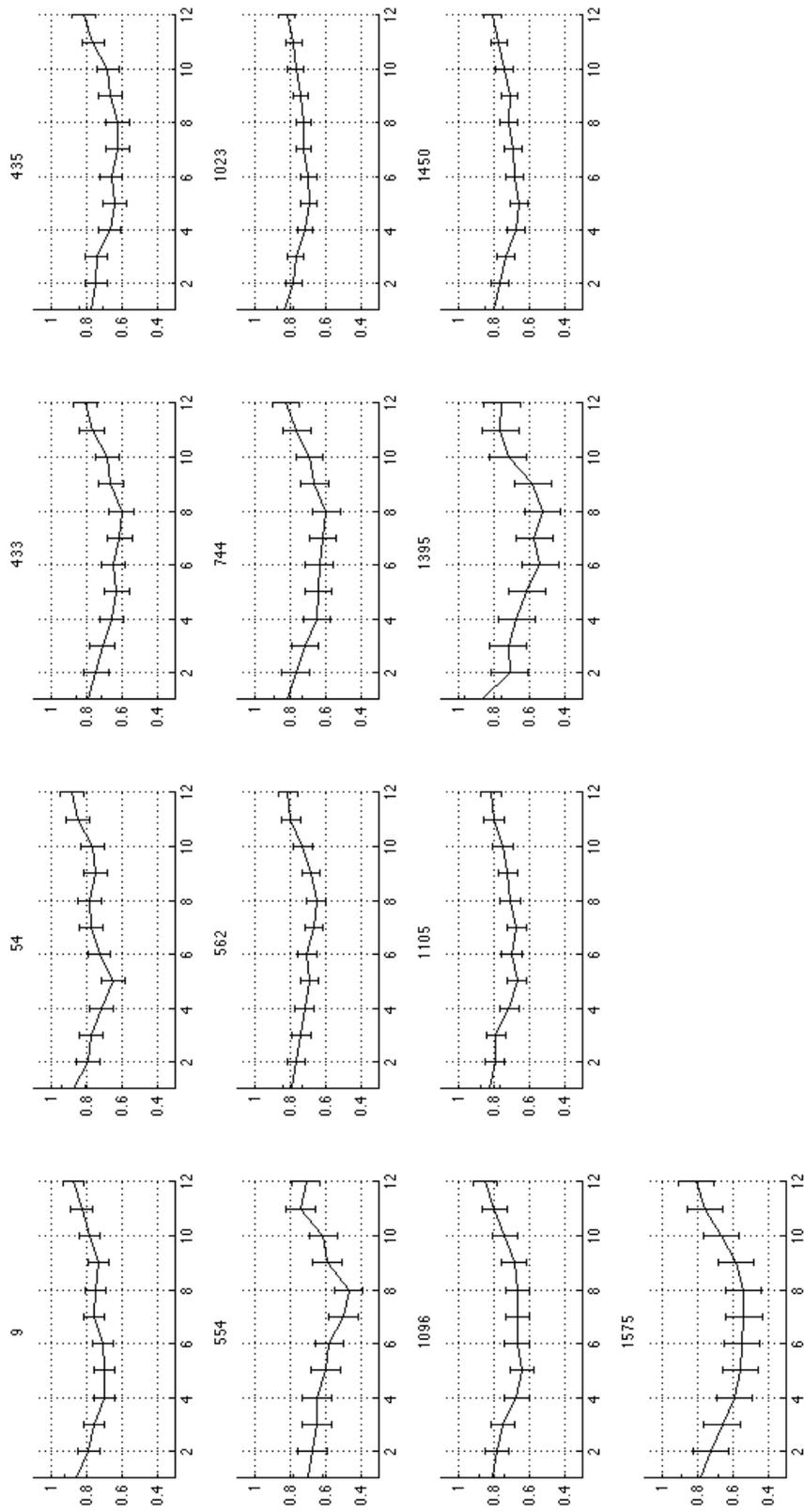
Figure 2.3: Diffuse fractions (y-axis) observed at various British weather stations for each calendar month (x-axis). The solid line depicts data for 1952-2010, and the vertical error bars represent the standard deviation of the individual annual values..

25

Table 2.4: Correlation coefficients (r values) between British annual/seasonal global (or diffuse) radiation and annual/seasonal cloud cover, with significant ($p \leq 0.05$) correlations denoted in bold.

Station ID	Global Radiation						Diffuse radiation			
	Global	Diffuse	Winter	Spring	Summer	Autumn	Winter	Spring	Summer	Autumn
9	**−0.49**	-0.03	**−0.55**	**−0.76**	**−0.88**	**−0.77**	**−0.41**	-0.13	**−0.53**	-0.42
435	**−0.94**	-0.17	**−0.70**	**−0.91**	**−0.92**	**−0.82**	**−0.79**	0.07	-0.09	-0.20
554	**−0.67**	0.20	**−0.48**	**−0.90**	**−0.85**	**−0.80**	-0.38	-0.32	0.51	0.09
1575	**−0.78**	-0.15	**−0.82**	**−0.86**	**−0.89**	**−0.70**	**−0.52**	-0.11	0.21	0.11

We found strongly significant negative correlations between annual/seasonal British global radiation and annual/seasonal cloud cover; we also found that three quarters of the tested weather stations have a statistically significant correlation between diffuse radiation and cloud cover in winter. The relation between diffuse radiation and cloud cover is generally much weaker for the other three seasons and annual values. When we calculated the correlation coefficients for Lerwick weather stations (Station ID: 9) and Jersey weather station (Station ID: 1575) in Table 2.4, the time periods of global, diffuse radiation and cloud cover data were kept the same. However, for Brooms Barn weather station (Station ID: 435) the correlation between diffuse radiation and cloud cover is based on a shorter period than that between global radiation and cloud cover, and is therefore not directly comparable. By comparing the correlation coefficients for Lerwick and Jersey weather stations in Table 2.4, we found that the relation between global radiation and cloud cover is stronger than that between diffuse radiation and cloud cover. Scatter plots between cloud cover and global/diffuse/direct/diffuse fraction are produced as shown in Figure 2.4. In Figure 2.4 (a) and (c), we found global/direct radiation negatively correlate with cloud cover. As to diffuse radiation in Figure 2.4 (b), we can see a negative relation trend between diffuse radiation and cloud cover in winter, but not in the other three seasons. Figure 2.4 (d) shows a positive correlation between diffuse fractions and cloud cover. This positive trend is especially strong during summer, meaning that when cloud cover increases during summer, the proportion of diffuse component out of global radiation increases; however, the actually amount of diffuse radiation does not necessarily increase.

Therefore, combining the results of the analyses in Tables 2.3, 2.4 and Figure 2.4, we infer that during winter, when cloud cover increases, global/diffuse/direct radiation decrease. Global/direct radiation is mainly affected by cloud cover; on the other hand, diffuse radiation may also be affected by other influences including, for example, changes in atmospheric aerosol concentration (Mercado et al., 2009). Liepert and Tegen (2002) found that sulphate aerosols mainly scatter solar radiation without significantly decreasing global radiation; Ramanathan et al. (2001) found that oceanic
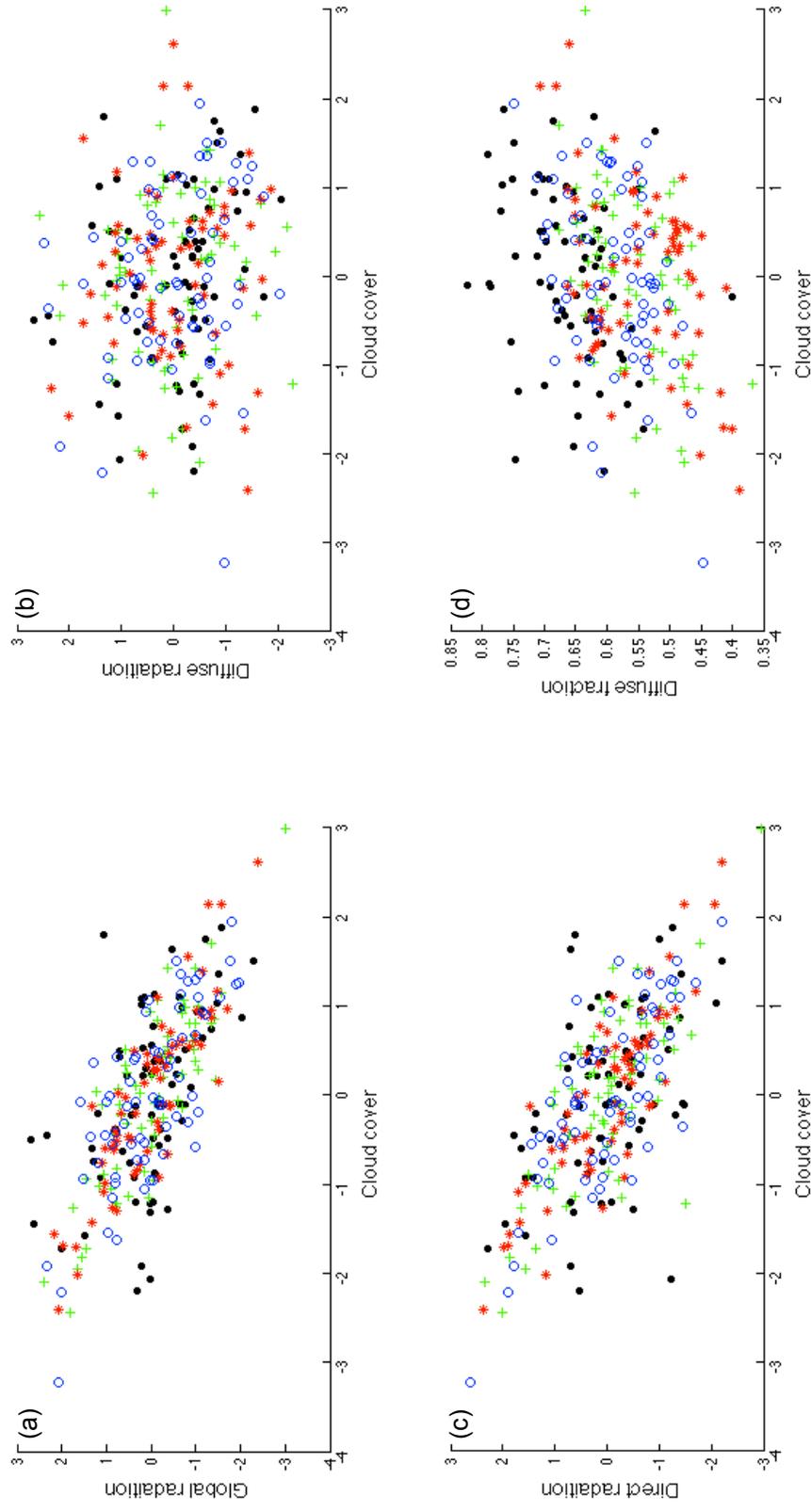
Figure 2.4: Scatter plots between normalised cloud cover and normalised global/diffuse/direct/ real diffuse fraction. The data used here are the same as in Table 2.4. Black dots, green plus marks, red stars and blue circles represent winter, spring, summer and autumn, respectively.

28

aerosols contain relatively large non-absorptive particles that result in forward scattering. Therefore, both of these two types of aerosol produce large quantities of diffuse radiation without significantly modifying global radiation. These findings should be explored as part of future work.

2.3.2 Effect of solar activity and cloud cover

In Table 2.5 , inter-annual variability of British global radiation as expressed through standard deviation is greatest in summer and least in winter, but using the coefficient of variation (i.e. scaling standard deviation by the mean radiation values for each month) shows that there are proportionately greater (lesser) climatic variations during winter (summer). Similar analysis is done for British diffuse radiation, which shows that this effect is more pronounced for diffuse radiation. This is most likely related to greater winter fluctuations in atmospheric air mass and circulation, e.g. jet stream, storminess and North Atlantic Oscillation (NAO) changes, affecting the British climate in winter (Hanna et al., 2008). NAO changes are discussed in the next chapter.

For the purposes of this analysis, it is assumed that sunspot numbers are an excellent corollary of extra-terrestrial irradiance (Bigg, 2003). A periodic fluctuation of around ten years can be seen for some of the weather stations that with sufficiently long-term records, as shown in Figure 2.5 (b-d). On one hand, British and US diffuse radiation generally lags (comes after) the sunspot numbers by about 1-2 years (Figure 2.5 (b),(d) and Table 2.6). On the other hand, US global/direct radiation tends to lead (comes before) sunspot numbers (Figure 2.5 (c) and Table 2.6), but no such correlations happen between British global/direct radiations with sunspot numbers (Figure 2.5 (a) and Table 2.6). Both the lag and lead are obvious especially during the central parts of the time series: this may caused by the 5-year running mean introducing an edge effect at the beginning and end of the time series. The correlation shown in Table 2.6 are produced using 5-year running mean and based

Table 2.5: Annual and seasonal means, standard deviation and coefficient of variation (CV) of global radiation for all tested British weather stations. All mean values are in unit of Wh m^{-2}.

Station	Annual		Winter		Spring		Summer		Autumn	
	Mean	St dev	Mean	St dev	Mean	St dev	Mean	St dev	Mean	St dev
9	2149.1	116.4	394.6	54.3	3029.3	234.3	3945.9	272.3	1163.4	107.2
54	2245.6	103.5	500.7	47.2	3277.1	187.8	3844.1	372.5	1258.5	160.2
433	2812.8	206.8	836.6	60.8	3770.0	340.8	4896.7	373.3	1809.5	92.5
435	2738.6	148.1	843.4	64.9	3509.8	304.8	4619.4	331.3	1807.8	122.1
554	2560.5	162.2	776.3	93.9	3227.8	282.0	4347.0	349.1	1691.1	169.4
562	2588.4	205.2	770.2	41.4	3275.5	291.8	4438.5	372.5	1646.9	136.5
744	2763.0	162.7	829.7	97.3	3540.2	289.8	4374.3	374.4	1897.6	157.6
1023	2255.8	136.5	621.9	100.2	3058.7	291.3	3892.3	352.7	1398.0	157.5
1096	2643.3	133.0	738.6	44.1	3525.2	252.1	4549.9	359.6	1668.2	120.4
1105	2556.5	173.3	705.4	61.2	3418.5	255.9	4479.9	330.0	1601.6	111.6
1395	2992.9	188.3	971.8	77.4	3932.4	277.4	5004.1	376.9	2053.7	121.0
1450	2505.7	153.3	693.1	57.2	3443.0	256.8	4273.4	325.9	1573.5	78.6
1575	3182.2	174.7	1032.0	98.1	4145.8	297.8	5380.1	449.4	2111.9	305.3
MEAN	2607.3	158.8	747.3	69.1	3473.3	274.0	4492.7	356.9	1667.9	141.5
CV (%)	6.08		9.53		7.91		7.97		8.56	

Table 2.6: Correlation coefficients (r values) between annual average daily global and diffuse radiation in Britain (1952-2010)/ US (1961-2005) and sunspot numbers, with significant ($p \leq 0.05$) correlations denoted in bold. "0" in the first row means no shift year, "-1" means solar radiation shifts one year advance with respect to the sunspot numbers, "1" means solar radiation shifts one year after the sunspot numbers et al.

	-3(yrs)	-2(yrs)	-1(yr)	0(yrs)	1(yr)	2(yrs)	3(yrs)
UK global	-0.05	-0.07	-0.06	-0.02	0.09	0.15	0.15
UK diffuse	0.53	**0.62**	0.48	0.26	-0.04	-0.29	-0.39
UK direct	-0.17	-0.29	-0.34	-0.28	-0.07	0.18	0.37
US global	-0.46	-0.32	-0.07	0.23	0.49	**0.63**	**0.61**
US diffuse	0.48	**0.63**	**0.61**	0.42	0.12	-0.16	-0.31
US direct	-0.59	-0.51	-0.25	0.11	0.47	**0.70**	**0.73**

on time series that are strongly autocorrelated. Therefore, instead of standard test for statistical significance, we made an adjustment for reducing number of effectively independent samples represented by the data. These adjustments are made for both 5-year running mean and number of complete sunspot cycles, i.e. divide degree of freedom by five or number of complete sunspot cycles. Finally, our results in Table 2.6 satisfy both of these adjustments.

The satellite instruments from IPCC (2013) suggest a variation of extraterrestrial irradiance of 1.1 W/m², i.e. 0.08% of 1367 W/m², over the 11-year solar cycle (IPCC, 2013). We show that the corresponding variation in ground-based solar radiation received on the Earth is ~ 77 times the extra-terrestrial irradiance (Table 2.7). Cloud-cover changes are clearly a leading contender of this large discrepancy, as in percentage terms they are ~ 44 times the extra-terrestrial irradiance variations (Table 2.7). Since global and diffuse radiation received on the Earth are both influenced by cloud cover, this clearly explains the greater variation of solar radiation (compared with solar irradiance) recorded by the meteorological stations. Furthermore, there are no correlations between cloud cover and sunspot numbers for these thirteen weather stations in UK, which is also supported by Kristjánsson et al. (2003).

Figure 2.6 (a) shows that most of the power is concentrated around six to eight years period for British global radiation. However, Figure 2.6 (b) (which shows British
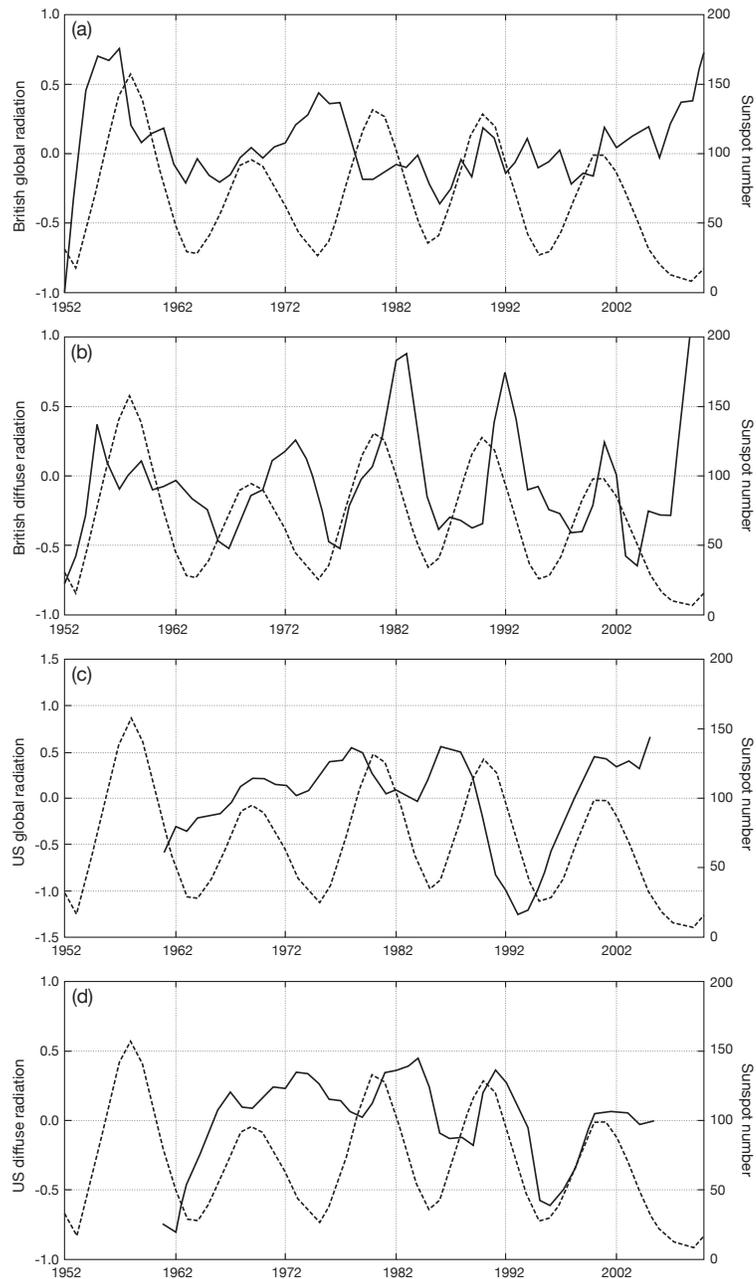
Figure 2.5: Comparison between detrended and normalised: (a) global radiation in Britain (solid line) and annual mean sunspot numbers (dashed line) for 1952-2010; (b) diffuse radiation in Britain (solid line) and annual mean sunspot numbers (dashed line) for 1952-2010; (c) global radiation in US (solid line) and annual sunspot numbers (dashed line) for 1961-2005; (d) diffuse radiation in US (solid line) and annual sunspot numbers (dashed line) for 1961-2010. Both the diffuse radiation and sunspot numbers data are annual averaged daily values and smoothed using 5-year running means.

Table 2.7: Standard deviations and coefficient of variations of annual means of British cloud and solar radiation (1952-2010) and US (1961-1990) solar radiation.

	Standard deviation	Coefficient of variation(%)
British cloud condition	0.20 okta	3.52
British global radiation	158.77 Wh m^{-2}	6.08
British diffuse radiation	93.95 Wh m^{-2}	6.18
US global radiation	190.24 Wh m^{-2}	5.56
US diffuse radiation	115.39 Wh m^{-2}	6.82

diffuse radiation) has the strongest power at eleven years period, in accordance with the 11year solar cycle. The wavelet analysis in Figure 2.6 (a) indicates a slight shift from a dominant 8-year period to a 6-year period during 1970-2005. The relations between global/ diffuse radiation and the solar cycle is next examined for the US sites. These show the strongest power at around eleven years period for both global and diffuse radiation (Figure 2.6 (c),2.6 (d)). In Figure 2.6 (c), the 16-year and 32-year time periods, which are also within the 95% confidence level can be safely ignored because they are affected by the cone of influence, where the edge effects become important.

Therefore, we hypothesise that the relatively short 6-8 year periodicity of British global radiation may be dominated by some regional climatic influence, such as the North Atlantic Oscillation (NAO), affecting cloud cover. This hypothesis should be explored as part of future work.

2.4 Conclusion

Our analysis of solar-radiation data for British weather stations from the UK Met Office has shown that the diffuse fraction was relatively low (high) during spring and summer (autumn and winter), and almost all the British weather stations used in this study have a diffuse fraction greater than 50% throughout the year (ranging on average from 64±8% in summer to 79±4% in winter). A similar analysis of the US diffuse fractions ranges from 49±15% in summer to 43±15% in winter, reflecting
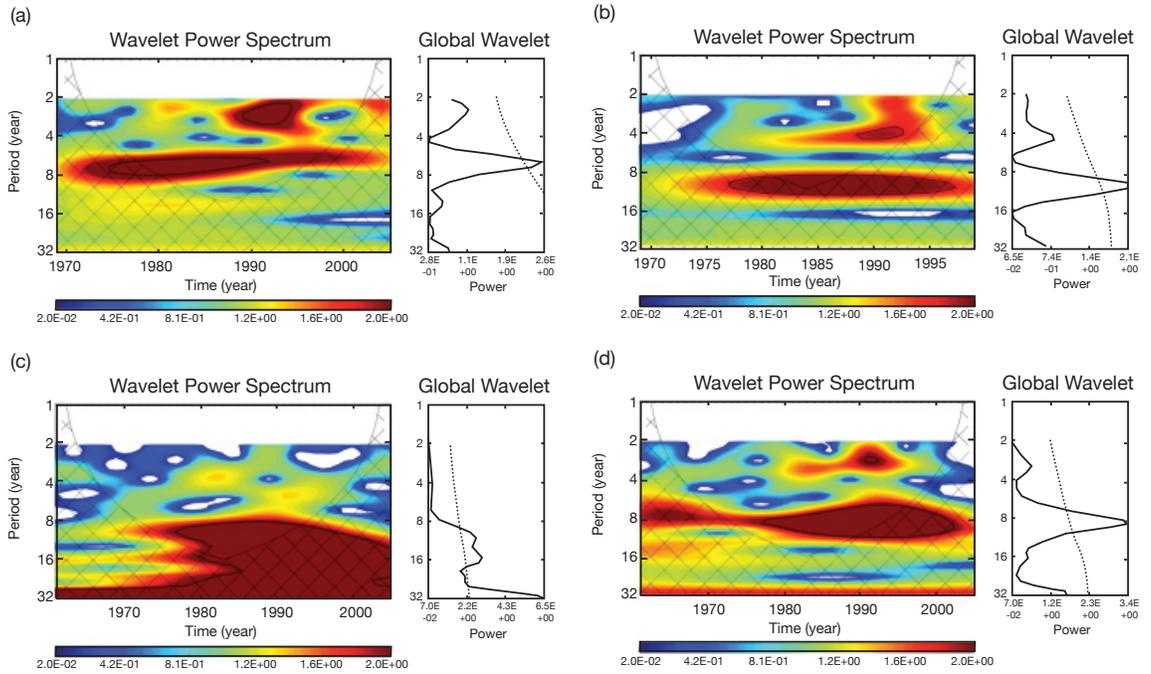
Figure 2.6: Wavelet analyses for: (a) normalised and detrended British global radiation time series for 1969-2005; (b) normalised and detrended British diffuse radiation time series for 1969-1999; (c) normalised and detrended US global radiation time series for 1961-2005; (d) normalised and detrended US diffuse radiation time series for 1961-2005. The 95% confidence level is shown by the black contours in Wavelet Power Spectrum and dashed lines in Global Wavelet part, and the cone of influence is indicated by the cross-hatched regions.

clearer conditions on average at these US stations.

British global radiation is generally correlates with diffuse radiation in winter, but much weaker in the other three seasons and annual values. In Britain, seasonal/annual cloud cover are significantly negatively correlated with seasonal/annual global radiation, and also in winter with diffuse radiation. During winter, more cloud cover results in less global and diffuse radiation. Global radiation is mainly dominated by cloud cover; whereas diffuse radiation may also be affected by aerosol.

In Britain, global radiation when scaled to its seasonal average values shows proportionately greater (lesser) variations during winter (summer), and this phenomenon is stronger for diffuse radiation. This is most likely related to greater changes in atmospheric air mass and circulation, e.g. involving the North Atlantic polar jet stream, storminess and NAO changes, making the British winter climate less stable.

We also found that British and US diffuse radiation generally comes after the sunspot numbers by ~ 2 years; US global/direct radiation tends to comes before sunspot numbers by ~ 2 years. But no such correlation happens between British global/direct radiation with sunspot numbers.

The variation in solar radiation received on the Earths surface has been found to be around ~ 77 times the extra-terrestrial irradiance changes. The variation in magnitude of British cloud cover is about ~ 44 times the extra-terrestrial irradiance variation. Since annual/seasonal British global (or diffuse) radiation and cloud cover are strongly correlated, cloud-cover changes explain the greater amplitude of global and diffuse radiation recorded by meteorological stations compared with the coincident variation in extra-terrestrial irradiance. No correlations are found between cloud cover and sunspot numbers in UK.

The results of the wavelet analysis show that the strongest power is at around eleven years period for both British and US diffuse radiation and US global radiation, which is consistent with the 11-year solar cycle, although with somewhat enigmatic 2-year lead/lags. However, the global radiation in Britain shows a slight shift from a period of eight years to six years during 1970-2005. We hypothesise that the

relatively shorter periodicity of global radiation in Britain may be driven by some regional climate factor such as NAO changes. This hypothesis will be explored as part of future work.

Chapter 3

Signature of the North Atlantic Oscillation on British solar radiation availability

Abstract

The impact of the North Atlantic Oscillation (NAO) on winter solar radiation in the British Isles is explored. Records of global horizontal radiation (GHR) from a set of UK Meteorological Office (UKMO) pyranometers spanning the last three decades have been compared to Hurrell's winter NAO index (WiNAOI). GHR in the West of Great Britain (GB) is found to be negatively correlated with WiNAOI; in eastern England, on the contrary, the correlation is significantly positive.

GHR can be decomposed in two components, direct and diffuse. Data availability limits the analysis of such components to some western Great Britain (GB) stations only, where WiNAOI is negatively correlated with GHR. Correlation with WiNAOI is stronger for direct radiation than for global, while it is not significant for the diffuse component. Wavelet analysis supports these results: direct radiation and WiNAOI feature a spectral peak at ~ 10 years, that neither diffuse nor GHR display.

This is a collaborative venture, and has minor correction before being accepted

for publication in the journal *Solar Energy* (Colantuono et al., 2014). The authors are: Giuseppe Colantuono, Yimin Wang, Edward Hanna and Róbert Erdélyi. I did the following work as my contribution.

Keywords: NAO; solar radiation; spatial variability.

3.1 Introduction

There is increasing interest in understanding variations of solar radiation reaching the Earth's surface, due to the the growing deployed photovoltaic (PV) capacity and its global environmental and economical implications (Jäger-Waldau, 2007; Dinccer, 2011). It is therefore not surprising that the share of irradiance variability due to prominent climatic phenomena has become subject of investigation: the impact of ENSO (El Niño/La Niña) on Australian irradiance availability has been examined (Davy and Troccoli, 2012); even more recently, Jerez et al. (2013) considered the impact of North Atlantic Oscillation (NAO) on renewable energy in Southern Europe. Knowing the effect on irradiance of such planetary-scale pseudo-oscillations can help reduce uncertainty in PV yield. The influence of NAO has recently been evaluated, for example, in various areas of power generation and demand (e.g. Ely et al., 2013) as well as in hydrology (Burt and Howden, 2013) or ecology (Zhai et al., 2013). The present chapter examines more closely the relationship between NAO and solar radiation over the UK, focusing on the winter season when NAO variability is strongest (e.g. Hanna et al., 2008).

NAO, defined as either the south-north mean sea-level pressure (MSLP) gradient across the North Atlantic (typically taking the Azores or Gibraltar as the southern station and SW Iceland as the northern station) or the North Atlantic component of the first mode of Northern Hemisphere MSLP variability (Hurrell et al., 2003), is related to the strength and variability of the westerly winds over the northern North Atlantic and Northwest Europe. High values of Winter NAO Index (WiNAOI) have

been associated with warmer- and wetter-than-normal winters in northern Europe, from Iceland to Scandinavia, and by inference with cloudier skies (Hurrell, 1995; Greatbatch, 2000; Hurrell et al., 2003). Consistent with this assumption, previous studies have reported a negative correlation between WiNAOI and wintertime values of solar radiation in Northwest Europe and over the British Isles (Pozo-Vázquez et al., 2004; Sanchez-Lorenzo et al., 2008). In particular, Pozo-Vázquez et al. (2004) found increasing absolute values of correlation while moving mainly from the southern to the northern part of Great Britain (GB), which reflects the closer proximity of the later region to the main North Atlantic storm tracks. However, the association of positive/negative WiNAOI with cloudy/clear skies has been partly disputed as winter overcast conditions are also possible during relatively cold and dry periods (see for example Mayes and Wheeler, 1997).

Here, the relationship between WiNAOI and solar radiation over the British Isles is examined with a spatial resolution higher than previous studies. This is in order to specify the geographical variability of the association between positive (negative) WiNAOI and lower (higher) global horizontal radiation (GHR) winter values beyond the current, simple picture of a northbound correlation gradient.

3.2   Methodology and dataset

We analyze the records of winter global horizontal radiation (GHR) in the last 31 years, taken hourly by a set of UK Meteorological Office (UKMO) pyranometers (UK Meteorological Office, 2012a); radiation measurements come from secondary ISO 9060 standard pyranometers (UK Meteorological Office, 2011, 2013) and are quality checked, meaning that unreliable data are supposed to be removed. "Dirt, snow or frost" (the sensors are not heated) are mentioned as possible causes of errors, together with horizon obstacles (UK Meteorological Office, 2012b). Invalid hourly data represent $\sim 4\%$ of the examined records, and are slightly more numerous ($\sim 5\%$) from October to January. On the contrary, invalid measurements are equally

present in the morning (before 12 UTC) and in the afternoon/evening, suggesting that morning frost/dew is not the main cause of error.

The 31-year time period is then split into sub-periods, as a means of including a greater number of simultaneously active pyranometers and increasing spatial resolution, and the timeseries are monthly-averaged. In order to consider a pyranometer "active" in a given sub-period, the associated timeseries is required to have no more than 70 invalid hourly values per month ($\sim 10\%$ of the monthly record). Sub-periods allow also for a qualitative checking of the persistence of NAO signature over the years. The recently increased availability of valid global radiation sensors (around 50 sensors in 1990, more than 100 today, although the number of stations continuously active over the last 16 years is about 30) enables us to split GB into different zones for the last 16 years, and search for spatial inhomogeneities. Consistent with the existing NAO and climate literature, the winter season is defined as DJF (December-January-February, where the December month belongs to the preceding year). The examined periods are the last 31 years (1983-2013, Figure 3.1, left panel), the last 21 years (1993-2013, Figure 3.1, right panel), the last 16 years (1998-2013, Figure 3.2), and the 21-year interval from 1983 to 2003, (Figure 3.1, center panel). For each period, a map for the winter season has been constructed, showing the UKMO stations active throughout the time interval and their relative correlation coefficients with the principal component-based (Hurrell, 2013) WiNAOI index.

Also, timeseries of GHR for individual calendar months have been compared with the relevant NAO index, as well as the winter season extended to March (DJFM). We do not report the results for any of these additional cases, as the signature of NAO is weaker with respect to the DJF season. WiNAOI therefore stands for the DJF NAO index throughout the entire chapter.

In order to aggregate monthly values and compose the winter season, the GHR timeseries for any winter calendar month at each location have been normalized to the local horizontal extraterrestrial irradiance. Having thus accounted for seasonal cycling, this procedure allows us to isolate the modulation that the atmospheric

Table 3.1: Details of the UKMO pyranometers (sorted from south to north) shown in Figure 3.2. The fifth column reports the WiNAOI vs GHR correlation coefficient for the 1998-2013 period. Correlation coefficients with P-value (column 6) lower than 5% are in bold italics, while they are in bold if $0.05 < P \le 0.10$.

ID	Station Name	Lat	Lon	Corr	P
1395	Camborne	50.22	-5.33	***-0.80***	0.00
1415	Cardinham	50.50	-4.67	***-0.69***	0.00
779	Thorney island	50.81	-0.92	0.32	0.24
744	East Malling	51.29	0.45	***0.49***	0.05
726	Kenley airfield	51.30	-0.09	0.34	0.20
471	Rothamsted	51.81	-0.36	**0.45**	0.08
692	Little Rissington	51.86	-1.69	0.28	0.29
1198	Aberporth	52.14	-4.57	***-0.71***	0.00
461	Bedford	52.23	-0.46	***0.55***	0.03
669	Shobdon airfield	52.24	-2.88	0.03	0.92
595	Church Lawford	52.36	-1.33	0.38	0.17
1190	Lake Vyrnwy n.2	52.76	-3.46	-0.28	0.29
1161	Aberdaron	52.79	-4.74	**-0.49**	0.06
554	Sutton Bonington	52.84	-1.25	0.41	0.11
395	Holbeach n.2	52.87	0.14	0.18	0.51
1144	Hawarden airport	53.18	-2.98	0.37	0.16
18904	Manchester Hulme	53.47	-2.25	-0.26	0.34
370	Leconfield	53.87	-0.44	***0.69***	0.00
1568	St Angelo	54.40	-7.64	***-0.67***	0.00
1450	Aldergrove	54.66	-6.22	***-0.59***	0.02
1467	Ballypatrick forest	55.18	-6.15	-0.39	0.14
1023	Eskdalemuir	55.31	-3.21	***-0.54***	0.03
268	Charterhall	55.71	-2.38	-0.09	0.77
212	Strathallan airfld	56.33	-3.73	0.14	0.59
177	Inverbervie n.2	56.85	-2.26	**0.46**	0.07
105	Tulloch bridge	56.87	-4.71	***-0.57***	0.02
113	Aviemore	57.21	-3.83	-0.11	0.68
67	Loch Glascarnoch	57.73	-4.89	***-0.76***	0.00
54	Stornoway airp.	58.21	-6.32	***-0.69***	0.00
44	Altnaharra n.2	58.29	-4.44	**-0.45**	0.08
9	Lerwick	60.14	-1.18	**-0.44**	0.09

processes impose on the deterministic amount of solar energy available in outer space. This method avoids the obliterating consequences of overweighting the variance of the brighter months of the season: e.g., the energy received in February is about twice the value of December at a latitude of 50°N, and four times at 60°N.

Global radiation is the sum of the direct and diffuse components, the estimation of which is crucial for converting GHR into global tilted radiation and assessing/predicting PV performance. Only a few UKMO sensors gauging diffuse radiation were operating in the UK until 1997, although these have since been inactive. The relationship of diffuse/direct records with WiNAOI is examined, although the presence of an East/West pattern cannot be verified due to insufficient geographical coverage.

3.3 Results

3.3.1 Winter GHR: correlation analysis

The correlation analysis between global radiation and WiNAOI over the last 31 years is summarized in Figures 3.1-3.3. During the 31-year time interval, a set of only six UK stations is available. The average timeseries (Figure 3.3) features a negative $r = -0.63$, suggesting that geographical averaging filters out fluctuations that are random in nature and therefore unrelated to NAO. These results could suggest the erroneous conclusion that solar radiation over the UK is uniformly negatively correlated with WiNAOI. The picture revealed by the analysis of shorter and more recent periods, instead, is much more varied, as shown by the higher number of active UKMO stations in Figure 3.2. In the 1993-2013 time interval (summarized in Figure 3.1c) only four more valid stations are present with respect to 1983-2013 (Figure 3.1a). In the 1998-2013 time span, instead, many additional UKMO sensors appear (Figure 3.2). The timeseries recorded in the east are characterized by opposite behavior compared with the western UKMO stations, as they are positively correlated with WiNAOI. Considering a relatively low significance value ($0.05 < P \leq 0.10$) for a
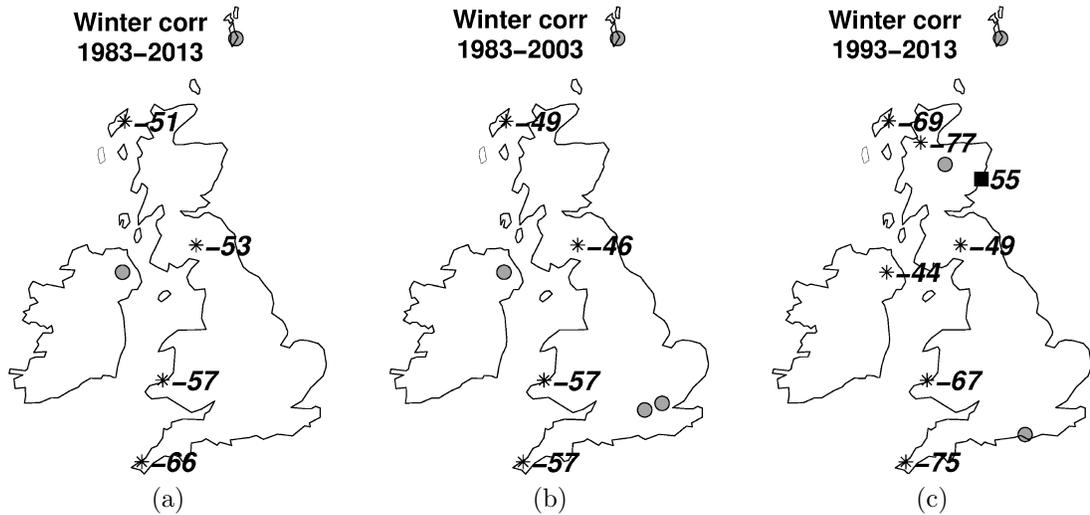
Figure 3.1: (a): The UK Meteorological Office (UKMO) stations recording GHR between 1983 and 2013. Stars/squares indicate negative/positive correlation (multiplied by 100) between GHR and WiNAOI, while circles are used for sensors showing no significant correlation (correlation coefficients are significant at the 5% level in all the panels). The correlation coefficient for the average of all the available pyranometers (Figure 3.3) is $r = -0.63$ ($P = 0.01$). (b) 1983-2003: $r = -0.41$ ($P = 0.10$) for the average of all available sensors. (c) 1993-2013: a station with positive correlations appears on the East coast; for the geographical average it is $r = -0.56$ ($P = 0.01$), due to the disrupting effect of the positively correlated station and of some uncorrelated stations absent from panel (a).

few locations in Figure 3.2 and Table 3.1 is justified by the limited length of the 1998-2013 timeseries, which is the only period offering a sufficient spatial resolution. On the other hand, the geographical pattern emerging from the collective behavior of the ensemble (Figure 3.2) reinforces the conclusion that the correlation does not occur by chance.

The relatively recent deployment of the "eastern" set of pyranometers disrupts the strong negative correlation of the average global radiation timeseries occurring for the 31 year-long period and shown in Figure 3.3. On the other hand, Figure 3.4 shows that the 1998-2013 GHR averaged over the "eastern" timeseries (that is, the timeseries positively correlated with WiNAOI, as shown in Figure 3.2) is positively correlated with WiNAOI, while the correlation coefficient between WiNAOI and the
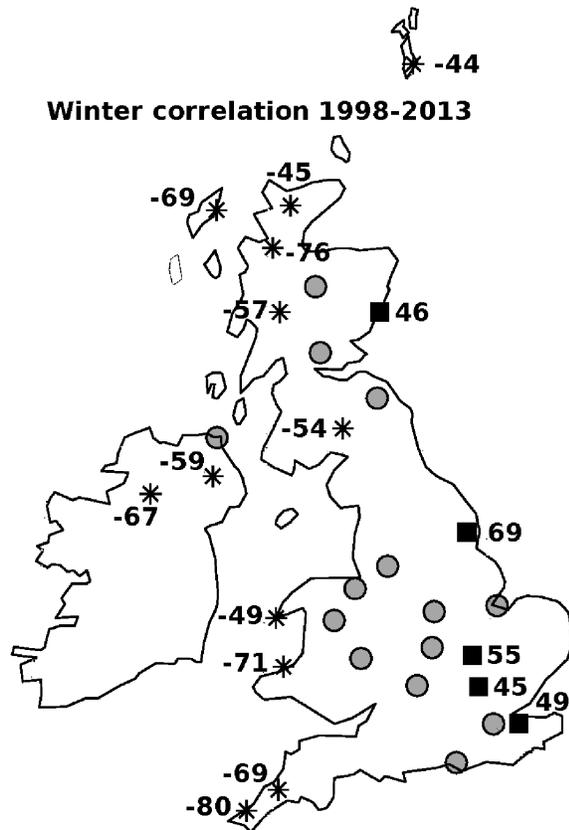
Figure 3.2: Like Figure 3.1, but for 1998-2013. A higher number of stations is available. A seesaw pattern emerges with respect to Figure 3.1: positive correlation values on the East of GB (squares, corresponding to bold positive values in Table 3.1), uncorrelated stations in Central England (circles), and negative correlation (represented with stars as in Figure 3.1, corresponding to bold negative values in Table 3.1) on the Atlantic side of GB and in the available stations in Ireland. Unlike Figure 3.1 (particularly panels a and c), the correlation between WiNAOI and the geographical average is not significant, due to the presence of the eastern pyranometers.

"western" average is negative. Also, an additional cluster of UKMO pyranometers is active in central and southern England, none of which is significantly correlated with WiNAOI. They may, however, reveal a transition zone between the negative correlations on the western side of GB and the positive correlation on the east. For completeness, in Figure 3.1b the stations active between 1983 and 2003 are reported with the correlation coefficients. The situation is similar to the full 31-year period, although the significantly negative correlation values are in general lower. Some
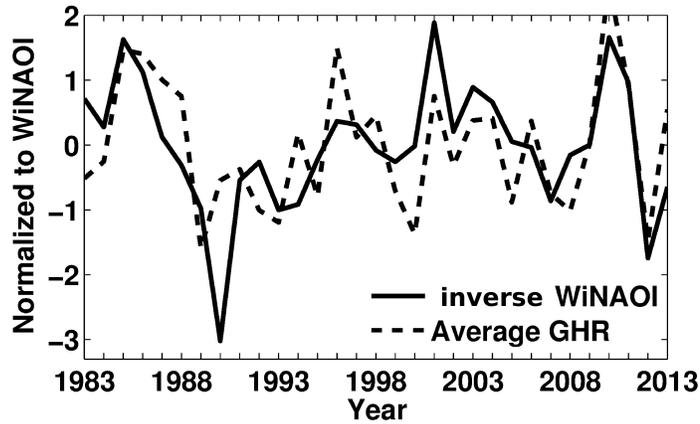
Figure 3.3: 1983-2013 winter NAO index (WiNAOI) is plotted with global horizontal radiation (GHR) recorded at the locations shown in Figure 3.1a, geographically averaged and then normalized to WiNAOI. The correlation coefficient, $r = -0.63$, is at the 99% confidence level.

(a) Western pyranometers   (b) Eastern pyranometers
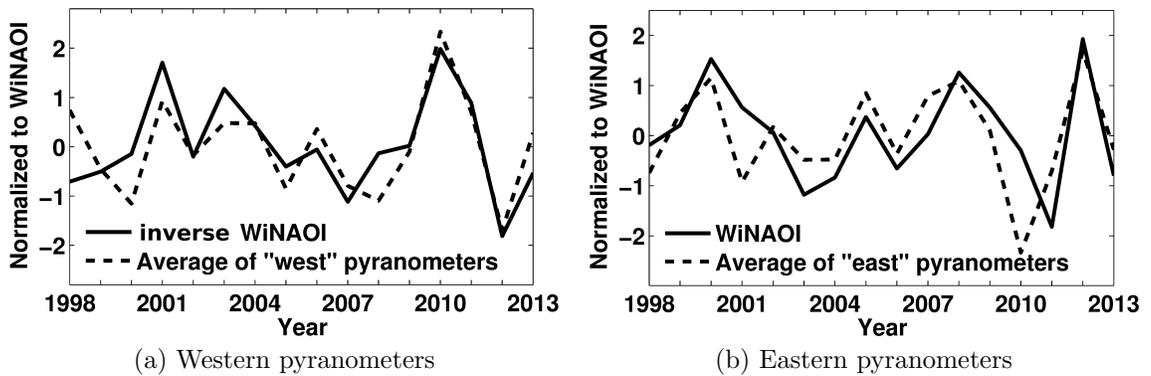
Figure 3.4: The geographical average of GHR for those UKMO stations that significantly negatively (positively) correlate with WiNAOI for 1998-2013 is plotted in the left (right) panel versus inverse WiNAOI (versus WiNAOI). The correlation coefficients are -0.79 and 0.66, respectively ($P < 0.01$), showing the opposite behavior of East and West of the British Isles' irradiance with respect to WiNAOI. All curves are normalized as in Figure 3.3.

extra stations are present with respect to the longer period, and are not significantly correlated. For the average we obtain $r = -0.41$, lowered by the stations in the Southeast which are absent in the 31-year time interval.

45

3.3.2 Winter direct and diffuse radiation

Diffuse solar radiation is, in general, a rarely measured physical quantity, despite its fundamental importance for solar energy applications. The UKMO recordings of the diffuse component were discontinued in 1997; the direct component, which could be determined by subtraction, is therefore equally unknown from then. In the cloudy British climate, the diffuse component constitutes a significant part of global radiation (Clarke et al., 2007b) and can exceed 50% at the monthly timescale. We therefore extend the analysis of the radiation-WiNAOI relationship to the direct and diffuse components for the available data. As for the 31-year timeseries discussed in the previous sessions, there are only four available stations, all negatively correlated with the WiNAOI index. The analysis that follows does not therefore pertain to the East-West seesaw discussion, but rather gives evidence of the stronger relation WiNAOI has with direct radiation rather than with global.

The correlation between the direct component and WiNAOI outperforms its global counterpart in winter; on the other hand, diffuse radiation shows little co-variation with WiNAOI for the available dataset (Table 3.2). The problem has been

Table 3.2: Correlation between horizontal radiation components and WiNAOI from 1969-1997, with significant ($P \leqslant 0.5$) correlations denoted in bold.

Global radiation

Station ID	9	1023	1450	1575	Mean
corr.coef	-0.06	**-0.71**	**-0.43**	-0.25	**-0.49**

Direct radiation

Station ID	9	1023	1450	1575	Mean
corr.coef	-0.29	**-0.72**	**-0.48**	-0.19	**-0.61**

Diffuse radiation

Station ID	9	1023	1450	1575	Mean
corr.coef	-0.19	-0.24	-0.09	-0.20	-0.08

also examined in the frequency domain. Figure 3.6 reports the outcome of the wavelet Fourier analysis. The only statistically significant power peak of WiNAOI for the
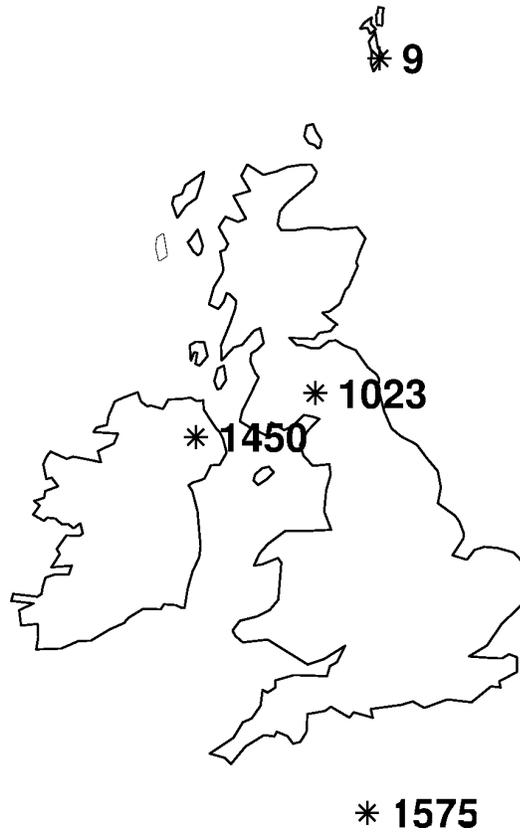
Figure 3.5: The UKMO stations available during 1969-1997 are shown. Locations for stations 9, 1023 and 1450 are reported in Table 3.1, while 1575 is on Jersey island.

1969-1997 interval corresponds to a period of ~ 9 years; this result does not differ significantly from that obtained by Hurrell et al. (2003) for the 1899-2002 period. The corresponding direct radiation timeseries peaks at ~ 10 years, while global and diffuse radiation do not reach the threshold of significance. The spectrum of direct radiation therefore shows the best approximation to the WiNAOI spectrum.

3.4   Discussion and conclusions

In this study we have analyzed the relationship between the North Atlantic Oscillation and the availability of solar radiation at the Earth's surface in the British Isles; the spatial resolution is higher than in previous studies (Pozo-Vázquez et al., 2004; Sanchez-Lorenzo et al., 2008). High values of the NAO index are generally associ-

(a) Winter Global Radiation

(b) Winter Direct Radiation

(c) Winter Diffuse Radiation
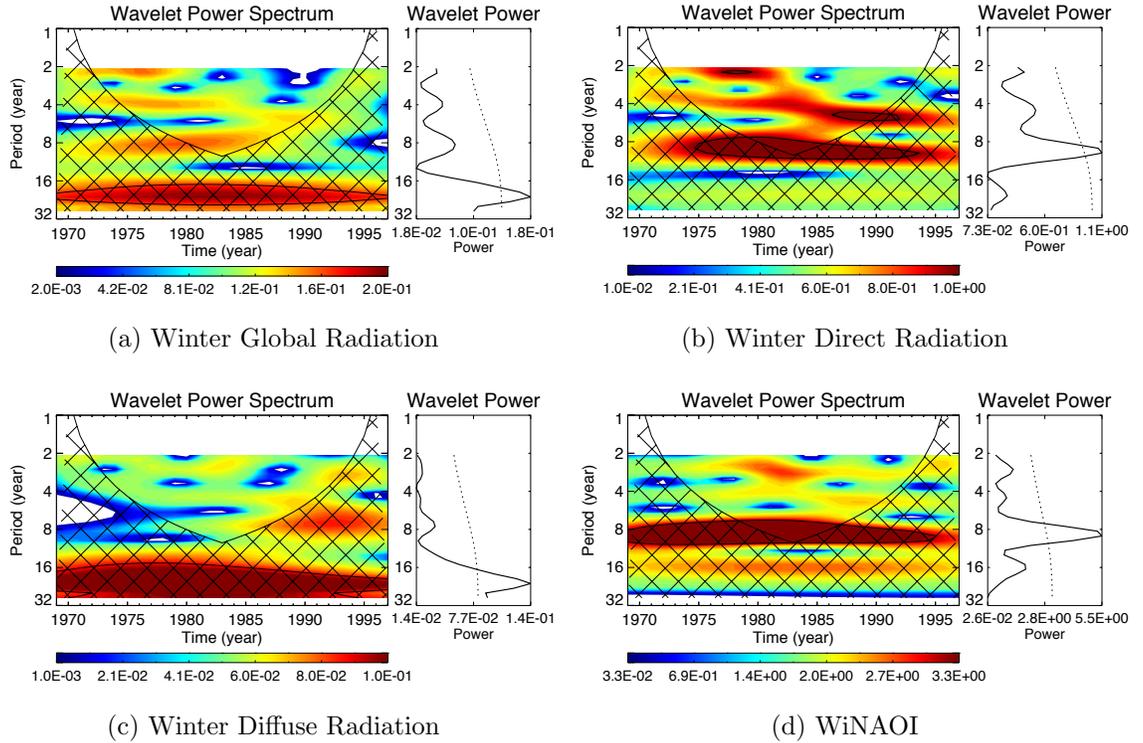
(d) WiNAOI

Figure 3.6: Wavelet output for the normalized and detrended (a) winter global radiation; (b) winter direct; (c) winter diffuse; (d) WiNAOI for 1969-1997. The confidence level is 90%, and is represented by the black contours in the Wavelet Power Spectrum plots and by the dashed lines superposed to the Global Wavelet curves; the cone of influence is indicated by the cross-hatched regions

ated with relatively mild and cloudy weather, although important exceptions exist (Mayes and Wheeler, 1997). We have found a strong, significant negative correlation between WiNAOI and the anomaly of GHR in the West of GB. In the East of the country, however, the correlation is significantly positive. This trend becomes evident in the last 16 years only, when a sufficient number of UKMO pyranometers spread throughout GB become available. The analysis limited to those few sensors continuously available during the last 31 years, none of which shows significant positive correlations with WiNAOI, could erroneously suggest the negative correlation with WiNAOI as a feature characterizing the whole archipelago. This is also the main position held in the existing literature, which examines wider areas (Pozo-Vázquez

et al., 2004; Sanchez-Lorenzo et al., 2008) and suggests the existence of a meridional gradient of correlation at the continental scale. Although the large-scale findings of Pozo-Vázquez et al. (2004) seem not completely incompatible with a small East-West variation of correlation coefficient over GB (Figure 2 therein), they indicate the North of the British Archipelago as one of the areas of strongest negative correlation between NAO index and solar radiation, in juxtaposition with the positive values for the Iberian region. In the present, more localized, and higher resolution study, the gradient is instead East/West.

The relationship of WiNAOI with the storm tracks and blocking over northwest Europe (Woollings, 2010) suggests a possible explanation for the East/West seesaw in terms of intensified storm tracks for positive WiNAOI winters, in which case a strong westerly flow is expected over western UK, leading to enhanced cloudiness and to a reduction of solar irradiance. In the opposite case (WiNAOI < 0), the weaker westerly flow is likely to be associated with easterly flow and blocking events, which can cause eastern UK to receive maritime airmasses, with more clouds and less solar radiation reaching the Earth surface.

Trigo et al. (2002) found WiNAOI positively correlates with the cloud cover in the West of GB; while this correlation is negative in the East of GB during high WiNAOI period. This means, as WiNAOI increases, the cloud cover in the West (East) of GB increases (decreases), and thus global radiation in the West (East) of GB decreases (increases) causing the negative (positive) correlation between WiNAOI and global radiation in the West (East) of GB. Therefore, this result from Trigo et al. (2002) are consistent with our findings. However during low WiNAOI period, Trigo et al. (2002) reported the opposite correlation pattern, i.e. WiNAOI negatively (positively) correlates with the cloud cover in the West (East) of GB. This part of their results is opposite to our findings. Bear in mind, Trigo et al. (2002) did not report significant level of their results. In our work, we did not compare high/low WiNAOI with global radiation separately, which should be explored as part of future work.

The correlation between the direct component and WiNAOI outperforms its

global counterpart in winter; diffuse radiation shows little co-variation with WiNAOI for the available dataset.

Chapter 4

Novel investigation of the state-of-the-art solar radiation models

Abstract

Horizontal diffuse radiation data are required in order to estimate monthly global radiation on a given tilted surface and for optimising the structure of a range of photovoltaic (PV) panels. Although global radiation data are commonly available, diffuse radiation data are not readily obtainable because of cost; there are, for example, about 50 British weather stations currently reporting global radiation, but only thirteen have recorded diffuse radiation.

This chapter evaluates the accuracies of four different models of global and diffuse radiation - the PVGIS model, UKCP09 model, Liu and Jordan model and Page model - against ground measurements from these thirteen UK Met Office British weather stations. The comparisons are made using standard statistical methods, which are the mean bias error (MBE) and root mean square error (RMSE). Our results show that the PVGIS model is the most accurate, followed by the Page model, UKCP09 model and Liu and Jordan model.

4.1   Introduction

For a horizontal surface, the global solar radiation is the sum of the direct, diffuse and ground-reflected radiation. The ground-reflected radiation at a location from surrounding topographic features is normally trivial compared with global radiation and is therefore ignored in this study (HEMI, 2000).

In Britain, just a few weather stations measure diffuse radiation, so real data are difficult to obtain (BADC, 2012); moreover, calculating the diffuse component using mathematical models is often inaccurate because it largely depends on complex local terrain. Concerns about the accuracy of solar radiation models have increased with the recent explosion of interest in exploiting this energy for renewable solar electricity generation (Clarke et al., 2007a). Many models for evaluating diffuse radiation and converting global radiation incident on a horizontal surface to that received by a tilted surface have been developed.

Solar estimates from ground station measurements naturally give the most accurate data with a high temporal resolution, e.g. every fifteen minutes, hourly or daily, when the solar radiation at a specific place needs to be known but obviously are often not available, even for a suitably representative nearby site; moreover, the radiation sensor may be covered with dirt, frost or snow or shaded by trees and/or buildings (PVGIS, 2010). Therefore, in these cases or for comparison purposes, solar-radiation estimates from satellites can be applied (PVGIS, 2010). Typically, the satellites measure extraterrestrial irradiance, from which is subtracted both the visible and infrared light reflected by the Earth and clouds (also measured by satellites) and the parts that are absorbed by the atmosphere and clouds. Problems and biases with this method include snow cover, varying terrain in mountain areas and low Sun angle (PVGIS, 2010). Assumptions and biases may also result from the part of radiation

that is subtracted, as described in Section 4.2.1.

Plenty of hourly solar radiation models have been evaluated (Noorian et al., 2008; Perez et al., 1990a). In Sections 4.2 & 4.3, we analyse four normally used monthly solar-radiation models in order to compare their accuracies with observed data from a range of different microclimates (representing different latitudes, cloud cover and local terrain differences). These models are the Photovoltaic Geographical Information System (PVGIS) model (PVGIS, 2012), UK Climate Projections (UKCP09) model (Murphy et al., 2009), Liu and Jordan (1962) model and Page (1961) model. The accuracies of the models are investigated by developing monthly average daily values of diffuse fraction (diffuse component over global radiation) for each model, and comparing these diffuse fractions with those calculated from observed data. The validation benchmarks are mean-bias error (MBE) and root-mean-square error (RMSE).

4.2 Methodology and datasets

4.2.1 Description of models

(i) PVGIS model

The PVGIS data are based on calculations from satellite images performed by the Satellite Application Facility on Climate Monitoring (CM SAF). The database represents a total of twelve years of global and direct radiation data, which comprise data from the first generation of Meteosat satellite (MFG) covering the period 1998 to 2005 and from the second-generation Meteosat satellites (MSG) spanning June 2006 to May 2010; the diffuse radiation is derived by subtracting direct component from its global counterpart. It covers the geographical domain of 0° N to 58° N and from 15° W to 35° E, which includes most of Europe and northern Africa. The spatial resolution at nadir, i.e. directly under the satellite at 0° N, 0° W, is 1'30 (3km) (Huld et al., 2010).

The following sub-sections describe the algorithms for deriving global and direct

radiation in the PVGIS model.

Global radiation   This component of the radiation is determined by

$$R_G^{in}(1 - \alpha) = R_{Tot}^{in} - R_{Tot}^{out} - R_A, \qquad (4.1)$$

where R_G^{in} is the global radiation at the ground. This is the part utilised by humans on the Earth. α is the surface albedo, which can be derived from satellite observations. R_{Tot}^{in} denotes the total incoming solar radiation at the top of the atmosphere, or extraterrestrial irradiance, which is calculated from the solar constant and solar zenith angle. R_{Tot}^{out} is the total outgoing solar radiation, or reflected solar irradiance at the top of the atmosphere, which can be measured directly by satellites. R_A is the part of the solar radiation absorbed in the atmosphere by gaseous compounds (such as water vapour and ozone) and aerosols. This parameter is not easily derived by satellite observations and is thus retrieved by radiative transfer models (Kiehl and Trenberth, 1997).

The absorbed solar radiation R_A strongly affects the total outgoing solar radiation R_{Tot}^{out}, which has strong correlation with atmospheric transmittance. Therefore, the algorithm to retrieve R_A uses: R_{Tot}^{out} - measured by satellite; R_{Tot}^{out} - simulated by radiative transfer models (RTMs) for various atmospheric conditions (transmittances).

A look-up table (Müller and Trentmann, 2010) that has already been derived from a comparison of cloud information and ground-based measurements of global and diffuse radiation, which defines turbidity under different meteorological conditions.

MeasuredR_{Tot}^{out} is compared toR_{Tot}^{out} calculated by the RTM, from which we find the result that is closest to the observed R_{Tot}^{out} and its corresponding atmospheric transmittance. The actual atmospheric transmittance is derived by linear interpolation between the two pre-defined transmittance values in the look-up table;

Direct radiation   The algorithm consists of two parts: clear sky and cloudy sky conditions. The cloud fraction, which is derived with the SAF software (Derrien

and LeGLeau, 2005) operated by CM- SAF, is used to distinguish between clear and cloudy skies.

For clear-sky conditions, direct radiation is pre-calculated using an RTM for various atmospheric transmittance conditions and stored in a look-up table. A global aerosol dataset (Koepke et al., 1997) and optical properties of aerosols and clouds (d'Almedia et al., 1991) are used in a software package (Müller and Trentmann, 2010) to derive the transmittance condition from a look-up table. After the aerosol factors are considered, the water vapour taken from the global numerical weather prediction model of the German Weather Service (Majewski et al., 2002) together with the ozone values from the US standard atmosphere ($\sim$ 345 DU) (Müller and Trentmann, 2010) are used to correct the atmospheric transmittance state, and thus its associated pre-calculated direct radiation can be found.

Secondly, for a totally cloudy sky, the direct radiation is set to be zero; for fractional cloud cover the formula of Mueller et al. (2009) is used:

$$R_{\text{cloudy sky}} = R_{\text{clear sky}} \times (k - 0.38 \times (1 - k))^{2.5}, \qquad (4.2)$$

where $R_{\text{cloudy sky}}$ is the direct irradiance under cloudy sky; $R_{\text{cloudy sky}}$ is the clear sky direct radiation, and, k is the clear-sky index, which is the ratio of global radiation for cloudy sky to clear sky and can be derived from the CM-SAF remote sensing Surface Incoming Solar Radiation product (Mueller et al., 2009).

Regarding parameter accuracy, the calculations of this model are based on MSG pixel basis using instantaneous images (at least hourly images). The daily average is computed by arithmetic averaging; the monthly mean is calculated from the daily averages if at least 20 daily means within one month are obtainable; finally, a spatial average of 15$\times$15 km^2 is applied (Müller and Trentmann, 2010).

Diffuse fractions are obtained by the following calculations:

Clear sky:

$$\frac{R_G^{in} - R_{\text{clear sky}}}{R_G^{in}}, \qquad (4.3)$$

Fractional cloud cover:

$$\frac{R_G^{in} - R_{\text{cloudy sky}}}{R_G^{in}},\tag{4.4}$$

Totally cloudy sky: 1.

(ii) UKCP09 model

The UKCP09 model applies algorithms based on the daily hours of bright sunshine and day length at a selected location.

Global radiation Cowley (1978) developed a set of linear regression equations relating daily global radiation and daily sunshine duration for ten stations in Great Britain. Making use of these equations, the interpolated grid global radiation maps for Great Britain can be produced using sunshine duration data with the baseline 1961-1990 available at 25-km resolution. Cowleys equation is given as:

$$G = E\left[d\left\{(\frac{a}{100}) + (\frac{b}{100})(\frac{n}{N})\right\} + (1-d)a'\right],\tag{4.5}$$

where G and E are the daily horizontal global and extra-terrestrial radiation, n is the daily hours of bright sunshine provided by measurement and N is the day length, $d = 0$ if $n = 0$, otherwise $d = 1$ if $n > 0$, and $a' = $ average ratio of G/E for overcast days. The monthly means for the coefficients a, a' and b were provided by Appendix B1 in Muneer (2004), in which 1961-1990 sunshine duration and global radiation data from fifteen weather stations ranging in latitude from 50.383° (Plymouth) to 57.150° (Aberdeen) were used to derive the coefficients a, a' and b; the extra-terrestrial radiation E can be easily computed using the solar constant and knowledge of solar geometry (Muneer, 2004).

Diffuse radiation Muneer (2004) recommends the following global model, which was developed via regression curves to establish the relationship between the daily

diffuse fraction (diffuse over global radiation) and the clearness index (K_T).

$$\frac{D}{G} = 0.962 + 0.779K_T - 4.375K_T^2 + 2.716K_T^3, \text{ for } K_T \geq 0.2, \qquad (4.6)$$

$$\frac{D}{G} = 0.98, \text{ for } K_T < 0.2. \qquad (4.7)$$

$$K_T = a + bn. \qquad (4.8)$$

(iii) Regression model

The distribution of solar radiation is to a large extent depends on latitude, owing to the geometry of the Earth's rotation and revolution about the Sun (HEMI, 2000). A simple method of estimating the daily solar radiation regime is applied, referring to these latitudinal changes.

In order to facilitate the discussion, diffuse fraction (diffuse over global radiation fraction) has been defined (Liu and Jordan, 1960). Both global and diffuse radiation are on a horizontal surface, and are functions of solar altitude, cloud cover, aerosols and other radiation-reducing factors. When the atmosphere is relatively clean, the daily variation of diffuse fraction for a fixed solar altitude mainly results from the variation of atmospheric water vapour (Liu and Jordan, 1960), although cloud cover also needs to be considered. Similarly, clearness index (global radiation over extra-terrestrial irradiance) can be used and is easier to apply since global radiation measurements are more readily available than diffuse and extra-terrestrial irradiance is easy to calculate. Therefore, in order to compute diffuse radiation (e.g. where in situ measurements are not available), the diffuse fraction, normally expressed as K = diffuse component over global radiation, is treated as a function of (inversely related to) the clearness index K_T = global radiation over extraterrestrial irradiance. Thus, the diffuse radiation is calculated based on observed global radiation and calculated

extra-terrestrial irradiance as shown in the following equation:

$$\frac{\text{Diffuse radiation}}{\text{Global radiation}} = f\left(\frac{\text{Global radiation}}{\text{Extraterrestrial irradiance}}\right) \tag{4.9}$$

The first correlation between the hourly diffuse fraction and the corresponding clearness index was developed by Orgill and Hollands (1977) and was based on four years of data measured in Toronto, Canada.

Using observed radiation data, the function just mentioned above can be deduced by the regression calculation as shown in Figure 4.1. This figure shows the regression curves produced by the two upcoming models of clearness index versus diffuse fraction in June for British weather station No. 9 in Lerwick; other months or weather stations show similar patterns to this one.

Note that if a particular years observed monthly global radiation and extra-terrestrial irradiance data are input into the following two regression models, that years diffuse radiation is calculated; alternatively, where several years averaged global radiation and extra-terrestrial irradiance data are input, then the average diffuse radiation for those years is computed.

Liu & Jordan model

The Liu & Jordan model, depicted in Equation 4.10, is based on monthly mean daily global radiation data from several locations in the United States and Canada up to 1962 (Liu and Jordan, 1962).

$$\overline{K} = 1.390 - 4.027\overline{K_T}^2 - 3.108\overline{K_T}^3. \tag{4.10}$$

Page model

The Page model, shown in Equation 4.11, was developed based on ten stations, which are between 40°N and 40°S, spread around the world up to 1961 (Page, 1961):
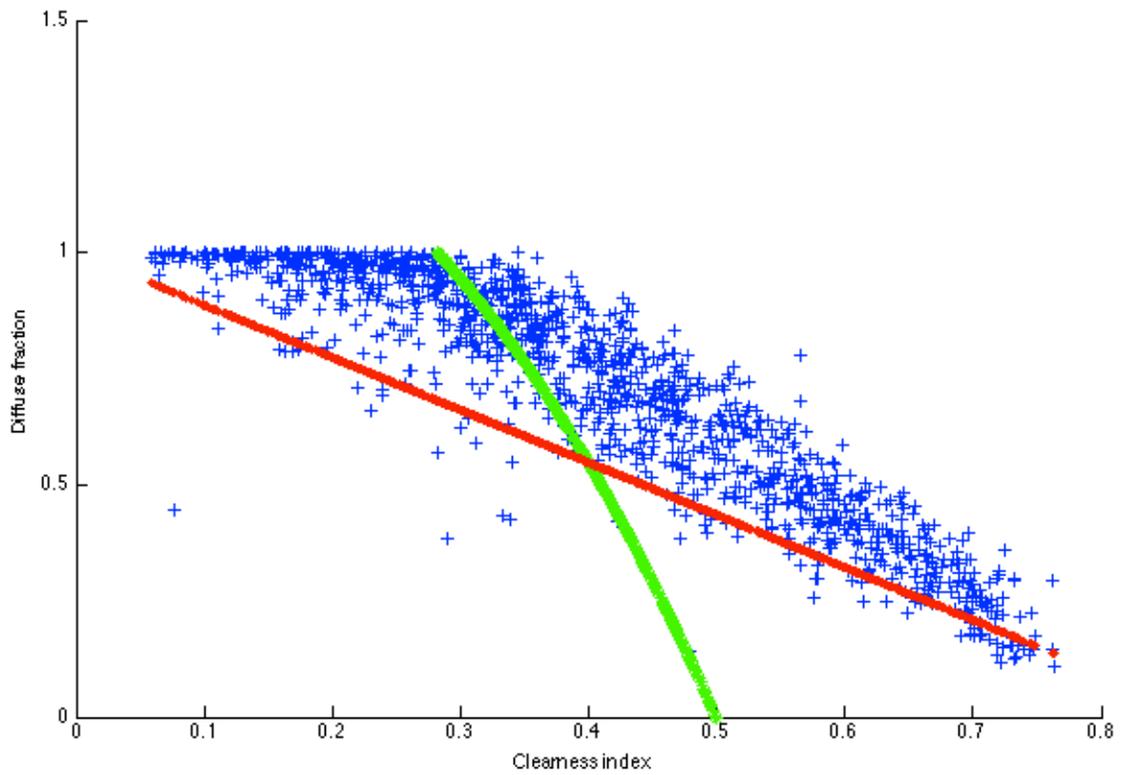
Figure 4.1: Regression curves of diffuse fraction (y-axis) versus clearness index (x-axis) for June for British weather station No. 9 (Lerwick). Regression curves are produced by the Liu & Jordan model (green) and Page model (red). Modelled diffuse fractions greater than one have been removed.

$$\overline{K} = 1.00 - 1.13\overline{K_T}. \tag{4.11}$$

In Equations 4.10 and 4.11, $\overline{K}$ is the monthly mean daily diffuse fraction, which is calculated by dividing monthly mean daily diffuse radiation by monthly mean global radiation; $\overline{K_T}$ is the monthly mean daily clearness index, which is the percentage of monthly mean global radiation relative to the extra-terrestrial radiation. We used the observed monthly mean global radiation; the extra-terrestrial radiation E was computed using the solar constant and knowledge of solar geometry (Muneer, 2004).

4.2.2 UK Met Office weather stations

The British ground measurements used in this chapter have been reported in Section 2.2.1 in Chapter 2.

4.2.3 Statistical data analysis

The model results are evaluated using mean bias error (MBE) and root mean square error (RMSE). Because the diffuse fractions from both the PVGIS and UKCP09 models do not change according to year, they are compared with each years observed solar radiation. However, the diffuse fractions from the Liu & Jordan and Page models are computed based on monthly mean daily values for each year, and the results are compared with the observed diffuse fractions from the respective year.

4.3 Model validation

In Figure 4.2, we can see that the diffuse fractions calculated by the UKCP09 and Liu & Jordan models have the largest errors of the four models (relative to in situ data).

An error analysis was carried out to calculate the errors of monthly average daily diffuse fractions, because the diffuse fraction is necessary for calculating global radi-
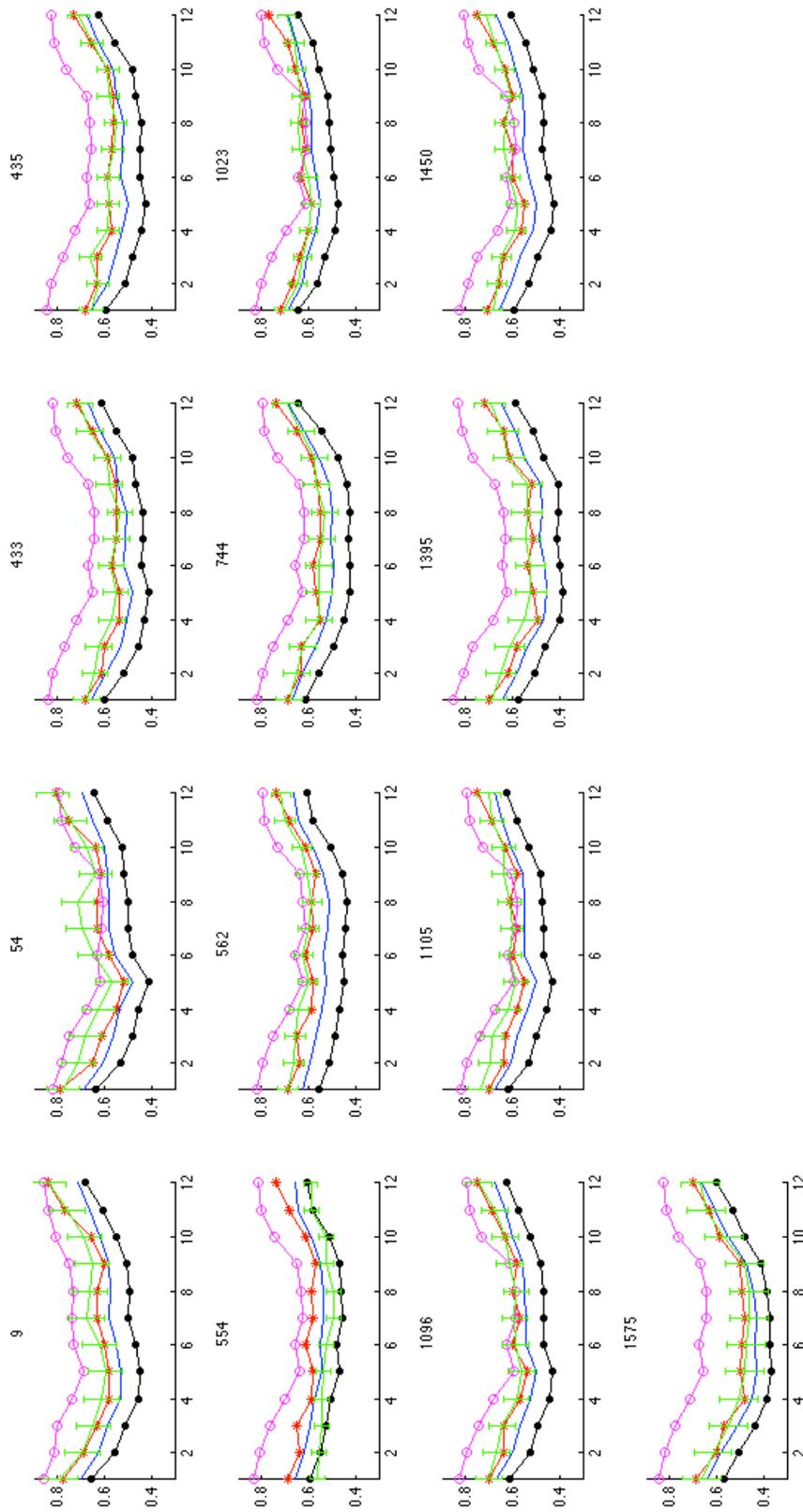
Figure 4.2: Diffuse fractions (y-axis) of various British weather stations for each calendar month (x-axis). The green solid line depicts observed data, with vertical error bars representing the standard deviation of the diffuse fractions of observed data, and all other lines represent the following models: PVGIS model (red line with asterisks), UKCP09 climate model projections for the 2020s based on low-emission scenarios (magenta line with circle), Page model (blue line) and Liu and Jordan model (black line with circles).

ation on tilted surfaces in other applications. Model output is evaluated in terms of MBE, RMSE and percentage error.

From Table 4.1, we note that for the absolute values of MBE 92% of the sites values produced by the PVGIS model are lower than those calculated from the other three models: on average they are 17%, 7% and 19% less than those of the UKCP09, Page and Liu & Jordan models, respectively. For RMSE, 100% of the sites values from PVGIS are less than those produced by the UKCP09 model by 10% on average, and 69% of the sites values from the PVGIS model are less than those from Page and Liu & Jordan models, by an average of 1% and 8%, respectively. This demonstrates that overall the PVGIS model is more accurate than the other three models.

Careful inspection reveals that 92% (Table 4.1) of the sites values produced by the Page model are lower than those computed by the UKCP09 model: on average they are respectively 8% and 11% lower for MBE and RMSE. These results imply that the Page model is more accurate than the UKCP09 model. This is surprising given that UKCP09 is based on the British observed data and a more complex concept, while the simpler Page model is based on a global dataset that is likely to be less transferrable to the UK. However, this conundrum may be explained as both the global and diffuse radiation produced by the UKCP09 model are modelled, whereas observed global radiation is used as the input data of the Page model.

A comparison of the UKCP09 and Liu & Jordan models from the MBE aspect shows that 85% of the sites using the UKCP09 model are more accurate than Liu & Jordan model, while 62% of the RMSE values based on the UKCP09 model are smaller than those based on the Liu & Jordan model (Table 4.1). On average the MBE values of the UKCP09 model are 2% smaller than those from the Liu & Jordan model; but the RMSE values of the UKCP09 model are 2% greater than those from the Liu & Jordan model. Overall, the UKCP09 model shows a better performance than the Liu & Jordan model for most tested sites; but averagely, the UKCP09 model is not significantly more accurate than the Liu & Jordan model.

All MBE values from the Liu & Jordan model underestimate the observed data,

Table 4.1: Error analyses for all available annual averaged daily British diffuse fraction data.

Station ID	MBE (Wh m^{-2})				RMSE (Wh m^{-2})			
	PVGIS	UKCP09	Page	Liu & Jordan	PVGIS	UKCP09	Page	Liu & Jordan
9	-0.021	0.093	-0.080	-0.149	0.083	0.126	0.100	0.161
54	-0.043	0.031	-0.101	-0.172	0.104	0.112	0.122	0.187
433	-0.019	0.113	-0.081	-0.154	0.091	0.147	0.102	0.165
435	-0.011	0.114	-0.073	-0.146	0.098	0.154	0.102	0.163
554	0.088	0.183	0.051	-0.017	0.150	0.220	0.118	0.126
562	-0.015	0.068	-0.067	-0.142	0.072	0.100	0.079	0.148
744	0.010	0.113	-0.034	-0.107	0.076	0.136	0.058	0.116
1023	0.012	0.070	-0.027	-0.095	0.094	0.126	0.077	0.122
1096	0.011	0.080	-0.047	-0.119	0.108	0.139	0.109	0.157
1105	0.000	0.064	-0.054	-0.125	0.122	0.144	0.125	0.172
1395	-0.012	0.136	-0.067	-0.139	0.075	0.153	0.079	0.145
1450	-0.005	0.061	-0.058	-0.133	0.077	0.113	0.081	0.144
1575	0.012	0.191	-0.030	-0.096	0.076	0.204	0.061	0.118
Mean	0.001	0.101	-0.051	-0.122	0.094	0.144	0.093	0.148
Percent error (%)	1.125	17.733	-8.027	-19.735	13.955	24.410	12.944	22.108

by 20% on average. This may imply that Britain has higher diffuse fractions than the US and Canada, bearing in mind that the Liu & Jordan model is based on the latter region. Similarly, 92% of the sites values produced by the Page model underestimate the observed data, by 8% on average, which could imply that the Britain diffuse fractions are higher than the global average on which the Page model is based. Moreover, since the underestimation of diffuse fraction from the Liu & Jordan model (20%) is greater than that from the Page model (8%), with the difference 12%. This may imply that the regression coefficients used in the Liu & Jordan model were derived based on a clearer sky than those used in the Page model. The implication is that the US and Canada have lower diffuse fractions than the global average used in the Page model. Note that these findings are limited by the fact that the global average used in the Page model is from a very restricted set of stations.

The Liu & Jordan model is apparently less accurate than the PVGIS, UKCP09 and Page models, which might be because the Liu & Jordan model was derived based on North American weather-station data rather than that from Britain or Western Europe. This discrepancy could also be due to the fact that a shade-ring correction factor was applied to all diffuse radiation data except for those recorded at Blue Hill and Massachusetts, which were used by Liu and Jordan to derive their model (Klein, 1976).

4.4   Conclusion

This work shows that the algorithm proposed by the PVGIS model performs best overall out of the four models tested here, followed by the Page, UKCP09 and Liu & Jordan models. Judging from the MBE aspect, the PVGIS model is on average 17%, 7% and 19% more accurate than the UKCP09, Page and Liu & Jordan models, respectively; judging from the RMSE aspect, the PVGIS model is on average 10%, 1% and 8% more accurate than the UKCP09, Page and Liu & Jordan models, respectively. The Page model shows a better performance than the UKCP09 and Liu

& Jordan models. The UKCP09 model has similar accuracy to the Liu & Jordan model.

Since all the MBE values produced by the Liu & Jordan model underestimate the observed data, this indicates that the diffuse radiation fraction in Britain is on average 20% higher than that in the US and Canada. Similarly, British diffuse fraction is on average 8% higher than the global level. Finally, because the Liu & Jordan model underestimates the observed data by 12% more than the Page model, this suggests that the US and Canada region may have a lower diffuse fraction than the global average. Of course these findings are limited by the fact that the global average used in the Page model is from a very restricted set of stations.

Chapter 5

Three-dimensional SOlar RAdiation Model (SORAM) and its application to 3-D urban planning

Abstract

The aim of this work is to evaluate the potential direct and diffuse solar radiation aggregated at a point location in an urban area. With the three-dimensional (3D) SOlar RAdiation Model (SORAM) presented here, the chapter makes three key contributions. Firstly, the model augments the Perez et al. (1990a) model by accounting for the aggregated contribution of diffuse radiation using ray-tracing methods. Secondly, the model demonstrates the use of a randomly generated city building distribution and terrain map to simulate the 3D urban solar radiation exposure at any time or over a selected time period. Thirdly, we validate our results using empirical sunlight data measured from a real urban area (Sheffield Solar Farm), and also validate our results against the Perez et al. (1990a) model under conditions of no shading.

This work has been published as an article in the journal *Solar Energy* (Erdélyi

et al., 2014). The authors are Róbert Erdélyi, Yimin Wang, Weisi Guo, Edward Hanna and Giuseppe Colantuono.

Keywords: 3D; shading condition; solar radiation.

5.1 Introduction

Solar radiation models are used to estimate how much solar irradiance can be collected at a location on the Earth's surface. Most existing models typically do not take into account the effects caused by urban shading (i.e. shadows cast by buildings, trees and other obstacles). The global radiation received on a point over a given time period is composed of direct radiation (i.e. that part which emanates directly from the Sun), diffuse radiation (the other part that is scattered by the Earth's atmosphere) and reflected radiation (reflected by obstacles surrounding the location). In most cases, the reflected radiation is negligible (HEMI, 2000) and is therefore ignored here.

5.1.1 Motivation

A sustainable city needs to generate a large fraction of its energy consumption using renewable energy sources. Large-scale photovoltaic (PV) solar-energy installations are seen as a potential solution for future cities (Hofierka and Kanuk, 2009). Grid-connected PV systems can aid peak shaving, minimize transmission and distribution losses and increase grid capacity since they generate electricity close to, or even at the consumers' point of use. Especially in great commercial areas, daytime peak load profiles are consistent with solar generation profiles (da Silva Jardim et al., 2008). Accurate local-scale (e.g. city-wide) models of both the spatial and temporal distributions of solar radiation are needed. The aim of this chapter is to provide a working model for estimating the total solar energy received at a point on a sloping PV cell surface, particularly those that are subject to intermittent shading from

urban terrain. The model we develop is a key enabler for the efficient deployment of PV panels at both the street level and on the walls of buildings. In order for a sustainable city or householder to determine the position, size, optimised slope and azimuth angles of PV installations, this model can be implemented to display the solar radiation distribution for each point on a surface (e.g. roof, walls and ground etc.) of a city or house. Moreover, this model can solve the problem raised in Fartaria and Pereira (2013), which is how to calculate shadow losses caused by 2-axis moving PV module trackers in PV collector fields.

5.1.2 Review

In the literature several solar-radiation software tools and models have been established. The most widely used software tools are the ArcGIS Solar Analyst (ArcGIS, 2012), the GRASS GIS r.sun (Šuri and Hofierka, 2004; Hofierka and Zlocha, 2012), the PVSYST (2013) and PV*Sol (2013). The main drawback of the ArcGIS Solar Analyst is that by using stereographic projection, the whole sky is projected as a flat circle, with inevitable geometric inaccuracies due to the spatial distortion during the translation from 3D to 2D. The description of the methodology of the GRASS GIS r.sun can be found in the article by Šuri and Hofierka (2004) with further extension from 2D to 3D version in Hofierka and Zlocha (2012). GRASS GIS r.sun and PVSYST assume an isotropic sky for diffuse radiation. Although this simplification is easy to use, it is imprecise and several anisotropic sky models have been shown to be more accurate (Muneer, 2004). PV*Sol is designed for the calculation of shadows cast only by static obstacles (Fartaria and Pereira, 2013).

There are other models and algorithms used to calculate shading losses like Perpinan (2012), Navarte and Lorenzo (2008) and Lorenzo et al. (2011), which compute shadow shapes with dimensions for each position of the Sun, followed by a calculation of multiple shadows' joint effect. This method is usually complicated as the intersection of the shadows is too complex to calculate and can lead to errors when

simplifications are made Fartaria and Pereira (2013). Similarly, Fartaria and Pereira (2013) computes shadow losses caused by 2-axis moving PV module trackers. Their paper considers the shaded fraction of the PV array area affected by the shading. This method is precise when considering only PV collector fields that are obstructed by simple regular geometric shapes, but can not adequately cope with complex or combined shapes that are found in urban areas.

In other literature, Melo et al. (2013) and Redweik et al. (2013) also estimate shadow losses at PV surfaces, but when calculating diffuse radiation by using diffuse shading factor in Melo et al. (2013) or the sky view factor in Redweik et al. (2013), they do not consider the angle of incidence of solar energy contribution from each sky segment. Under the diffuse radiation framework employed in Melo et al. (2013) and Redweik et al. (2013), provided that all the obstacle dimensions are the same, their orientation with respect to the PV cell is not important. Our work improves on this by attempting to refine the Perez et al. (1990a) model, enabling it to calculate the angle of incidence for each diffuse ray.

Alternative methods, such as that adopted by Orioli and Gangi (2012), use photographs taken on site to determine the level of shadowing. However, this is not efficient for real-time planning at the city scale. Similarly, the software SOLCEL (Yoo, 2011) is efficient for evaluating a shading/sunlit area on a solar cell module. However, the SOLCEL uses the method from Quaschning and Hanitsch (1998) to calculate the shaded area on a PV module, which requires a survey of the surroundings using optical instruments, such as fisheye camera. This method is only valid for one observer point (Quaschning and Hanitsch, 1998). Therefore, the SOLCEL is not applicable for large PV systems planning like the city scale. The Nguyen and Pearce (2012) algorithm is based on 2.5D raster data, which limits consideration to roofs but not walls or the reflected component of global radiation. However, Redweik et al. (2013) found the solar radiation incident on the walls is lower than that on the roofs, but due to their large collective area, walls are a significant part of the solar-energy potential in urban areas.

5.1.3   Contribution

In the first part of this chapter, we present a 3D SOlar RAdiation Model (SORAM) that builds on the improved Perez et al. (1990a) model, the Reindl et al. (1990) model and Sun-Earth trigonometric relationship models from Duffie and Beckman (1991), and also uses a ray-tracing method (Shirley et al., 2005; Mena-Chalco, 2010), which is not subject to the above limitations. SORAM divides the sky into a large number (typically thousands) of uniformly-spaced sectors. This is in contrast with the well-known Perez et al. (1990a) model which calculates the contribution of diffuse radiation from three different regions of the sky (horizon band, circum-solar and the rest of the sky), and has previously been shown to perform well in model inter-comparison studies (Muneer, 2004; Noorian et al., 2008). The first modelling novelty is that we combine a ray-tracing method (Shirley et al., 2005; Mena-Chalco, 2010) with the adjusted Perez et al. (1990a) model to determine whether a solar ray (direct or diffuse), can reach a PV cell location in the 3D terrain map. The angle of incidence of each solar ray is taken into account since for a sloping surface, each solar ray from the sky contributes different amounts of solar energy.

In SORAM, we also utilize the model developed by Reindl et al. (1990) to split measured values of hourly global radiation into its direct and diffuse components. The data thus derived are then corrected for the inclined plane of the PV cell by taking into account geometry (i.e. solar altitude, solar azimuth, and azimuth and elevation of the PV cell), as well as the shadows projected by surrounding objects. By aggregating the direct and diffuse radiation from all the points taking into account the angles of incidence in the sky that are not obstructed by obstacles, SORAM can accurately obtain the tilted global radiation received by a sloping PV cell over any period of time, from one hour to one year. We validate our results both against the well-known Perez et al. (1990a) model without terrain obstacles, and against the global radiation measured by the sensors surrounded by real urban obstacles (The Sheffield Solar Farm, 2013).

Different from GRASS GIS r.sun and PVSYST, SORAM calculates solar radiation receipt based on an anisotropic sky. Also, unlike Melo et al. (2013) and Redweik et al. (2013), SORAM takes into account the angle of incidence of each sky segment by deducing the solar-energy contribution for each segment separately, based on the Perez et al. (1990a) model for the calculation of diffuse radiation.

SORAM also has several ways of enabling greater future scalability than the other software tools and models mentioned above. The first advantage is because the segment of the sky in SORAM is modular. Therefore, in order to increase modelling accuracy of the anisotropic nature of diffuse radiation, SORAM can be easily scaled to incorporate a more sophisticated method and/or increase the spatial resolution of sky segment. The second advantage of SORAM is that because it uses the angle of incidence from the Sun to a point on a PV cell for each solar (direct and diffuse) ray, it can be used to calculate the solar radiation received by various shapes of panel element such as a cylinder (which is already used in the solar PV industry) and is not limited to just a flat plane surface (McIntosh et al., 2007; Colantuono et al., 2013); in other words, various models of solar concentrators can be embedded into SORAM to operate a comprehensive optimization analysis. However, here, for simplification and because it is widely employed in industry, we just use a flat plane surface in our analysis. The third advantage of SORAM is that since a 2-axis PV tracker moves according to the position of the Sun, meaning that the tracker's coordinates are available, SORAM can easily calculate shading losses resulting from other trackers in the PV collector field. The fourth advantage is that SORAM can evaluate the received solar radiation for any point on the map, meaning that spatial resolution is limited only by computational power. Therefore, SORAM has the potential to determine the percentage of the shading on a PV module. When the coordinates for each point on the PV module are calculated, SORAM is capable of evaluating partial shading.

It is also worth noting that in the field of radio-communications (Boithais, 1987), a number of tools have been developed which predict the propagation of electro-

magnetic waves (Atoll, 2013). Despite the common electromagnetic nature of radio-communication waves and solar rays, there are some fundamental differences when considering propagation:

1. Propagation Path: radio waves are emitted from devices on Earth's surface, whereas solar rays come from a single source in the sky and are parallel. Therefore, radio wave propagation deals mainly with how waves reflect and penetrate structures, whereas solar ray propagation is affected by atmospheric effects as well as how rays intersect ground-level obstacles;

2. Frequency: radio wave propagation ($\sim 10^9$ Hz) can be treated as a wave model, whereas visible solar ray propagation ($\sim 10^{15}$ Hz) is treated as a ray model.

Therefore, the contribution of this chapter overlaps to a certain extent with radio-wave propagation research, but is fundamentally different in the aforementioned areas. The common aspects may be important for radio-wave flux estimates in an urban environment.

5.2   The 3D urban environment

This section describes the 3D urban environment used to demonstrate our proposed methodology. The solar position data in terms of hourly solar altitude, solar azimuth, angle of incidence on a PV cell's surface, and daily solar duration are computed by SORAM based on models found in Duffie and Beckman (1991). Figure 5.1 outlines the overall structure of the model flowchart that underpins this body of work. In this figure, the solar altitude, solar azimuth, solar duration and angle of incidence are derived using the solar geometry algorithm summarized in Figure 5.2. The parameters marked as "daily" are daily values, otherwise they are hourly values.
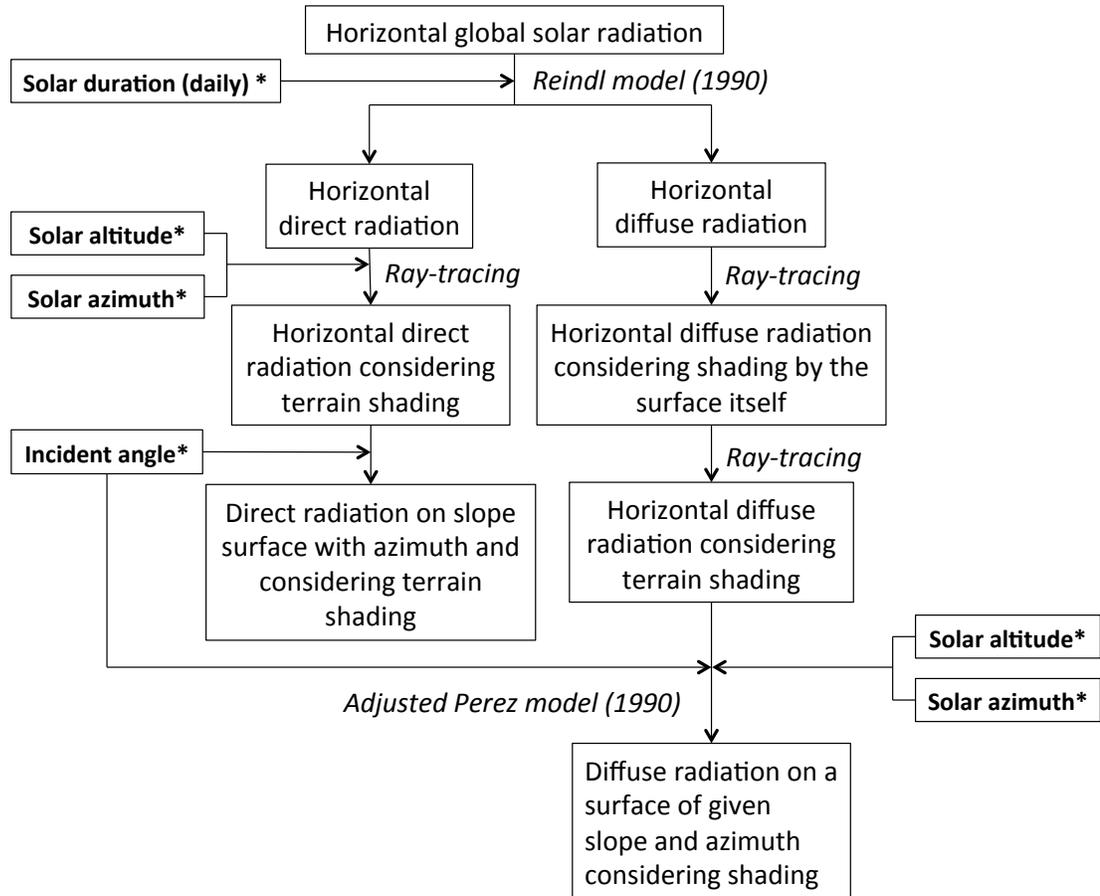
Figure 5.1: Flowchart of SORAM. Solar altitude, solar azimuth, solar duration and angle of incidence are derived from the process summarized in Figure 5.2. The parameters marked as "daily" are daily values, otherwise hourly values.
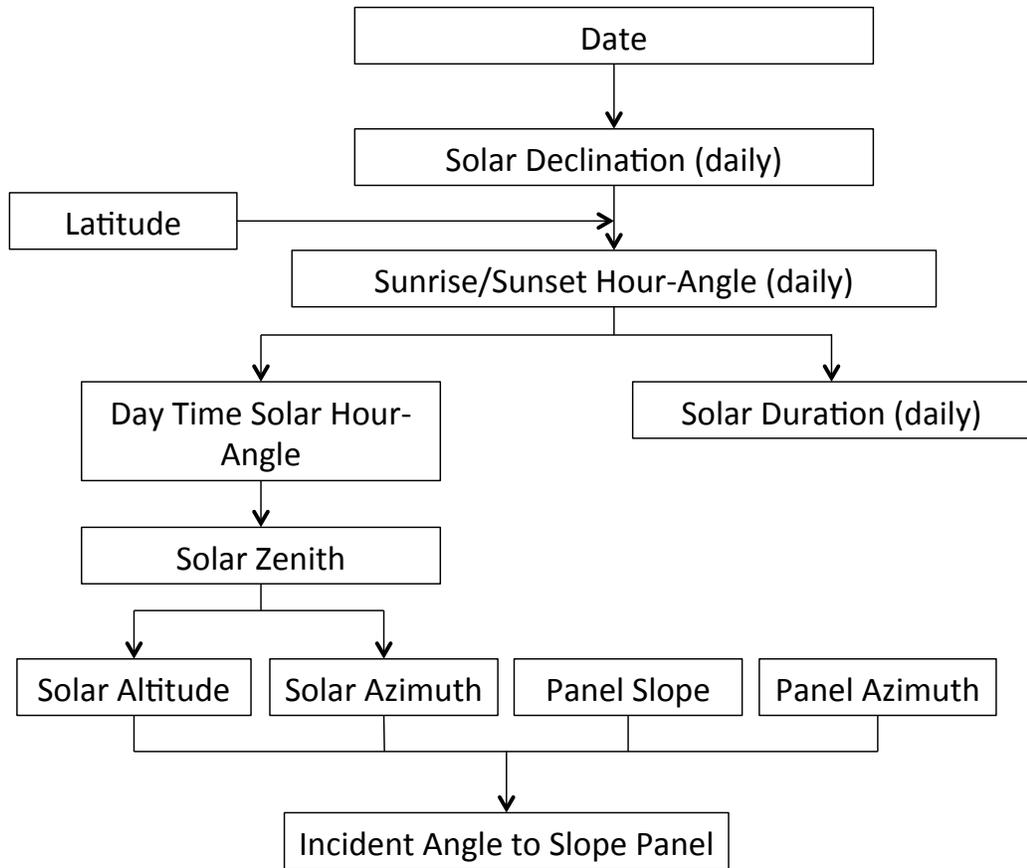
Figure 5.2: Flowchart of the solar geometry calculation used to derive solar altitude, solar azimuth, solar duration and angle of incidence. The parameters marked as "daily" are daily values, otherwise hourly values.

5.2.1 Mechanism of the coordinate system of SORAM

Since we need to embed obstacles (buildings/trees) into SORAM, and detect their shading using ray-tracing method, which is easily built on Cartesian coordinate system, we choose x/y-axes representing the position of obstacles and z-axis representing the height of them. Therefore, our z-axis extends from the Earths center through the location in question. Because we use south as our zero reference, y-axis points from the Earths center toward the South Pole. In order to keep the right-handed coordinate system valid, x-axis points from east to west.

5.2.2 Direct and Diffuse radiation

For each day, the sunrise time is determined and solar radiation data from that point onwards are integrated until sunset. This is to avoid unnecessary calculations for the night-time hours, to save computation time. Horizontal direct and diffuse radiation data are required to estimate global radiation on a PV cell of a given slope and azimuth. Global solar radiation received by a PV cell can be decomposed into direct and diffuse components. Although horizontal global radiation data are commonly available, horizontal direct and diffuse radiation are scarcely measured variables because of costs; therefore, the widely used model developed by Reindl et al. (1990) is embedded into SORAM to predict hourly direct and diffuse radiation from hourly global radiation on a horizontal PV cell.

Sections 5.3 and 5.4 outline the algorithm that estimates direct and diffuse radiation on a PV cell of given slope and azimuth from their counterparts on a horizontal PV cell considering surrounding shading conditions. In SORAM, for visualization and demonstration, a PV cell can be represented by an arbitrary area, which is taken to be a triangle in this particular chapter. As shown in Figure 5.3, the plan and portrait view of a PV cell are represented by a triangle in a hypothetical city in SORAM. The red dots on the PV cell represent the diffuse rays with their angles of incidence smaller than 0° or greater than 90°.
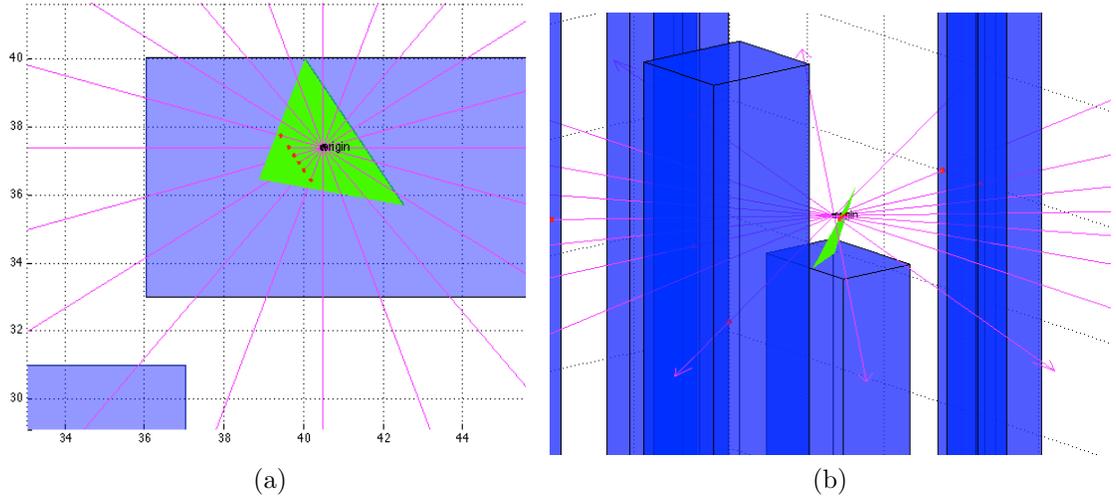
Figure 5.3: The red dots on the PV cell represent the diffuse rays with $\theta_d \leqslant 0°$ or $\theta_d \geqslant 90°$. (a) Plan view of a PV cell represented by a triangle in a hypothetical city in SORAM; (b) portrait view of (a).

The angle of incidence of each solar ray is calculated using a solar geometry sub-function, and the resulting flowchart is shown in Figure 5.2. The angle of incidence at a given time is assumed constant for the whole map area. The parameters defining the position of the Sun in the sky are calculated on a daily or hourly basis; a list of them can be found in Table 5.1. For more details, see Duffie and Beckman (1991).

5.2.3 Shading algorithm

In order to simulate a random urban setting, a number of obstacles (buildings/trees) are incorporated with stochastic width, length and height dimensions, with boundaries of $[1, 10]$, $[1, 10]$ and $[1, 50]$ meters respectively (i.e. these values are randomly varied in 1-m increments within these ranges). The aim of using these boundaries is to obtain a realistic representation of the city and solar radiation distribution for visualization. When we incorporate a real urban plan into SORAM, these hypothetical boundaries are no longer necessary. In this work, trees are considered as solid obstacles and their solar energy potential is not considered. The dimension for each building/tree is described by using its two-set Cartesian coordinates in this 3D envi-

Table 5.1: Nomenclature used in this chapter

Parameter Name	Parameter	Range
Angle of incidence from direct radiation	θ	$0° - 90°$
Angle of incidence from diffuse radiation	θ_d	$0° - 90°$
Solar altitude	α_s	$0° - 90°$
Solar azimuth	γ_s	$-180° - 180°$
Diffuse-ray altitude	α_d	$0° - 90°$
Diffuse-ray azimuth	γ_d	$-180° - 180°$
Surface slope angle	s	$0° - 90°$
Surface azimuth angle	γ	$-180° - 180°$
Horizontal direct radiation	B_h	$0 - \infty$
Slope direct radiation	B_s	$0 - \infty$
Horizontal diffuse radiation	D_h	$0 - \infty$
Slope diffuse radiation	D_s	$0 - \infty$
Diffuse radiation (main)	T_m	$0 - \infty$
Diffuse radiation (horizon)	T_h	$0 - \infty$
Number of solar ray (main)	n_m	$0 - \infty$
Number of solar ray (horizon)	n_h	$0 - \infty$
Diffuse radiation contribution coefficient (main)	1	1
Diffuse radiation contribution coefficient (circum-solar)	F_1	$0 - \infty$
Diffuse radiation contribution coefficient (horizon)	F_2	$0 - \infty$

ronment, i.e. (x, y, z) and (x+width, y+length, z+height). These random obstacles are also randomly placed on a 100×100 m^2 map showing their distribution. Results are sampled at a 1×1 m spatial resolution on this map. Solar altitude varies between $[0°, 90°]$, and the solar azimuth angle ranges between $-180°$ and $180°$ with $0°$ due south, where east is negative and west is positive. The time-step size depends on the resolution at which solar radiation is observed. Hourly temporal resolution is sufficient for most applications (Hofierka and Zlocha, 2012), and is consequently adopted in this work.

Ray-tracing (Shirley et al., 2005; Mena-Chalco, 2010) is used in this work to determine if a solar ray is shaded by an obstacle. Shirley et al. (2005) considered an intersection between a 2D ray vector and a rectangle, which can be generalized to between an arbitrary 3D ray and a voxel. Mena-Chalco (2010) implemented the ray-tracing algorithm for detecting if a 3D ray vector intersects with a box (voxel).

In our ray-tracing algorithm, contrary to real conditions, a PV cell (i.e. a tested point in the 3D urban environment) is regarded as a source emitting rays to the sky segments. The position of the 3D ray vector on the 3D urban environment is determined by the Cartesian coordinates of the tested point; the direction of the 3D ray vector is represented by the hourly altitude (α) and azimuth (γ) of direct/diffuse radiation rays, i.e. $(\sin(\gamma_s), \cos(\gamma_s), \tan(\alpha_s))$ or $(\sin(\gamma_d), \cos(\gamma_d), \tan(\alpha_d))$. The subscripts s means direct solar radiation, and d means diffuse solar radiation. The ray-tracing method is then used between the 3D ray vector and each obstacle. Once an intersection is detected, the distance between the PV cell and the intersection is calculated. A positive distance means the intersection is between the PV cell and the sky, otherwise a negative distance represents an invalid intersection and is discarded.

5.3   Direct radiation

To predict the tilted direct radiation, a point for mounting a PV panel in SORAM is chosen, called the *origin*. Hourly direct radiation is treated as a ray emanating from the Sun towards of the *origin*. θ is the angle of incidence, i.e. the angle between the direct radiation on a PV cell surface and the normal to that surface.

If $\theta < 0°$ or $\theta \geqslant 90°$, hourly amount of direct radiation associated with the solar ray is excluded from the integration, i.e. $B_s = 0$. Whereas, if $0° \leqslant \theta < 90°$, the ray-tracing algorithm is used to determine whether the direct ray intersects with buildings that are taller than the vertical height of the *origin*. If there is an intersection, $B_s = 0$; if the direct ray is not obstructed by any building, the tilted hourly direct radiation can be estimated by:

$$
\begin{aligned}
B_s &= B_h \frac{a_0}{a_1}, \\
a_0 &= \max(0, \cos(\theta)), \\
a_1 &= \max(\cos(85°), \cos(\frac{\pi}{2} - \alpha_s)).
\end{aligned}
\tag{5.1}
$$

where B_s and B_h are the hourly direct radiation on a sloping and horizontal PV cell, respectively, α_s is the solar altitude angle. For more details of these variables, see Duffie and Beckman (1991).

5.4 Diffuse radiation

In this section, we describe how SORAM converts diffuse radiation from horizontal surface to the sloping one while taking shading into account. As previously mentioned, the Perez et al. (1990a) model has demonstrated strong agreement with empirical data. In SORAM, the Perez et al. (1990a) model is further developed to take shading due to obstacles into account.

5.4.1 Augmenting the Perez et al. (1990a) model with Ray-Tracing

It is observed that, in the atmosphere, there are two main zones causing the anisotropic nature of diffuse radiation: i) circumsolar brightening resulting from forward scattering by aerosols, and ii) horizon brightening mostly caused by multiple Rayleigh scattering and retro-scattering in a clear atmosphere (Kano, 1964). In the Perez et al. (1990a) model, the circumsolar disk and horizon band are superimposed on the sky hemisphere, creating three distinct isotropic zones (Perez et al., 1987).

In the model proposed by Perez et al. (1990a), for simplicity it is assumed that all circumsolar energy is emitted from a point centred on the Sun's position, and the horizon band originates from an arc of a great circle at the base of the atmosphere. The horizon band in SORAM is a great circle that is at the same height as the *origin*, and because it is naturally level with the *origin*, it has no effect on a horizontal PV cell centred on the *origin*.

Without any terrain shading, the relationship between diffuse radiation on a slop-

ing PV cell and a horizontal one may be written as (Perez et al., 1987, 1990a):

$$D_s = D_h \left[(1 - F_1) \frac{1 + \cos(s)}{2} + F_1 \frac{a_0}{a_1} + F_2 \sin(s) \right]. \qquad (5.2)$$

where D_s and D_h are the hourly diffuse radiation on a sloping and horizontal PV cell, respectively, a_0 and a_1 have the same definition as in Equations 5.1, s is the slope angle of a PV cell, F_1 and F_2 are the diffuse radiation contribution coefficients for the circumsolar and horizon zones, respectively. They are normalised by the diffuse radiation contribution coefficient for the main zone. Therefore, $(1 - F_1)$ is the ratio of diffuse radiation on a horizontal PV cell from the main zone to the whole sky.

Because of the homogeneity of the three aforementioned sky zones, applying the Perez et al. (1990a) model to SORAM and assuming the total diffuse radiation from the main zone is T_m, the number of those diffuse rays is n_m, we note that:

$$1 - F_1 = \int_{-\pi}^{\pi} \int_0^{\frac{\pi}{2}} \frac{T_m}{n_m} \sin(\alpha_d) \, d\alpha_d d\gamma_d, \qquad (5.3)$$

where α_d and γ_d are the altitude and azimuth angles for each diffuse ray, respectively. Thus, the diffuse radiation contribution of each ray in the sky is,

$$
\begin{aligned}
\frac{T_m}{n_m} &= \frac{1 - F_1}{\int_{-\pi}^{\pi} \int_0^{\frac{\pi}{2}} \sin(\alpha_d) \, d\alpha_d d\gamma_d}, \\
&= \frac{1 - F_1}{2\pi}, \qquad (5.4)
\end{aligned}
$$

Moreover, the angle of incidence of a diffuse ray is

$$
\begin{aligned}
\cos(\theta_d) &= \cos\left(\frac{\pi}{2} - \alpha_d\right) \cos(s), \qquad (5.5) \\
&\quad + \sin\left(\frac{\pi}{2} - \alpha_d\right) \sin(s) \cos(\gamma_d - \gamma),
\end{aligned}
$$

where γ is the azimuth angle of a PV cell.

Therefore, without any terrain shading, the diffuse radiation from the main zone

both on the front and back of a sloping PV cell is,

$$\int \frac{T_m}{n_m} \cos\left(\theta_d\right) d\theta_d,$$

$$= \frac{1 - F_1}{2\pi} \cos\left(s\right) \int_{-\pi}^{\pi} \int_0^{\frac{\pi}{2}} \sin\left(\alpha_d\right) d\alpha_d d\gamma_d,$$

$$= (1 - F_1) \cos\left(s\right). \tag{5.6}$$

This part of the diffuse radiation contribution is for the whole main zone of the sky. This means when a diffuse ray comes from back of a PV cell ($\theta < 0°$ or $\theta > 90°$), a negative value contributes to this integration, which should be zero. Thus, the diffuse radiation contribution shaded by a PV cell needs to be added, which is,

$$(1 - F_1)\frac{1 - \cos\left(s\right)}{2}. \tag{5.7}$$

Therefore in reality, when there is no terrain shading, the diffuse radiation from the main zone on a sloping PV cell is,

$$(1 - F_1) \cos\left(s\right) + (1 - F_1)\frac{1 - \cos\left(s\right)}{2},$$

$$= (1 - F_1)\frac{\cos\left(s\right) + 1}{2}. \tag{5.8}$$

which satisfies Perez et al. (1987, 1990a) as shown in Equation 5.2. Note that in SORAM, the part of diffuse radiation contribution comes from back of a PV cell is detected and set to be zero.

Similar to the direct radiation, the conversion of horizontal to inclined diffuse radiation from the circumsolar zone is,

$$F_1\frac{a_0}{a_1}. \tag{5.9}$$

Assuming the total diffuse radiation from the horizon zone is T_h and the number

of those diffuse rays is n_h, we have:

$$
\begin{aligned}
F_2 \sin(s) &= \int \frac{T_h}{n_h} \cos(\theta_d) \, d\theta_d, \tag{5.10} \\
&= \frac{T_m}{n_m} \int_{\gamma - \frac{\pi}{2}}^{\gamma + \frac{\pi}{2}} \sin(s) \cos(\gamma_d - \gamma) \, d\gamma_d,
\end{aligned}
$$

Thus,

$$
\frac{T_h}{n_h} = \frac{F_2}{\int_{\gamma - \frac{\pi}{2}}^{\gamma + \frac{\pi}{2}} \cos(\gamma_d - \gamma) \, d\gamma_d}. \tag{5.11}
$$

To sum up, for each diffuse ray in the main, circumsolar and horizon zone, the energy contributions are

$$
\frac{1 - F_1}{\int_{-\pi}^{\pi} \int_0^{\frac{\pi}{2}} \sin(\alpha_d) \, d\alpha_d d\gamma_d} \cos(\theta_d), \tag{5.12}
$$

$$
F_1 \frac{a_0}{a_1}, \tag{5.13}
$$

$$
\frac{F_2}{\int_{\gamma - \frac{\pi}{2}}^{\gamma + \frac{\pi}{2}} \cos(\gamma_d - \gamma) \, d\gamma_d} \cos(\theta_d). \tag{5.14}
$$

5.4.2 Shading from Slope Surface and Terrain

Method I: angle of incidence and ray-tracing

Figures 5.3 and 5.4 show an arbitrary example where the triangle represents a PV cell with a slope of 50° and an azimuth angle 60° in SORAM. A half sphere with altitude $\alpha_d \in [0°, 90°]$ and azimuth $\gamma_d \in [-180°, 180°]$, respectively, is centred on the *origin*. Vectors in Figures 5.3 and 5.4 represent twenty diffuse rays $(\alpha_d = 0°)$.

Let the number of vectors when $\alpha_d = 0°$ be N. To guarantee the uniform representation of the sky, the number of vectors for any elevation should be $N \cos(\alpha_d)$. It is worth noting that as the slope angle increases, the number of independent vectors converges to one.

There are two kinds of shading: one results from the sloping PV cell itself, and
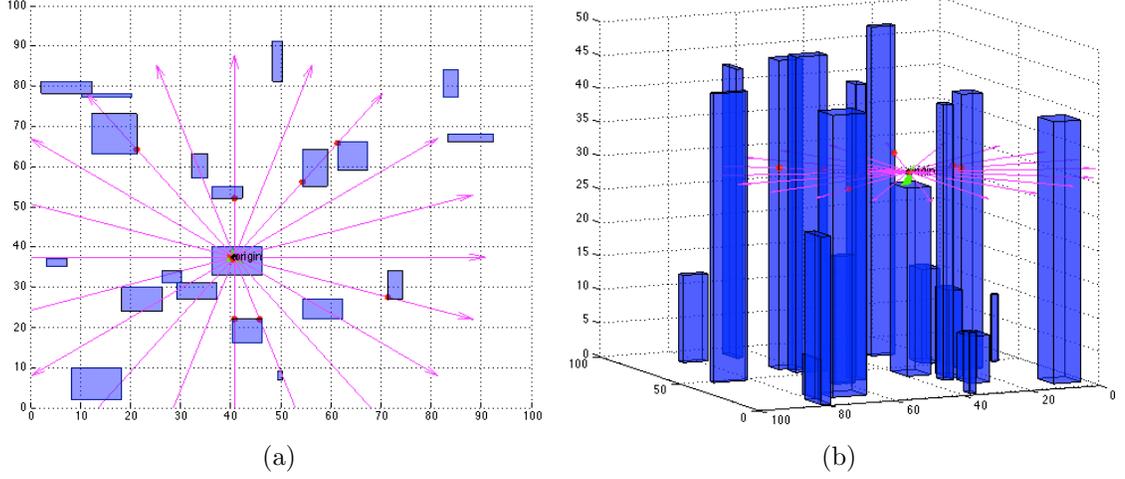
Figure 5.4: The red dots on buildings mean the diffuse ray intersect a building and are therefore not collected by the PV cell; while the red dots on the PV cell represent the diffuse rays with $\theta_d \leqslant 0°$ or $\theta_d \geqslant 90°$. (a) Plan view of a hypothetical city in SORAM; (b) portrait view.

the other is from surrounding obstacles including buildings. If $\theta_d < 0°$ or $\theta_d \geqslant 90°$, $D_s = 0$. Whereas, if $0° \leqslant \theta_d < 90°$, ray-tracing algorithm is used to determine whether or not the diffuse ray intersects with buildings. If there is an intersection, $D_s = 0$; otherwise, if a diffuse ray emanates from the main, the circumsolar or the horizon zone, this ray's energy is given by Equation 5.12, 5.13 or 5.14, respectively, and is therefore integrated to the diffuse portion, see Figure 5.4.

Method II: triangle PV panel by ray-tracing

In the 3D environment, a triangle representing a PV cell can be located at any position in SORAM simulation for any given slope and azimuth angle. An arbitrary example with a slope of $50°$ and an azimuth angle $60°$ is shown in Figures 5.3 and 5.4. We define a test point (the *origin*) at the centroid of the triangle (not inside the material). Vectors in Figure 5.3 and 5.4 represent 20 unique diffuse rays ($\alpha_d = 0°$). The methodology used to calculate the coordinates of the triangle in the SORAM is described in Section 5.A.

Let the number of vectors when $\alpha_d = 0°$ be N, to guarantee the uniform repre-

sentation of the sky, the number of vectors for any elevation should be $N \cos(\alpha_d)$. It is worth noting that as the slope angle increases, the number of independent vectors converges to one.

As the simulation program loops through each diffuse ray uniformly distributed in the sky, if both α_d and γ_d of a diffuse ray are within the solid angle of the step size of the loop centred on the Sun's position, this diffuse ray is attributed to the circumsolar zone n_c; while, if $\alpha_d = 0°$, in order to satisfy using an arc of a great circle to represent the horizon band, one ray is added to the number of rays n_h; otherwise, the remaining diffuse rays belong to the isotropic zone (rest of the sky), and hence n_i is added one more portion.

There are two kinds of shading: one results from the sloping PV cell itself, and the other is from surrounding obstacles or buildings. Hence, two steps are used to determine the portion of diffuse radiation collected by a sloping PV cell. Therefore, the ray-tracing computer algorithm is applied twice.

First, the algorithm detects if there is an intersection of a diffuse ray with the triangle, for example as shown in Figure 5.3, there are in total 20 diffuse rays (denoted by the magenta vectors), six of which go to the back of the PV cell with six intersections (denoted by the red dots), and the remaining fourteen diffuse rays might succeed in reaching the PV cell if they do not hit any building.

Second, those diffuse rays which might reach the PV cell are detected one by one by the ray-tracing algorithm, which shows whether and where there are intersections with buildings. As shown in Figure 5.4, the red dots on buildings mean the diffuse ray intersect a building and are therefore not collected by the PV cell.

For each diffuse ray which reaches the PV cell, the simulation evaluates which region of the isotropic, the circumsolar or the horizon band it belongs to. If a diffuse ray emanates from the circumsolar zone, this ray's energy (as in Equation 5.13) is added to the diffuse portion. However, if the ray is emitted by the horizon band then the energy (derived from Equation 5.14) is added. Likewise, if it comes from the isotropic region then the amount of energy is given by Equation 5.12.

Finally, when all diffuse rays are aggregated, the diffuse portion is multiplied by the hourly observed horizontal diffuse radiation to obtain the tilted diffuse radiation. This is then added to the direct radiation calculated from Section 5.3 at the same time-step to obtain the tilted global radiation.

The difference of the power output from these two methods for evaluating shading is smaller than the level of 10^{-3}.

5.5 Results and Evaluation

5.5.1 Hypothetical results

Integrating results from the above calculations for a certain time period for each point on the map, a contour plot is constructed, as shown in Figure 5.5. Figure 5.5a shows stacked contours for a sequence of height levels spaced by 20 m, in each case considering shading from the hypothetical distribution of buildings. Next, Figure 5.5b with its chosable parameters (height, slope and azimuth) displays the solar radiation distribution on the ground due to shading with its chosable parameters.
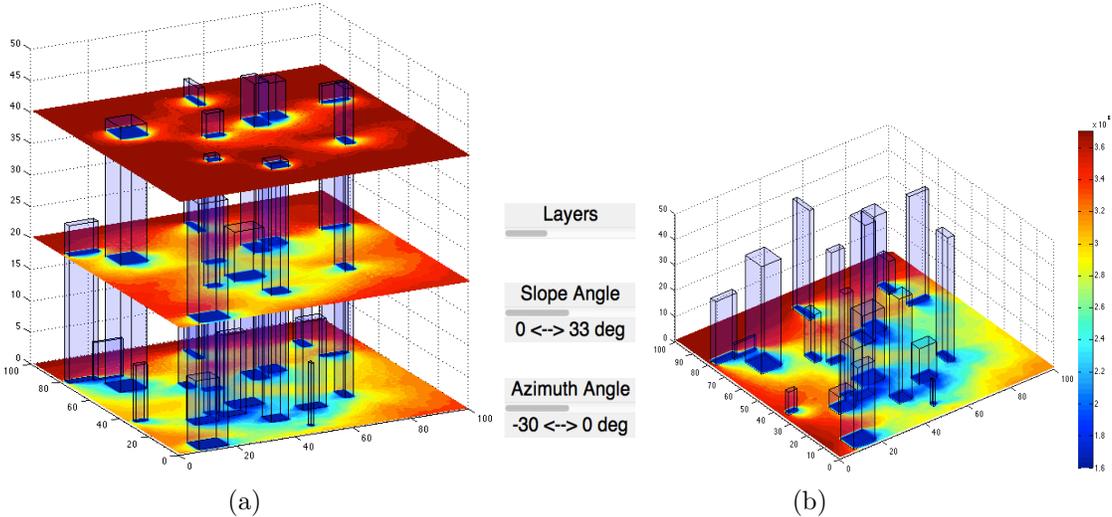
Figure 5.5: Solar radiation distribution in the hypothetical city introduced in Figure 5.4 computed by SORAM: (a) contours on various heights; (b) contours with chosable parameters: height, slope and azimuth angles of PV cells.

SORAM can also deduce the optimised slope and azimuth angle for any selected location in a city. This is accomplished by repeatedly running SORAM for a given range of slope and azimuth angles.

5.5.2 Evaluation of SORAM

The Sheffield Solar Farm (SSF) is part of Project Sunshine operating at the University of Sheffield, UK, allowing real-world testing of photovoltaics. Nine months of hourly global radiation data were collected by the SSF with two different pyranometers at a 12.7° tilt, 45° southeast facing and 45° southwest facing, respectively. Figure 5.6a shows a Google Map's image of the Hicks Building at the University of Sheffield, UK and the resulting map in SORAM. The green triangle represents the position of the pyranometer from the Sheffield Solar Farm. Figures 5.6b and 5.6c show a graphical sketch of how SORAM takes obstacles into account when determining the amount of diffuse radiation reaching the pyranometer. The blue lines represent the edges of surrounding buildings that can cast shadows on the green triangle representing the pyranometer position. The magenta vectors in Figure 5.6b and 5.6c indicate the part of diffuse radiation when the slope angle of the pyranometer (green triangle) is 12.7°, and the actual stepsize of azimuth used in SORAM is one-tenth or smaller than shown in this figure. Figure 5.7 shows the global radiation distribution over the sampled area around Hicks building. The blue lines in Figures 5.7a and 5.7b depict the edges of buildings of the sampled area based on a Google Map and SORAM. All the obstacles such as buildings and trees are approximated by voxels. Figure 5.7c displays the 3D simulation of global radiation distribution at heights of 0 m and 11.3 m over area defined in Figures 5.7a and 5.7b, based on SORAM and accounting for the various buildings present.

The performance output of SORAM is shown in Tables 5.2 and 5.3. The evalua-
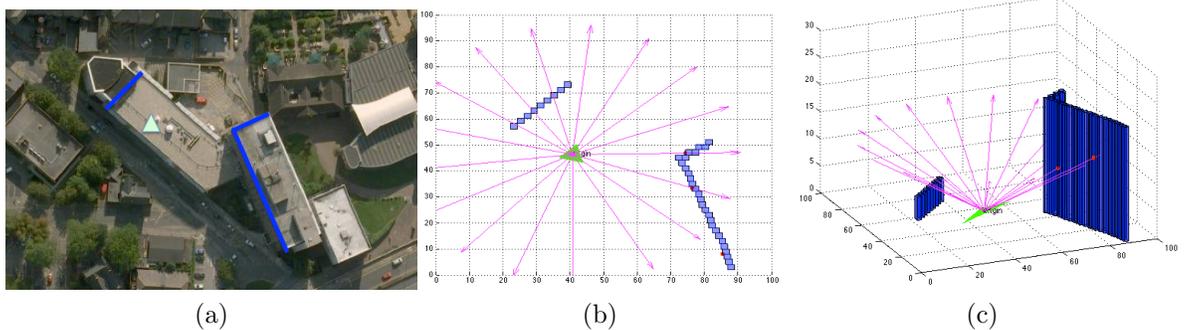
Figure 5.6: (a) GoogleMap's image of the Hicks Building at the University of Sheffield, UK; the green triangle represents a PV cell (i.e. the position of the pyranometer from the Sheffield Solar Farm); (b), (c) A graphical sketch of how SORAM takes obstacles into account when determining the amount of diffuse radiation reaching the PV cell.

Table 5.2: Output performance of SORAM vs the Perez et al. (1990a) model. The output is the ratio of diffuse radiation on a sloping PV cell to a horizontal one. The minus sign in MBE means the output from SORAM underestimates that from the Perez et al. (1990a) model.

Orientation	Mean	MBE	RMSE
45°SE	1.1	-2.8 $\times 10^{-5}$	1.9 $\times 10^{-4}$
45°SW	1.0	-4.9 $\times 10^{-5}$	5.3 $\times 10^{-4}$
Percent error		-3.6 $\times 10^{-3}$%	3.4 $\times 10^{-2}$ %

tion includes the mean bias error (MBE), given by

$$\text{MBE} = \frac{\sum_n(\text{model}_i - \text{measured}_i)}{n}, \tag{5.15}$$

where n is the number of data points and i denotes a given event, and root mean square error (RMSE),

$$\text{RMSE} = \left\{ \frac{\sum_n(\text{model}_i - \text{measured}_i)^2}{n} \right\}^{0.5}. \tag{5.16}$$

Experiments about the step sizes of α_d and γ_d have been done in SORAM, i.e. resolution of the segment of the diffuse radiation from the sky. The differences of MBE and RMSE between experiments should be smaller than 1%, because 1% in-
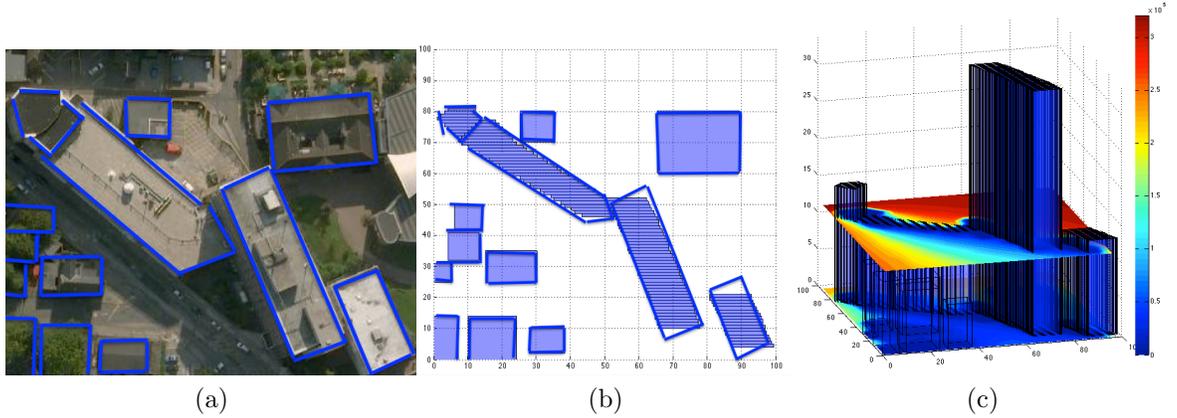
Figure 5.7: (a) GoogleMap image of Hicks Building and its immediate surroundings at the University of Sheffield, UK; (b) plan view of (a); (c) 3D simulation of global radiation distribution at heights of 0 m and 11.3 m over area defined in (a) and (b), based on SORAM described in main text and accounting for the various buildings present. The blue lines in (a) and (b) depict the margins of buildings of the sampled area both from a Google Map and SORAM. All the obstacles such as buildings and trees are approximated by voxels.

crease/decrease is very important in PV industry. Without any terrain shading, the MBE and RMSE are calculated in the way that SORAM produces the modelled data, and the output from Perez et al. (1990a) model is treated as the measured data. In this case, the maximum step size of α_d and γ_d is 6°. Under terrain shading, SORAM with various step sizes produces the modelled data, and SSF gives the measured data. In this case, the maximum step size of α_d and γ_d is 2°. These experiments were done with 1° increment, and start from 1° for the step sizes of α_d and γ_d due to computer

Table 5.3: Output performance of SORAM and Perez et al. (1990a) vs observed data from the Sheffield Solar Farm. The unit of Mean Global Irradiance, MBE and RMSE is KJm^{-2}h^{-1}. The minus sign in MBE of SORAM means the output from SORAM underestimates that from the Sheffield Solar Farm measured global radiation data.

Surface	Mean Global	SORAM		Perez et al. (1990a) model	
Orientation	Irradiance	MBE	RMSE	MBE	RMSE
45° SE	912.1	45.8	177.2	72.6	196.5
45° SW	794.0	-13.2	121.5	9.6	103.5
Percent error		3.3%	17.4%	4.6%	17.3%

limitation and time.

In Table 5.2, SORAM outputs the modelled data, and the data from the Perez et al. (1990a) model is treated as the measured data. The performance is evaluated using the ratio of sloping diffuse radiation to horizontal diffuse radiation: this step is to check if the improved diffuse model in SORAM agrees with the Perez et al. (1990a) model. This table shows a $-3.6 \times 10^{-3}\%$ underestimation of SORAM against the Perez et al. (1990a) model, and the RMSE is $3.4 \times 10^{-2}\%$. In order to evaluate how consistent SORAM is with the Perez et al. (1990a) model, the step size of α_d and γ_d of $1°$ is used. These results indicate that the formulae deduced in Section 5.4 are consistent with the Perez et al. (1990a) model.

Similarly, Table 5.3 shows the comparison between SORAM and the observed SSF data, and, between the Perez et al. (1990a) model and the observed SSF data. The performance is evaluated using the global irradiance since this step is to validate SORAM. The "SORAM" shown in Table 5.3 depicts that SORAM ran under real shading conditions around the *origin*. In this case, SORAM gives the modelled data, and SSF gives the measured data. The shading is mainly caused by two parts of Hicks building with absolute heights (higher than the *origin*) of 21.9 m and 4.3 m respectively, as shown in Figure 5.6. Note that the Perez et al. (1990a) model is not able to integrate the shading effect from the surroundings. Therefore the diffuse radiation produced by SORAM is smaller than the Perez et al. (1990a) model due to shading (Table 5.3). Considering computation time, the step size of α_d and γ_d is $2°$ for this table.

Furthermore, SSF's horizontal global radiation has been measured under the same shading conditions (the green triangle in Fig 5.6 shows the position of the SSF's pyranometers), and used to predict the tilted direct and diffuse radiation for the tilt-orientated PV cell. However, in order to calculate solar radiation on a shaded sloping PV cell, SORAM input should be unshaded horizontal global radiation, which is not available in Sheffield. Therefore, we expected that SORAM modelled output would underestimate the solar energy. The evaluation, between the $45°$ SW pyranometer

from SSF and SORAM modelled output under the same configuration and shadow effects as shown in SORAM in Table 5.3, meets the expectation whose MBE is -13.2 KJm^{-2}h^{-1}; however, for the 45° SE case, it does not. There are at least three reasons for these errors, regardless of the overestimation or underestimation. The first reason is the complexity of the 45° SE surroundings, where only the Hicks building (main shadow) is taken into account, whereas several buildings of unknown heights that could cast shadows on the pyranometer are not included in SORAM. Secondly, the modelled solar radiation is sensitive to the positions of the pyranometer (the triangle in Figures 5.6b and 5.6c) and the buildings, while the real-life map in SORAM (Figures 5.6b and 5.6c) is just an approximation constructed from Google Map: thus this approximation may produce errors. Thirdly, it is believed that the largest errors are introduced by the embedded Perez et al. (1990a) model, which treats the solar radiation contribution within each sky zone as uniform, and from errors in the solar-radiation measurements.

The absolute averaged MBE of SORAM with shading against the observed data is 3.3% while RMSE is 17.4%: MBE (RMSE) is smaller than (similar to) the MBE (RMSE) of 4.6% (17.3%) obtained using the Perez et al. (1990a) model against measured data. Overall, SORAM shows a better and more accurate performance than the Perez et al. (1990a) model.

5.6   Conclusion

In this chapter, we propose a numerical model (SORAM) for evaluating the direct and diffuse solar radiation on a sloping PV cell in an urban environment. We believe this is a key enabler technology with great potential for the mass deployment of solar PV cells in current and future sustainable cities.

The chapter makes three key contributions. First, the established Perez et al. (1990a) model is combined with a ray-tracing algorithm to improve the accuracy of anisotropic diffuse radiation modelling, taking into account the angle of incidence of

each solar ray. Second, dynamic 3D shading from urban obstacles (buildings/trees) is integrated into the model. Third, the model is validated using empirical measurement.

More specifically, the chapter utilizes the Reindl et al. (1990) to convert global horizontal radiation to direct and diffuse radiation. The direct radiation on a PV cell of a given slope and azimuth is determined following Duffie and Beckman (1991) and Muneer (2004), together with a ray-tracing algorithm. The Perez et al. (1990a) model is adapted with a ray-tracing algorithm, in order to transform diffuse radiation from a patch in the sky to a specific ray. The combined algorithm is then used to compute the shading effect from the urban terrain buildings. Finally, we aggregate the direct and diffuse radiation received.

SORAM without shading is validated against the (Perez et al., 1990a) model. A $-3.6 \times 10^{-3}\%$ underestimation show that under conditions of no shading SORAM works as well as the Perez et al. (1990a) model. SORAM with shading is evaluated against the observed SSF solar radiation data. The results show a 3.3% MBE and a 17.4% RMSE, while these values are respectively 4.6% and 17.3% when the outputs from the Perez et al. (1990a) model are compared with SSF data. Therefore, SORAM overall performs better than the Perez et al. (1990a) model.

The proposed model has been applied to a sample area in order to demonstrate its capabilities. Error analysis shows that SORAM can be effectively used in many applications including solar energy (PV and thermal) installations and environmentally friendly urban design. A further development of SORAM will focus on flexibility of shapes of obstacles and integrating reflected radiation by different materials such as glass and trees.

For queries about the SORAM computer code, please contact the corresponding author. For queries about the experimental data used here, please consult Dr Alastair Buckley (alastair.buckley@sheffield.ac.uk) from the Sheffield Solar Farm (www.sheffieldsolarfarm.group.shef.ac.uk) who is the PI of SSF.

5.A Appendix: coordinates of the triangle and the *origin* point

A triangle is treated as a PV cell with selected orientation and slope angles. The coordinates of the three corners and centroid point of the triangle is computed in this Appendix.

Assume the triangle is a equilateral triangle as shown in Figure A.1, input values are the coordinates of the corner V_0, i.e. x_0, y_0, z_0.
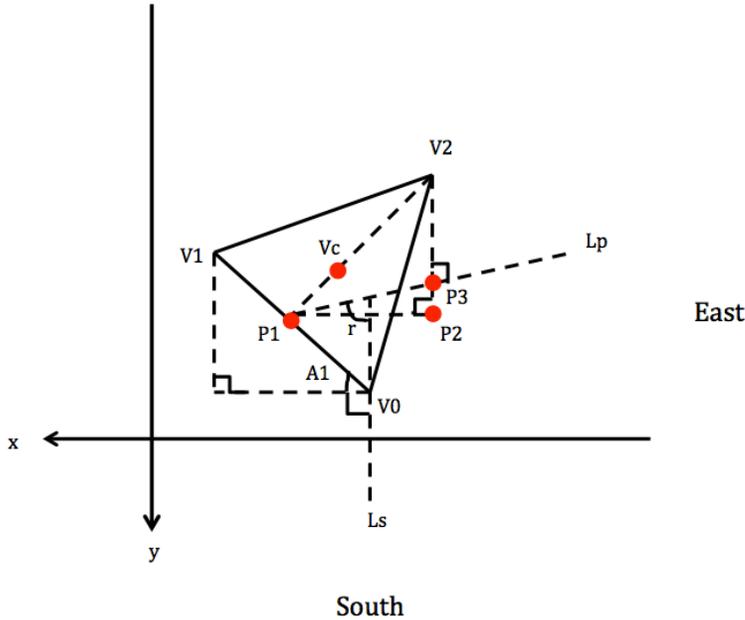
Figure A.1 Coordinates of the triangle regarded as a PV cell used to detect shading conditions arising from the PV cell itself.

$$
\begin{cases}
V_0 = [x_0, y_0, z_0], \\
V_1 = [x_1, y_1, z_0], \\
V_2 = [x_2, y_2, z_2], \\
d = 0.1.
\end{cases}
\tag{A.1}
$$

Here, d is the length of a side of the triangle. The amount of d does not affect the

received solar radiation, which has been proved by the 3D SORAM simulator.

5.A.1 (i) $-90° \leqslant \gamma \leqslant 90°$

If the azimuth angle of a PV cell γ is between $-90° \leqslant \gamma \leqslant 90°$, the angle between Lp and Ls is γ, thus the angle $A1 = \gamma$, which gives:

$$\begin{cases} x_1 = x_0 + d\cos(\gamma), \\ y_1 = y_0 - d\sin(\gamma). \end{cases} \quad (A.2)$$

The coordinates of P1 are:

$$\begin{cases} P1_x = \frac{x_1-x_0}{2} + x_0, \\ P1_y = \frac{y_1-y_0}{2} + y_0, \\ P1_z = z_0. \end{cases} \quad (A.3)$$

and the distance between P1 and V_2 is $\frac{\sqrt{3}d}{2}$, thus the distance between P1 and P3 is $\frac{\sqrt{3}d}{2}\cos(s)$. The acute angle between the line Lp the line between P1 and P2 is also γ. Therefore, the distance between P1 and P2 is $\frac{\sqrt{3}d}{2}\cos(s)\sin(\gamma)$, and the distance between P2 and P3 is $\frac{\sqrt{3}d}{2}\cos(s)\cos(\gamma)$. So the coordinates of V_2 are:

$$\begin{cases} x_2 = P1_x - \frac{\sqrt{3}d}{2}\cos(s)\sin(\gamma), \\ y_2 = P1_y - \frac{\sqrt{3}d}{2}\cos(s)\cos(\gamma), \\ z_2 = z_0 + \frac{\sqrt{3}d}{2}\sin(s). \end{cases} \quad (A.4)$$

Therefore, the coordinates of the *origin* V_c (the point slightly higher than the centroid of the triangle) are:

$$\begin{cases} Vc_x = \frac{2}{3}(P1_x - x_2) + x_2, \\ Vc_y = \frac{1}{3}(y_2 - P1_y) + P1_y, \\ Vc_z = \frac{z_2 - z_0}{3} + z_0 + \frac{d}{1000}. \end{cases} \tag{A.5}$$

The algorithm will evaluate the collected diffuse portion for any selected spot within SORAM domain. The size of the triangle (i.e. d) will not affect the estimated output of solar radiation. The experiment shows that the *origin*, which should be higher than centroid of the triangle, and it is fixed at 0.001 times d. Similarly, there are two sets of coordinates for the triangle and the *origin* when $-180° \leqslant \gamma < -90°$ and $90° < \gamma \leqslant 180°$.

5.A.2   (ii) $90° < \gamma \leqslant 180°$

The angle between Lp and Ls is azimuth angle of this PV cell γ, thus the angle $A1 = 180° - \gamma$, which yields:

$$\begin{cases} x_1 = x_0 - d\cos(180° - \gamma), \\ y_1 = y_0 - d\sin(180° - \gamma). \end{cases} \tag{A.6}$$

The coordinates of P1 are:

$$\begin{cases} P1_x = \frac{x_0 - x_1}{2} + x_1, \\ P1_y = \frac{y_0 - y_1}{2} + y_1, \\ P1_z = z_0. \end{cases} \tag{A.7}$$

and the distance between P1 and V_2 is $(\sqrt{3}d)/2$, thus the distance between P1 and P3 is $((\sqrt{3}d)/2)\cos s$. The obtuse angle between the line Lp and the line between P2 and P3 is also γ. Therefore, the distance between P2 and P3 is $(((\sqrt{3}d)/2)\cos s)\cos 180° - \gamma$,

and the distance between P1 and P2 is $(((\sqrt{3}d)/2)\cos s)\sin 180° - \gamma$.

So the coordinates of V_2 are:

$$\begin{cases} x_2 = (x_0 - x_1)/2 + x_1 - (((\sqrt{3}d)/2)\cos s)\sin 180° - \gamma, \\ y_2 = (y_0 - y_1)/2 + y_1 + (((\sqrt{3}d)/2)\cos s)\cos 180° - \gamma, \\ z_2 = z_0 + ((\sqrt{3}d)/2)\sin s. \end{cases} \qquad (A.8)$$

Therefore, the coordinates of centroid of the triangle V_c is

$$\begin{cases} Vc_x = \frac{2}{3}(P1_x - x_2) + x_2, \\ Vc_y = \frac{1}{3}(y_2 - P1_y) + P1_y, \\ Vc_z = \frac{z_2 - z_0}{3} + z_0 + \frac{d}{1000}. \end{cases} \qquad (A.9)$$

5.A.3   (iii) $-180° \leqslant \gamma < -90°$

The angle between Lp and Ls is azimuth angle of this PV cell γ, thus the angle $A1 = 180° - \gamma$, which yields:

$$\begin{cases} x_1 = x_0 - d\cos(180° - \gamma), \\ y_1 = y_0 - d\sin(180° - \gamma). \end{cases} \qquad (A.10)$$

The coordinates of P1 are:

$$\begin{cases} P1_x = \frac{x_0 - x_1}{2} + x_1, \\ P1_y = \frac{y_1 - y_0}{2} + y_0, \\ P1_z = z_0. \end{cases} \qquad (A.11)$$

and the distance between P1 and V_2 is $(\sqrt{3}d)/2$, thus the distance between P1 and P3 is $((\sqrt{3}d)/2)\cos s$. The obtuse angle between the line Lp and the line between P1 and P3 is also γ. Therefore, the distance between P2 and P3 is $(((\sqrt{3}d)/2)\cos s)\cos(180° - \gamma)$,

95

and the distance between P1 and P2 is $(((\sqrt{3}d)/2)\cos s)\sin(180° - \gamma)$.

So the coordinates of V_2 are:

$$\begin{cases} x_2 = (x_0 - x_1)/2 + x_1 + (((\sqrt{3}d)/2)\cos s)\sin 180° - \gamma, \\ y_2 = (y_1 - y_0)/2 + y_0 + (((\sqrt{3}d)/2)\cos s)\cos 180° - \gamma, \\ z_2 = z_0 + ((\sqrt{3}d)/2)\sin s. \end{cases} \qquad \text{(A.12)}$$

Therefore, the coordinates of centroid of the triangle V_c is

$$\begin{cases} Vc_x = \frac{1}{3}(x_2 - P1_x) + P1_x, \\ Vc_y = \frac{1}{3}(y_2 - P1_y) + P1_y, \\ Vc_z = \frac{z_2 - z_0}{3} + z_0 + \frac{d}{1000}. \end{cases} \qquad \text{(A.13)}$$

Chapter 6

Development of smart phone application to estimate the shading effect of obstacles

Abstract

The aim of this chapter is to present a mobile application (app) used to predict and optimise the direct and diffuse solar radiation collected in an urban area, taking into account terrain shading. The key contribution of this work is to demonstrate a new image-processing-based algorithm for evaluating terrain shading around a point of interest by a smart phone. By input unshaded global horizontal radiation (hourly), we validate our modelling results using empirical sloping solar radiation data observed at a real urban area, and also validate our results against the output from SORAM (Erdélyi et al., 2014) under the same shading conditions. We use iPhone 4 as an example and explain the programming of the app in detail in the Section 6.A.

This work has been submitted to the journal *Renewable Energy* (Wang et al., 2014b). The authors are Yimin Wang, Róbert Erdélyi, Edward Hanna and Giuseppe Colantuono.

Keywords: panoramic picture; smart phone; solar radiation model; terrain shading.

6.1 Introduction

Global solar radiation at the Earth's surface comprises direct, diffuse and reflected components. In most cases, reflected radiation is negligible (HEMI, 2000) and is therefore ignored in this work. Although horizontal global radiation data are commonly obtainable, horizontal direct and diffuse components are rarely measured due to high cost. Horizontal direct and diffuse radiation data are necessary to predict global radiation on a given tilt-oriented PV module. Solar radiation received by a surface located in an urban area is crucial to thermal and photovoltaic (PV) solar energy installations. However, most existing solar radiation models do not take into account the effects resulting from shading due to complex urban obstacles. Besides the effective solar irradiance, terrain shading also has an important influence on the practical efficiency of PV module (Melo et al., 2013).

Several algorithms have been established for analysing shading conditions at a location. The method from Quaschning and Hanitsch (1998) can estimate the surroundings of a PV module by describing the shading profile with polygons. These polygons are then quantified in spherical coordinates. However, converting real life view to polygons results in errors; describing each vertex of complex polygons is difficult. Another method developed by Orioli and Gangi (2012) allows the estimation of shading effect by comparing the photographed solar discs and the calculated Sun's positions. However, besides a camera, this method also requires a compass and a clinometer to produce the input data; and angle of incidence of diffuse rays are not able to be considered. Moreover, compared with the above methods, our work involves a function to weaken the edges of scattered clouds, which will be introduced in later sessions.

In Erdélyi et al. (2014), we have presented the three-dimensional (3D) SOlar RAdiation Model (SORAM). The Reindl et al. (1990) model, which is embedded

into SORAM, splits observed hourly horizontal global radiation into its direct and diffuse components. SORAM then corrects these derived horizontal direct and diffuse components for the tilted PV cell taking into account geometry, i.e. solar altitude, solar azimuth, azimuth and elevation of the PV cell as shown in Figure 5.2, as well as terrain shading using a ray-tracing algorithm. The shading casted by buildings, trees and other obstacles, which are represented by voxels, are incorporated into a 3D environment. Solar altitude varies between $[0°, 90°]$, and the solar azimuth angle ranges between $-180°$ and $180°$ with $0°$ being due south, where east is negative and west is positive. All the parameters defining the position of the Sun in the sky are considered on a daily or hourly basis. By aggregating the direct and diffuse rays from all the points in the sky that are not blocked by obstacles based on the adjusted Perez et al. (1990a) model, SORAM can be used to accurately compute the global radiation collected by a sloping PV array.

In this chapter, we propose a Shading Detection Algorithm (SDA) based on image processing for evaluating shading conditions of a PV module. We, then, combine SDA with SORAM to develop an app to be used on a smart phone. All the algorithms that underpin this app are analogous to the ones used in SORAM, except for the way of computing terrain shading. Instead of voxels representing obstacles in SORAM, SDA analyses the available panoramic picture taken by the smart phone, which is the surrounding view of a PV module. Under this way, the shading profile is described by spherical coordinates, i.e. elevation and azimuth which is the same as a solar ray's (direct or diffuse) azimuth. By comparing hourly solar altitude with the elevation of the shading at the same azimuth as the solar ray's, SDA evaluates if a solar ray (direct or diffuse) can reach the PV cell. SDA requires less data input compared with the shading analysis algorithm in SORAM since the knowledge of all dimensions of obstacles is not necessary. The time step size depends on the time resolution of observations. Hourly temporal resolution is sufficient for most applications (Hofierka and Zlocha, 2012), and is thus adopted in this work.

6.2 Structure of this work

6.2.1 Description of functions

Figure 6.1 displays the four tabs in the app developed here.

1. The first tab "Map" is used to determine the latitude of the point of interest;

2. The desired PV modules can be chosen from the second tab "Panels", which lists the available technologies. The efficiency of the chosen module is later used for computation;

3. The third tab "Mounting" allows users to either lay their iPhone on a mounted PV module to read its slope and azimuth (using the segment button "Sensor"), or to input the desired slope and azimuth for PV modules using the segment button "Type-in" or "Slider";

4. The fourth tab "Skyview" calls the function "Camera" to make a panoramic picture of the surroundings of the point of interest, and to derive the azimuths and elevations of the surroundings. Then, the function "Evaluate" calculates the annual power output, which depends on latitude, PV module type, slope and azimuth of the PV modules, as well as on terrain shading. Finally, the function "Optimise" is used to determine the optimal slope and azimuth for the PV modules.

6.2.2 Project Outline

A list of the parameters used in the app can be found in Table 6.1. Figure 6.2 outlines the overall structure of the app. Section 6.3 describes the algorithms that estimate tilted direct and diffuse radiation from their horizontal counterparts, taking into account terrain shading. Section 6.3.3 explains how the surrounding of a PV module is captured to make up a panoramic picture, and how this picture is used to evaluate

Figure 6.1: The four tabs of the iPhone 4 app.

terrain shading. The algorithms which evaluate terrain shading are summarized in Figure 6.9. In Section 6.4, we validate our model by comparing its output with empirical solar radiation data, and also compare our results with the output from SORAM (Erdélyi et al., 2014) under the same surroundings.

6.3 The solar radiation model

6.3.1 Direct radiation

Without terrain shading, the energy contribution of a direct ray hitting a PV module can be estimated by:

$$B_s = B_h \frac{a_0}{a_1}, \tag{6.1}$$

where,

$$
\begin{aligned}
a_0 &= \max\left(0, \cos\left(\theta\right)\right), \\
a_1 &= \max\left(\cos\left(85°\right). \cos\left(\frac{\pi}{2} - \alpha_s\right)\right).
\end{aligned}
$$

and, B_s and B_h are the hourly direct radiation on a sloping and horizontal PV module, respectively, α_s is the solar altitude. For more details of these variables, see Muneer
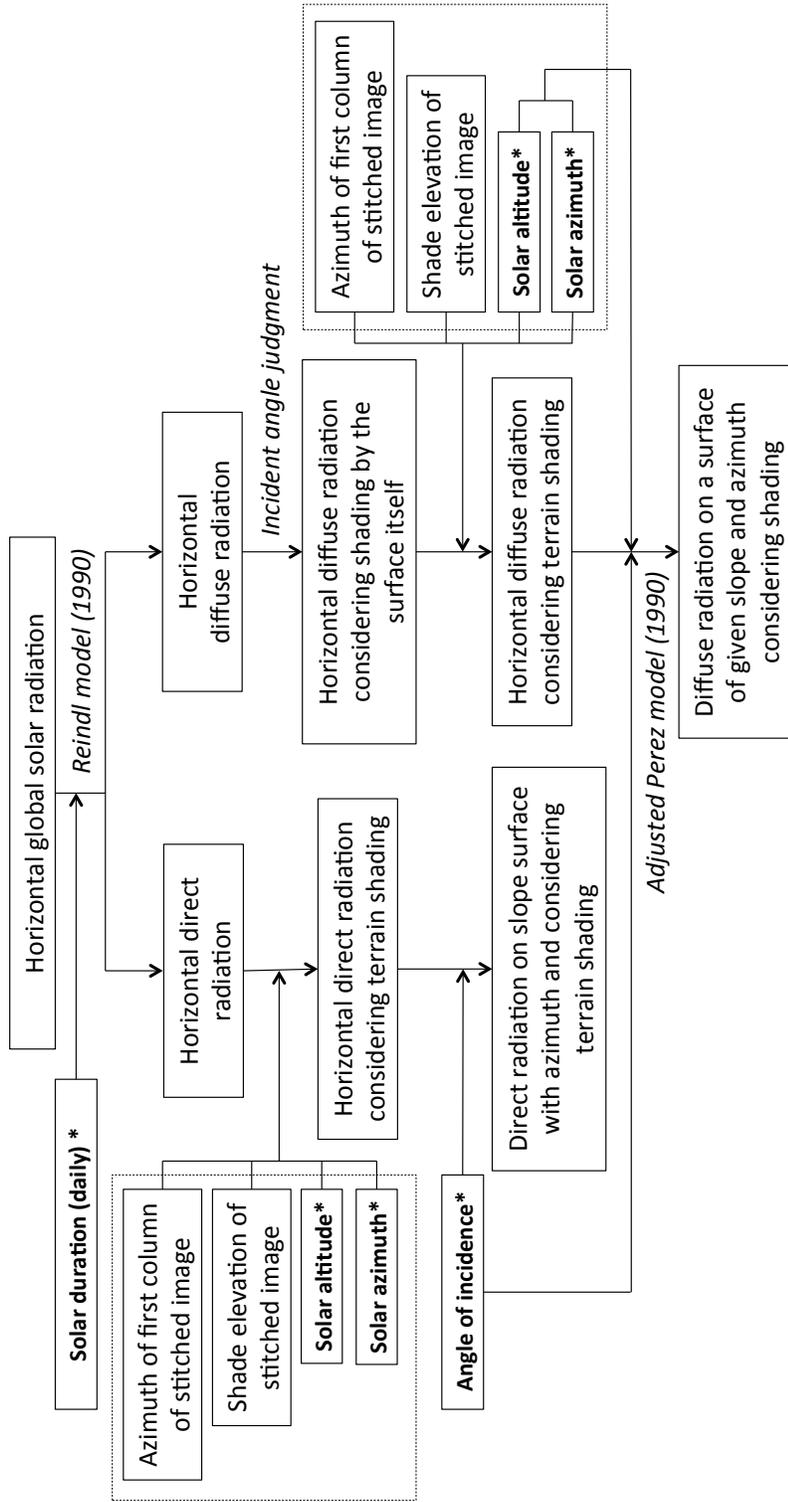
Figure 6.2: Flowchart of the mobile app. Solar altitude, solar azimuth, solar duration and angle of incidence are derived from the process summarized in Figure 5.2. The parameters marked as "daily" are daily values, otherwise parameter values are hourly.

Table 6.1: Nomenclature used in this study

B_s	Sloping direct radiation
B_h	Horizontal direct radiation
θ	Angle of incidence from direct radiation
α_s	Solar altitude
1	Diffuse radiation contribution coefficient (main)
F_1	Diffuse radiation contribution coefficient (circum-solar)
F_2	Diffuse radiation contribution coefficient (horizon)
θ_d	Angle of incidence from diffuse radiation
α_d	Diffuse-ray altitude
γ_d	Diffuse-ray azimuth
γ	Surface azimuth angle
γ_{1N}	Azimuth of center of first image of panoramic picture relative to North
n_{tot}	Total number of columns of panoramic picture
γ_{c1N}	Azimuth of first column of first image of panoramic picture relative to North
γ_{c1S}	Azimuth of first column of first image of panoramic picture relative to South
γ_s	Solar azimuth
n	Day number of a year
i	Number of hours between sunrise and sunset
n_{com}	Number of column for current comparison
τ	Angle of each column of image
n_{col}	Total number of columns of an image
n_{row}	Total number of rows for a column of an image
α	Elevation of shade
r_{ele}	Number of the highest row that has a white section in each column
Ω	Solar duration

(2004).

6.3.2 Diffuse radiation

It is found that there are two main zones resulting from the anisotropic nature of diffuse radiation in the Earth's atmosphere (Kano, 1964):

1. Circumsolar brightening resulting from forward scattering by aerosols;

2. Horizon brightening mostly caused by multiple Rayleigh scattering and retro-scattering in a clear atmosphere.

The Perez et al. (1990a) model assumes that all circumsolar energy emanates from a point centred on the Sun's position, and represents the horizon zone with a unidimensional arc of a great circle at the base of the atmosphere. By adjusting the Perez et al. (1990a) model, Erdélyi et al. (2014) found that for each diffuse ray in the main, circumsolar and horizon zones, the energy contributions are, respectively

$$\frac{1 - F_1}{\int_{-\pi}^{\pi} \int_0^{\frac{\pi}{2}} \sin(\alpha_d) \, d\alpha_d d\gamma_d} \cos(\theta_d), \tag{6.2}$$

$$F_1 \frac{a_0}{a_1}, \tag{6.3}$$

and

$$\frac{F_2}{\int_{\gamma-\frac{\pi}{2}}^{\gamma+\frac{\pi}{2}} \cos(\gamma_d - \gamma) \, d\gamma_d} \cos(\theta_d). \tag{6.4}$$

6.3.3 Shading conditions - SDA

The steps needed to acquire the panoramic picture of the surroundings of the PV module are:

1. Capturing a series of images around a PV module (Figure 6.3 (a));

2. Stitching the captured images in step 1 into a panoramic picture (Figure 6.3 (b));

3. Converting the panoramic colored picture into black and white by an edge-detection algorithm (Figure 6.3 (c));

4. Determining the edges between the sky and other discerning objects in the panoramic picture;

5. Computing the elevations of the shadow-casting objects for each column in the panoramic picture, by applying the vertical angle of view of the smart phone.
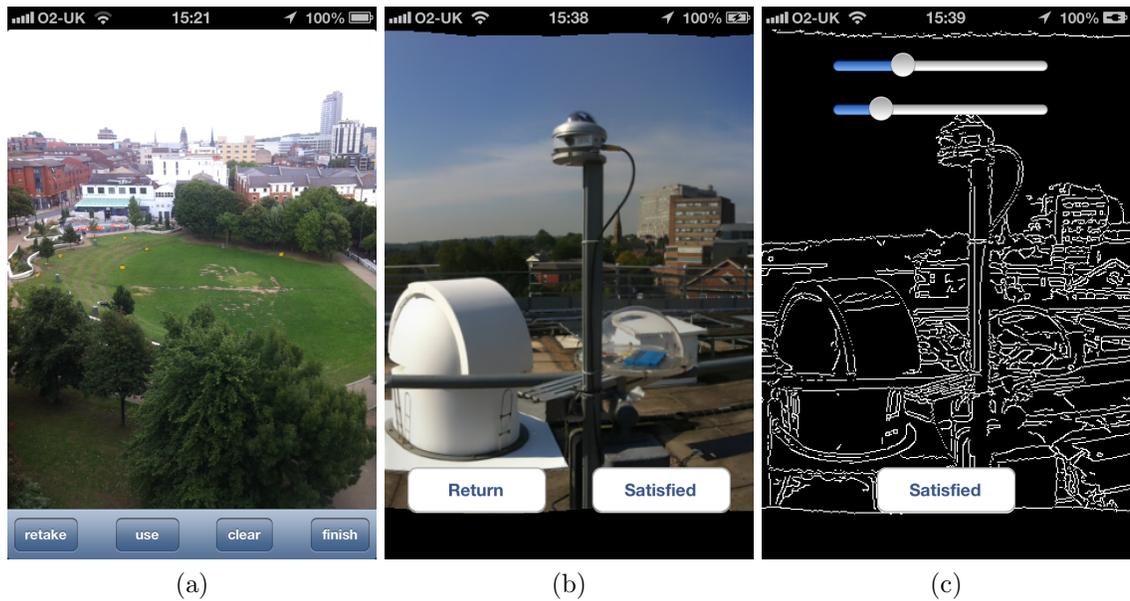
Figure 6.3: The three steps needed to acquire a panoramic picture of the PV module's surroundings: (a) images are taken and saved to the app's local document storage; (b) images are stitched into a panoramic picture; (c) low and high thresholds are adjusted to obtain a satisfactory black and white panoramic picture.

When a smart phone is held vertically, an image is captured automatically and immediately shown in the display of the smart phone. Objects higher than the central horizontal line of the image can obstruct sunshine. If the image taken is satisfactory:

1. it is saved to the app's local document storage on the smart phone, and the semi-transparent right half of it is overlaid on the left half of the display so the user can overlap it with the new view seeing in the display and take the next image;

2. it also means the azimuth of the phone (when the image was taken) is recorded. Only the azimuth of the first image making up the panoramic picture is sent to the solar radiation model for further processing (i.e. identification of the positions of the shadow-casting objects).

If the image taken is not satisfactory, it is discarded and another one is taken. This procedure is repeated until a sufficient number of images for determining the shading

from the surroundings of a PV module is taken. Finally, all these images are amalgamated as a panoramic picture, which is then saved to the app's local document.

The Open Source Computer Vision Library is a library of programming functions mainly aimed at real-time computer vision (OpenCV, 2013), which fulfills two tasks here:

1. Stitching together the images;

2. Converting the stitched full color picture into a black and white version by using the Canny edge detection (Canny, 1986), so that all edges are represented by white (i.e. grey level value greater than 200), while the background is black.

The fifteen sample images in Figure 6.4 are stitched into the panoramic picture shown in Fig 6.5. The panoramic picture is converted into greyscale on one hand for limiting the computational requirements (Figure 6.6); on the other hand, Laungrungthip et al. (2010) found that the blue color channel in a full color image can not only increase the contrast between the sky and non-sky regions of an image, but it also can decrease the contrast between scattered clouds and blue sky. Therefore, during the conversion from a full color image to the greyed one, increasing the weight of the blue color channel can reduce the likelihood that clouds are recognised as regions separate from the sky. The Canny edge detection algorithm (Canny, 1986) then determines the edges where the greyscale intensity of the picture changes the most, i.e. where gradients are stronger; the black and white version of the original picture is then produced (Figure 6.7). Low and high thresholds of the Canny edge detection function can be tuned to remove unnecessary edges like cloud boundaries, while retaining the edges of the shading objects, i.e. shading profile. For example, after some attempt, although using the same high thresholds, Figure 6.8 is taken under a low threshold value of 10; while Figure 6.7 uses a low threshold value of 120 to avoid cloud edges. About 20 images with various cloud types have been tested. After increasing the weight of the blue color channel when an image is converted into greyscale, together with using low and high thresholds function, the edges of clouds

106

can be erased. The elevation of shading profile at each column (the set of pixels having the same abscissa) of the panoramic picture is then used by the solar radiation model.
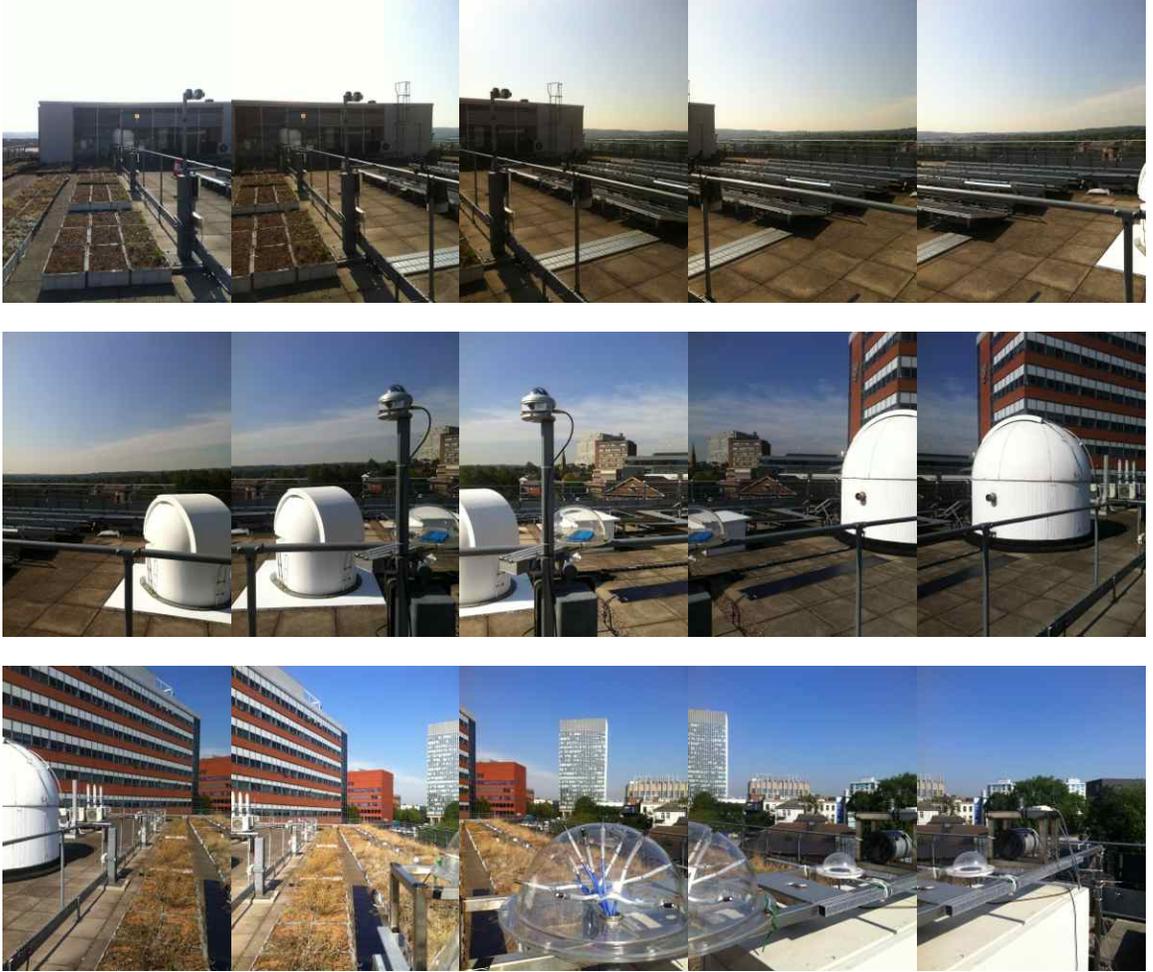
Figure 6.4: The fifteen images used to derive the panoramic picture around the pyranometer on top of Hicks Building at the University of Sheffield, UK.

In this work, we use iPhone 4 for testing the output from the app. Since the vertical angle of view of the iPhone 4 is 61°, the higher half of the panoramic picture occupies 30.5°. Therefore, the elevation of shading profile for each column in the panoramic picture is (Figure 6.9)

$$\alpha = \frac{r_{ele} - n_{row}/2}{n_{row}} \times 30.5°. \tag{6.5}$$

Figure 6.5: Panoramic picture obtained by merging together the images shown in Figure 6.4
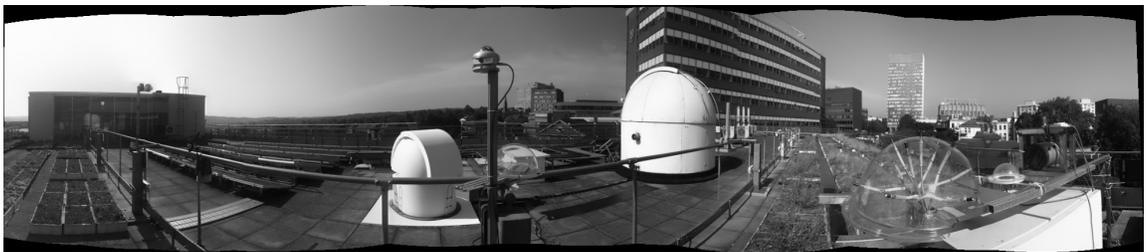
Figure 6.6: Greyscale panoramic picture looking around the pyranometer on top of Hicks Building at the University of Sheffield, UK.
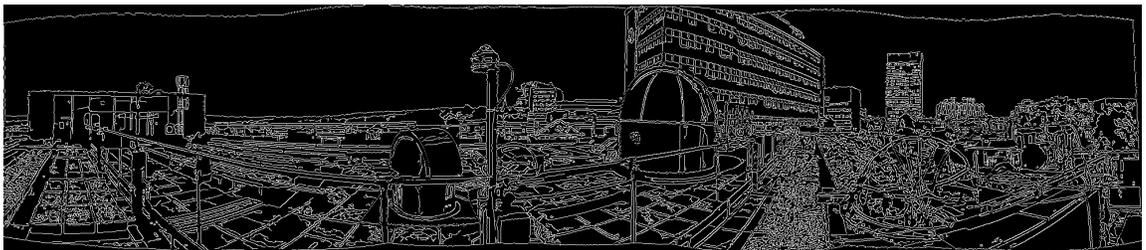
Figure 6.7: Black and white panoramic picture without clouds.
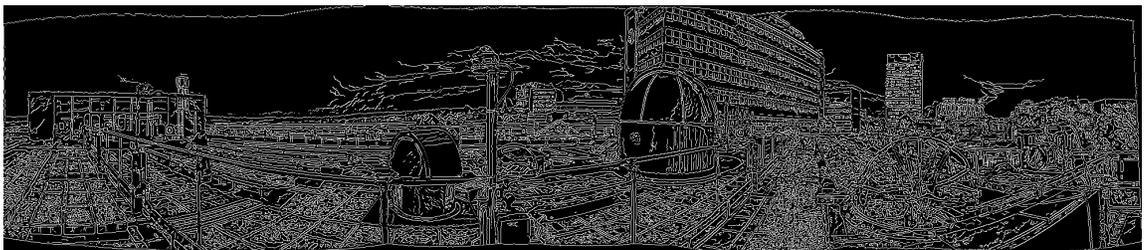
Figure 6.8: Black and white panoramic picture with clouds.

We, then, calculate the azimuth of the first column of the panoramic picture for identifying the position of the panoramic picture within the surrounding view. Since the horizontal angle of view of the iPhone 4 is 47.5°, the angle of each column of the panoramic picture is $\tau = 47.5°/n_{col}$. As shown in Figure 6.9, if the azimuth of the first image (i.e. the central column of the first image) of the panoramic picture relative to North γ_{1N} is greater than half of the horizontal angle of view, the azimuth of the first column of the panoramic picture relative to North is

$$\gamma_{c1N} = \gamma_{1N} - \frac{47.5°}{2}, \tag{6.6}$$

otherwise,

$$\gamma_{c1N} = 360° - (\frac{47.5°}{2} - \gamma_{1N}). \tag{6.7}$$

Therefore, the azimuth of the first column of the panoramic picture relative to South is

$$\gamma_{c1S} = \gamma_{c1N} - 180°. \tag{6.8}$$

If the hourly solar azimuth (γ_s) is greater than or equal to γ_{c1S}, the number of the columns in the panoramic picture having the same azimuth as the solar ray's are:

$$n_{com} = (\gamma_s[n][i] - \gamma_{c1S})/\tau, \tag{6.9}$$

otherwise,

$$n_{com} = (360° + \gamma_s[n][i] - \gamma_{c1S})/\tau. \tag{6.10}$$

where n and i in square brackets are the number of days in a year, and number of hours between sunrise and sunset, respectively.

If n_{com} is smaller than or equal to the total number of columns of the panoramic picture, meaning n_{com} is not beyond the panoramic picture, the comparison of α_s with the elevation angle of shading for that column allows to evaluate if a solar ray can reach the PV module. This procedure is repeated for each direct and diffuse ray.
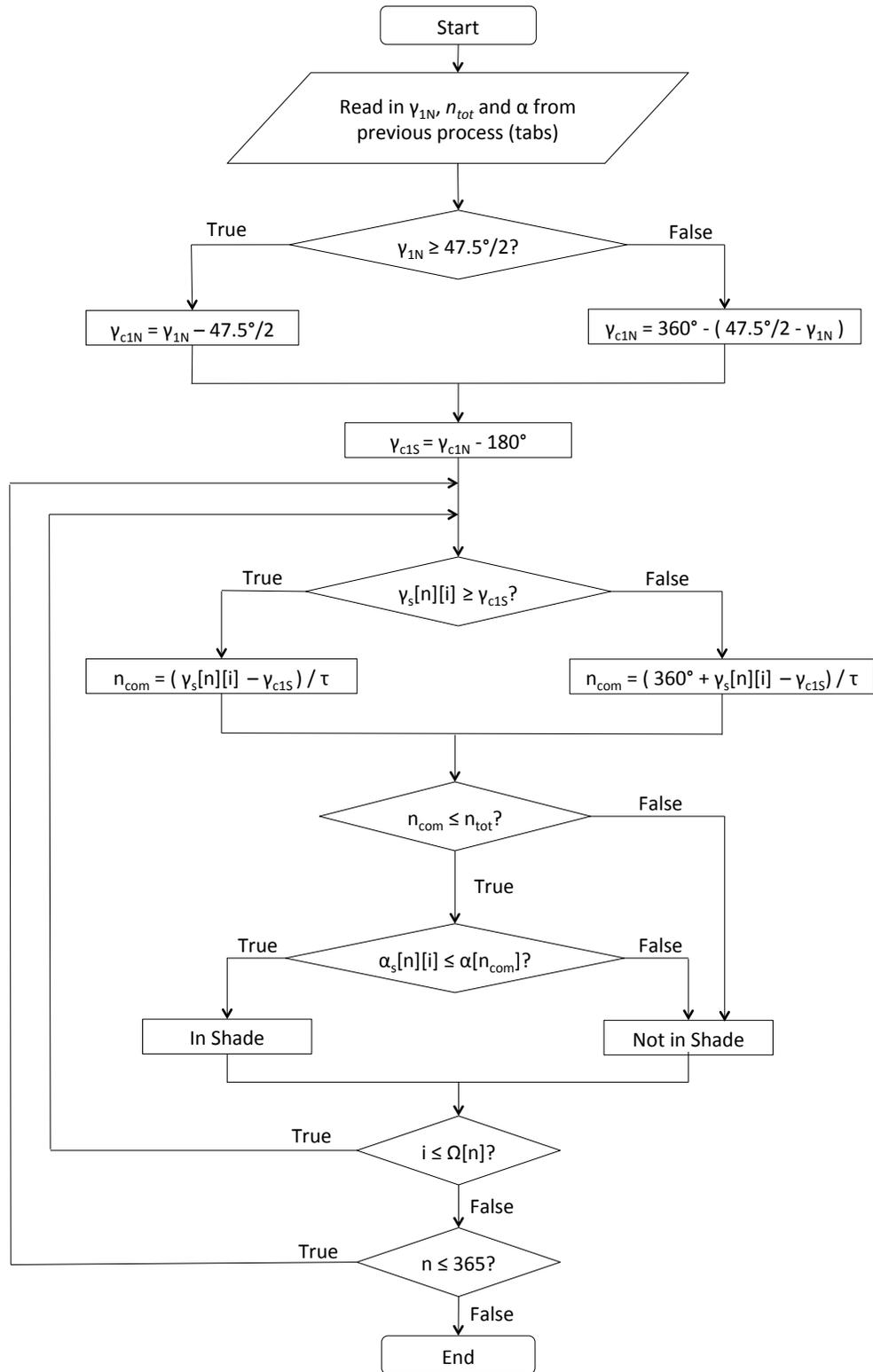
Figure 6.9: Flowchart showing the calculation of terrain shading embedded in the mobile app.

Finally, when all the direct and diffuse rays are aggregated, the diffuse contribution coefficient is multiplied by the hourly observed horizontal diffuse radiation to obtain the tilted diffuse radiation. This is then added to the direct radiation at the same timestep to obtain the tilted global radiation. The tilted global radiation is then multiplied by the efficiency of the PV module from the second tab to obtain the overall power output in kWh/m^2.

Repeating the above process for a range of slope ($[0, 90°]$) and azimuth ($[-180°, 180°]$) for an entire year, and finding the maximum power output, gives the optimal slope and azimuth. The ratio between the power output computed for a mounted PV module to that for the optimal slope/azimuth is the efficiency for the chosen way of mounting.

6.4   Evaluation of the app's performance

The Sheffield Solar Farm (The Sheffield Solar Farm, 2013) is part of Project Sunshine operating at the University of Sheffield, UK, and allows real-world testing of photovoltaic technology. A horizontal pyranometer and two different directions oriented pyranometers at a 12.7° tilt, 45° southeast facing and 45° southwest facing are mounted on top of the Hicks Building at the University of Sheffield. Nine months of hourly global radiation data were collected by these three pyranometers. Figure 6.5 show the landscape around those pyranometers.

The performance of the app is shown in Tables 6.2 and 6.3. The evaluation includes the mean bias error (MBE), given by

$$\text{MBE} = \frac{\sum_n(\text{model}_i - \text{observed}_i)}{n}, \tag{6.11}$$

where n is the number of data points and i denotes a given event, and the root mean

Table 6.2: Performance of the app vs the Perez et al. (1990a) model. The output is the ratio of diffuse radiation on a sloping PV cell to that on a horizontal module. The minus sign in MBE means the output from the app underestimates that from the Perez et al. (1990a) model.

Orientation	Mean	MBE	RMSE
45°SE	1.1	-2.8 $\times 10^{-4}$	4.7 $\times 10^{-4}$
45°SW	1.0	-3.1 $\times 10^{-4}$	7.4 $\times 10^{-4}$
Percentage error		-0.03 %	0.4 %

square error (RMSE),

$$\text{RMSE} = \left\{ \frac{\sum_n (\text{model}_i - \text{observed}_i)^2}{n} \right\}^{0.5}. \tag{6.12}$$

Table 6.2 compares the tilted diffuse radiation calculated by the original and adjusted Perez et al. (1990a) model versions without considering terrain shading. In this evaluation, the adjusted Perez et al. (1990a) returns the modelled data, while the output of the original Perez et al. (1990a) model is treated as the observed data. There is a 0.03% underestimation of the adjusted Perez et al. (1990a) model from the app against the original Perez et al. (1990a) model, and the RMSE is 0.4%. These results indicate that the adjusted Perez et al. (1990a) model is consistent with the original one.

Similarly, Table 6.3 shows the global radiation comparisons between the app and the SSF observations, and, between the Perez et al. (1990a) model and SSF observations. In this evaluation, the app takes into account the real terrain shading around the SSF pyranometers. Note that the Perez et al. (1990a) model is not capable of integrating terrain shading. Therefore, the diffuse radiation estimated by the app is lower than the Perez et al. (1990a) model output due to shading.

Moreover, the SSF global horizontal pyranometer is subject to the same shading conditions as the sloping pyranometers shown in Figure 6.5, and was implemented to predict the tilted direct and diffuse radiation for a tilt-orientated PV module. However, in order to estimate global radiation on a shaded tilted PV module, the input

Table 6.3: Output of the app and Perez et al. (1990a) vs the observed data from the Sheffield Solar Farm. The unit of Mean Global Irradiance, MBE and RMSE is KJm^{-2}h^{-1}. The minus sign in the app's MBE means its output underestimates the Sheffield Solar Farm's observed global radiation.

Surface Orientation	Mean Global Irradiance	app		Perez et al. (1990a) model	
		MBE	RMSE	MBE	RMSE
45° SE	912.1	52.5	171.8	72.6	196.5
45° SW	794.0	-7.6	107.1	9.6	103.5
Percentage error		3.4%	16.2%	4.6%	17.3%

of the app should be unshaded horizontal global radiation, which is not obtainable in Sheffield. Hence, we expect the app output would underestimate the solar power. As shown in Table 6.3, the comparison between the 45° SW-oriented SSF pyranometer and the app output meets the expectations, i.e. the MBE is -7.6 kWh/m^2. On the contrary, the 45° SE-oriented SSF pyranometer does not. It is believed that the largest error is introduced by the solar-radiation measurements. The Perez et al. (1990a) model embedded in the app can also be a source of error, because it treats the solar radiation distribution within each sky zone as uniform.

Under terrain shading conditions, the absolute average MBE and RMSE from the app against the SSF observations are 3.4% and 16.2%, respectively. These values are smaller than the MBE and RMSE of 4.6% and 17.3% of the Perez et al. (1990a) model against SSF measurements. Therefore, the app shows a better agreement with observed data than the Perez et al. (1990a) model. Finally, we compare the output from the app with that from SORAM (Erdélyi et al., 2014) for the same test environment, the difference is within 1%.

6.5 Conclusion

In this chapter, we demonstrate a smart phone app for evaluating the direct and diffuse solar radiation received on a sloping PV module in an urban environment. We suggest this is a practical technology for both PV module suppliers and their

customers for accurate evaluation of PV capability.

The chapter makes three key contributions. First, it develops a new Shading Detection Algorithm (SDA) based on image processing for evaluating how terrain shading affects PV modules. Second, the output of the app is validated using empirical measurements. Third, we use iPhone 4 as an example and explain the programming of the app in detail in the Section 6.A.

SORAM (Erdélyi et al., 2014) is embedded in the app for calculating the contribution of each direct/diffuse ray. For evaluating terrain shading, SDA requires overlapping images to be taken off the viewscape surrounding a PV module location, stitch them to a panoramic picture and convert the panoramic picture into black and white based on Canny (1986) edge detection. SDA, then, derives the elevation of the shadow-casting obstacles from each column of the panoramic picture. By comparing the elevation of shading obstacles with solar altitude at the same azimuth as the solar ray's, SDA can determine if a direct/diffuse ray can reach a PV module. Finally, the energy of direct and diffuse rays is aggregated.

The app is validated against the Perez et al. (1990a) model without shading. An underestimation as low as 0.03% shows that the app works as well as the Perez et al. (1990a) model. Taking into account real shading conditions, the app is validated against the empirical SSF solar radiation data. The resulting 3.4% MBE and 16.2% RMSE are lower than the 4.6% MBE and 17.3% RMSE obtained by comparing the Perez et al. (1990a) model with the SSF data. Overall, the app performs as well as SORAM and better than the Perez et al. (1990a) model.

The app requires the input of unshaded global horizontal radiation (hourly). Therefore, it needs either an instrumented site or an external model or database.

6.A Appendix: app software

The programming language Objective-C and the compiler Xcode are used to create the app assisted by OpenCV in processing images.

6.A.1 Tab: Map

The class "CLLocationManager" and protocol "CLLocationManagerDelegate" of the framework "CoreLocation" are set up when the app is started, or the view of the tab "Map" is loaded. CLLocationManager is used to configure the delivery of the most recent location (e.g. latitude and longitude) and heading events of a device, i.e. initiate (start/stop) location and heading updates. These location- and heading-related updates are delivered to CLLocationManagerDelegate, which defines the method used to receive location and heading updates. The method "desiredAccuracy" of CLLocationManager is specified to be the highest-level of accuracy "kCLLocationAccuracyBest" for the app. Once the app is activated, the method "startUpdatingLocation" of CLLocationManager is called to start updating the latitude and longitude of the current location for later use. By pressing the "location" button, the user's current coordinates are found, shown in the center of the map view, and the latitude is sent to the solar radiation model underpins the tab "Skyview" for further calculation.

The class "MKMapView" and protocol "MKMapViewDelegate" of the framework "MapKit" are, also, set up when the app is activated, or the view of the tab "Map" is loaded. They provide an embeddable map interface, which is used to display map information. The map in the app is initially centered on the coordinates of the user's current location. The segment buttons "Map", "Satellite" and "Hybrid" are used to change the type of map that displayed by the method "mapType" of the class MKMapView.

The class "UISearchBar" and the protocol "UISearchBarDelegate" belong to the framework "UIKit". The former perform a text field control for text-based searches; while the latter actually implements the searches. The method "searchBarSearch-

ButtonClicked" of UISearchBarDelegate is called when a user clicks the search bar, which tells the delegate (i.e. a pointer to an object with a set of methods the delegate-holder knows how to call) conforming to UISearchBarDelegate the search button was tapped. The user can type in an address and click the button "Search". The method "geocodeAddressString" of the class "CLGeocoder" of CoreLocation is used to convert the address to the coordinates. The data types "MKCoordinateSpan" of MapKit is used to define to what extent, the user's map is displayed centered from the chosen coordinates. By using the class "MKPointAnnotation" of MapKit, the map accesses the coordinates of the chosen address and places a pin there. The final effect of clicking on the "Search" button is to send the latitude of the chosen address to the solar radiation model embedded in the tab Skyview for further calculation.

6.A.2 Tab: Panels

A spinning-wheel with a set of currently available PV modules is shown through the class "UIPickerView". The user selects these modules by rotating the wheel so that the desired row of the module aligns with a selection indicator. The method "didSelectRow: inComponent:" of the class's corresponding protocol "UIPickerViewDelegate" is called by the picker view when a user selects a module. A module's image and description are shown at the left and above the picker, respectively. Once a module is chosen, its efficiency is sent to the solar radiation for further calculation.

6.A.3 Tab: Mounting

There are three segment buttons at the top of the tab "Angles": "Sensor", "Type-in" and "Slider". Sensor is used to detect the current azimuth and slope of the iPhone 4. However, in the two text fields under Type-in, a user can type the desired azimuth and slope for a PV module. Slider performs the same functions as Type-in but chooses angles by sliders. In Sensor and Type-in, when the buttons "Azimuth" and "Slope" are pressed, or when the sliders in Slider are modified, these values of angles are sent

to the solar radiation model for further calculation. The buttons "Reset" in these segments can be used to erase any record of angles.

Azimuth of a PV module

In the segment button Sensor, the method "didUpdateHeading" of CLLocationManagerDelegate is used to obtain true north, which is the direction of the geographic North Pole. The value 0° means the device points exactly at true north, 90° means it points east, 180° means it points south, and so on. Under the segment Sensor: an iPhone 4 can be placed along a PV module, so that the azimuth of this PV module is the same as the azimuth of the iPhone 4 displayed. In order to keep a PV module conforming to the same definition of solar geometry, i.e. when an iPhone 4 faces south through west to north, the heading values relative to true north ranging from 0° to 180° can be directly used as the azimuth of the iPhone 4. Whereas, when an iPhone 4 faces north through east to south, the heading values relative to true north ranging from 180° to 360° have to subtract a 360° to represent the azimuth of the iPhone 4.

Slope of a PV module

In the segment button "Sensor", the class "CMMotionManager" of the framework "CoreMotion" is set up and its update is called when the view of the tab "Mounting" is loaded. It provides an app with a device's accelerometer data, rotation-rate data, magnetometer data and device-motion data such as "attitude". The slope of a device can be provided by the Euler angle pitch of the attitude data. Under the segment Sensor: an iPhone 4 can be placed on a mounted PV module, such that the slope of this PV module is the same as the slope of the iPhone 4. The range of the slope is between 0° and 90°.

6.A.4 Tab: Skyview

This is the view where a user reads the final results. The solar radiation model underpins this tab. When a user presses the button "Camera", a video preview based on the framework "AV Foundation" is loaded, which is the gateway to play and create time-based audio-visual media.

Due to the usage of the app, only the back-facing camera of the iPhone 4 is connected. The property "focusMode" of the class "AVCaptureDevice" is set to be "AVCaptureFocusModeContinuousAutoFocus". In this way, the back-facing camera continuously monitors focus and auto focuses when necessary. The class CMMotionManager is also used here to continuously detect the slope of iPhone 4, once the slope hits 90°, an image is taken automatically. This is done by the method "captureStillImage" of the class "AVCamCaptureManager"

If an image taken is satisfactory, the button "use" is pressed to save it; otherwise, "retake" is pressed to discard it. The button "finish" is used to stitch together all saved images, which typically takes several minutes (depending on the number of images). The stitch function is implemented by the package "StitchImgViewController" of OpenCV. The method "scrollView" of the class "UIScrollView" is used to properly display the panoramic picture. The "clear" button deletes all images stored in the app's local document storage.

As shown in Figure 6.3, the stitched panoramic picture is shown in the iPhone 4 screen and is scrollable. There are two buttons appearing meanwhile. Pressing the button "Return" goes back the Tab: Skyview. By pressing the button "Satisfied", the panoramic picture is converted into black and white by the method "cv::Canny" of OpenCV. The two sliders in this page are for the low and high thresholds of Canny edge detection function. Pressing the button "Satisfied" on this page gets back to the Tab: Skyview and calculates elevation of shadings. Press "Evaluate" computes and displays the power output. The button "Optimise" is used to display efficiency using the running bar, which ranges between 0 and 1.

Chapter 7

Numerical spectral-based simulations of rectangular and cylindrical 2-layer luminescent solar concentrators

Abstract

An analytical model of externally-coated, rectangular and cylindrical luminescent solar concentrators (LSCs) have been developed, which are able to estimate the residual intensity (RI) as a function of wavelength, concentration of luminescent dye and device dimension. In order to examine the behaviour of solar radiation in various wavelength ranges and optimise the RI reaching the collectors at the edges of the LSCs, we investigate four kinds of luminescent dye (Lumogen Red, DCM2, DCJTB and DCM), different concentrations of dyes and length of concentrator. Seven commonly used solar cells (c:Si, mc:Si, a:Si, CIGS, TJGalnAs, TJGaInP and GaAs) are evaluated with respect to the output of the model.

We found that the Lumogen Red has a better performance than other dyes in most cases. For Lumogen Red and DCM, the lower concentration of dye, the bet-

ter the performance. In the cases of DCM2 and DCJTB, when the wavelength is less than ∼620 nm, the concentration-performance relationship is similar to that of Lumogen Red and DCM; otherwise, the higher concentration of the dye, the better the performance. The attenuation due to the externally-coated layer does not necessarily have a stronger impact on the cylindrical LSC. After a certain wavelength, the cylindrical LSC works as well as the square LSC, despite its longer optical path. Our experiments also show that the shorter the LSCs, the better the performance. A red-shift (shift to longer wavelengths) occurs when the length increases due to more attenuation in the longer paths. The reduced RI in cylindrical LSC is about uniform; however, the impact of long paths becomes stronger when the length exceeds a certain threshold in the case of square LSC. Among the seven evaluated solar cells, TJGalnAs is the most efficient solar cell.

This work is being submitted to *Journal of Lightwave Technology* (Wang et al., 2014a). The authors are Yimin Wang, Giuseppe Colantuono, Adam P. Green, Róbert Erdélyi and Edward Hanna.

Keywords: luminescent dye; photovoltaic; wavelength.

7.1   Introduction

Numerous efforts have recently been made to reduce the cost of photovoltaic (PV) conversion from sunlight. Luminescent solar concentrators (LSC) represent one of the techniques under development. The basic idea of LSC devices is to use a system of luminescent dyes to guide sunlight inside the LSC by the law of total internal reflection onto the edges of the device, where PV cells are located (McIntosh et al., 2007). Luminescent dye can absorb a photon and emit it with a new wavelength. Various species of luminescent dyes can absorb and emit different bands of wavelengths of radiation. Publications on LSCs first emerged in the late 1970s in Weber and Lambe (1976) and Goetzberger and Greubel (1977). Debije and Verbunt (2012)

state that luminescent dyes can be dispersed within a thin layer. In this way, the emitted light can travel mainly in the clear, thicker inner material. The efficiency of the power conversion of LSCs including solar cells is about 4-7% (Sloof et al., 2008; Currie et al., 2008; Goldschmidt et al., 2009). The maximum optical concentration of LSC is theoretically limited by re-absorption losses due to the overlap of absorption and emission spectra (Smestad et al., 1990; Rowan et al., 2008). Larger wavelength shifts can decrease the re-absorption of sunlight that is emitted by luminescent dyes (Batchelder et al., 1979, 1981).

Colantuono et al. (2013) found that LSCs with luminescent dye dispersed only in a thin external layer have greater optical efficiency than their homogenous counterparts. A significant proportion of the incident sunlight is trapped in the LSC by total internal reflection due to the higher index of refraction of the host material (n_i) and external layer(s) (n_e) than that of the air (n_{air}), and is led towards the edges. In Figure 7.1, the thin solid line represents a beam emitted from a dye particle located in P and travelling to the edge of the device.
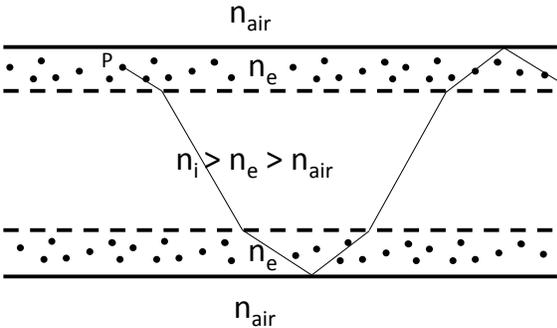
Figure 7.1: Refractive index of a standard rectangular LSC.

Numerous examples of ray-tracing applied to homogeneous LSCs exist in the literature, the best known being probably Batchelder et al. (1979). McIntosh et al. (2007) used applied ray-tracing to a cylindrical concentrator. Colantuono et al. (2013) constructed, as a generalisation of McIntosh et al. (2007), a numerical model for predicting the performance of rectangular and cylindrical 2-layer LSCs. To understand the variability of the residual intensity (RI), which is the fraction of the emitted light

collected by solar cells, the geometrical concentration (GC), which is the ratio of the light-harvesting area to the solar cells area, and the optical concentration (OC), which is the product of RI and GC, a sequence of experiments was conducted in Colantuono et al. (2013) on pairs of square and cylindrical 2-layer LSCs without taking into account the wavelength-dependence of sunlight. Key parameters including the indices of refraction for both layers, the ratios of external to internal attenuation coefficient and the outer layer thickness, were varied one at a time during the experiments. Colantuono et al. (2013) found that the square LSC always yields a higher RI. The cylindrical LSC, however, always has a better GC than the square one; unfortunately, this does not necessarily guarantee a higher OC. As the external region becomes thicker and contains more luminescent dye, the output is reduced more strongly from the cylindrical LSC than the square one. When the external index of refraction (n_e) is fixed, the higher the internal index of refraction (n_i), the better performance of the LSCs. When isotropic diffuse radiation is considered, the cylindrical LSC's OC increases by a factor of π compared with the square one. This becomes an advantage of the cylindrical LSC, especially in cloudy weather conditions when there is only diffuse solar radiation. Moreover, a smaller LSC is more efficient than a larger one.

In this chapter, we explore the variability of RI as function of wavelength; the integral of RI (IRI) on the whole spectrum is then computed. LSC size, dye concentration and the species of luminescent dye are varied in a sensitivity study of the LSCs behaviour. For each dye species, their different absorption and emission spectra are taken into account. Additionally, by using the refractive index dispersion relation, $n(\lambda)$, the trapping and refraction properties are modelled as a function of wavelength. Since the RI of an LSC depends predominantly on the absorption and emission spectra of the dye, we, hereby, analyse four kinds of commonly used luminescent species: Lumogen Red and DCM family including DCM2, DCJTB and DCM. Lumogen Red is one of the most efficient fluorescent dyes currently available organic dye materials for LSCs (van Sark et al., 2008). It has been seen to be very chemically

stable, which means it can last under exposed conditions (to sunlight/weather) for longer than many dyes (van Sark et al., 2008). DCM2, DCJTB and DCM have a larger Stoke's shift (i.e. less self-absorption) than any of the Lumogen series (Green et al., 2013). Although they have lower quantum yields than the Lumogen family, they are a good test for the LSC model because of the important property of a high Stoke's shift. We demonstrate that our analyses can give a useful insight into the physics of a layered LSC, and distinguish the behaviour of sunlight in the different layers according to wavelength.

7.2 Escape Cone Loss (ECL) of 2-layer cylindrical LSC

A beam of light impinging a luminescent dye in the external layer of the LSC is emitted in all directions. Following Colantuono et al. (2013), an escape-cone can be expressed by the angles α and β, as shown in Figure 7.2. The plane of α is parallel to the cylinder axis and that of β is normal to the cylinder axis.
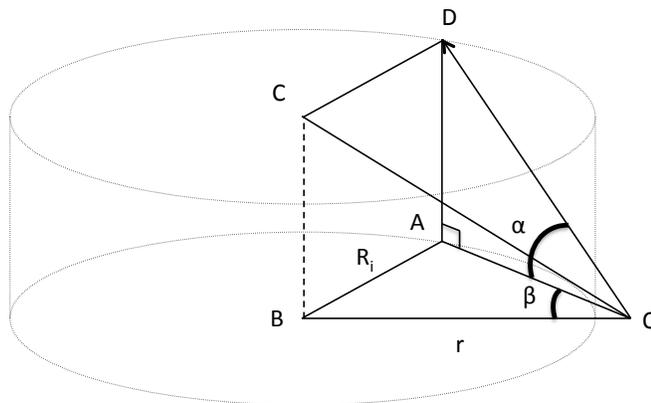
Figure 7.2: Propagation of a ray emitted from the point O onto D in the external layer of a 2-layer cylindrical LSC. The point A is the projection of the point D, the angle α is defined between DOA. The angle β is on the plane AOB that is perpendicular to the plane defined by DOA.

There are two phenomena that may happen after emission:

1. When the emitted light hits the inner layer before hitting the external interface, i.e.,

$$-\arcsin\frac{R_i}{r} < \beta < \arcsin\frac{R_i}{r}, \tag{7.1}$$

   where R_i and r are the radius of the inner cylinder and emitting point, respectively.

2. Otherwise, if the angle of incidence of the light impinging the LSC surface is bigger than its critical angle, this light can be trapped, i.e.,

$$\arcsin\frac{R_i}{r} < \beta < 2\pi - \arcsin\frac{R_i}{r}. \tag{7.2}$$

The critical angle is the opening angle of the escape-cone. In a 2-layer cylindrical LSC, the critical angle for the external layer is

$$\cos\alpha_C^e = \frac{\sqrt{1 - n_e^{-2}(\lambda)}}{\sqrt{1 - (r/R_e)^2 \sin^2\beta}}, \tag{7.3}$$

where R_e is the radius of the external cylinder and λ is the wavelength. The beam hitting the LSC-air surface with an angle smaller than the critical angle α_C^e will leave the LSC and is lost forever (Goetzberger and Greubel, 1977).

7.3 Absorption of 2-layer cylindrical and "sandwich" rectangular LSC

Once the ECL is known, the path and the properties of the trapped light can be determined. The absorption losses, i.e. attenuation and re-absorption losses for the trapped light, have been quantified in Colantuono et al. (2013). The proportion of the total light emitted in the cylindrical LSC's doped region, which reaches the solar

cells, is

$$
\begin{aligned}
I_{cyl}^{tot}(\lambda) \;=\; & \frac{1}{2\pi L} \int_0^L dx \int_0^{\frac{\pi}{2}} d\beta \int_{\alpha_C^e}^{\frac{\pi}{2}} \cos\alpha \Big(I_{right}^{direct}(\lambda) \\
& + I_{right}^{reflected}(\lambda) + I_{left}^{direct}(\lambda) \\
& + I_{left}^{reflected}(\lambda) \Big) d\alpha.
\end{aligned}
\tag{7.4}
$$

Here, I_{right}^{direct} and I_{left}^{direct} represent the light emitted directly into the right and left internal layer, respectively. $I_{right}^{reflected}$ and $I_{left}^{reflected}$ represent the light emitted towards the right and left external interface, and reflected back, respectively.

The analogous proportion of the total light emitted in the rectangular LSCs doped region, which reaches the solar cells, is

$$
\begin{aligned}
I_{rect}^{tot}(\lambda) = & \frac{1}{2\pi L_L L_S} \int_0^{L_L} dx \int_0^{L_S} dy \\
& \int_{\arcsin(n_e^{-1})}^{\frac{\pi}{2}} \sin\beta d\beta \int_0^{2\pi} d\alpha \exp \\
& \left\{ \frac{ -D(\alpha) \left[\frac{2 Z_{ext} \xi_e(\lambda)}{\cos\beta} + \frac{Z_{int} \xi_i(\lambda) n_i(\lambda)}{\sqrt{n_i^2(\lambda) - n_e^2(\lambda) \sin^2\beta}} \right] }{ 2 Z_{ext} \tan\beta + \frac{Z_{int} n_e(\lambda) \sin\beta}{\sqrt{n_i^2(\lambda) - n_e^2(\lambda) \sin^2\beta}} } \right\},
\end{aligned}
\tag{7.5}
$$

where L_L and L_S are the lengths of the two largest sides of a rectangle, respectively. $D(\alpha)$ is the distance from the emission point to the perimeter of the rectangle. The thickness of the rectangle is $Z_{tot} = Z_{int} + 2 Z_{ext}$, where Z_{int} and Z_{ext} are the internal and external thicknesses, respectively. ξ_e and ξ_i are the attenuation coefficients of the external and the internal layers, respectively.

7.4 Results

We run numerical experiments for various concentrations of four species of commonly used luminescent dyes: Lumogen Red, DCM2, DCJTB and DCM. We, further, evaluate RI for various lengths of LSCs.

Note that $n_i > n_e$. In this work, we use PMMA as the external host material, and polycarbonate as the internal host material. The external and internal refractive index dispersion relations are given by Polyanskiy (2013) and Kasarova et al. (2007), i.e.

$$
\begin{aligned}
n_e(\lambda) &= (2.40 - 8.31 \times 0.01 \times \lambda^2 - 1.92 \times 0.1 \times \lambda^{-2} \\
&\quad + 8.72 \times 0.01 \times \lambda^{-4} - 1.67 \times 0.01 \times \lambda^{-6} \\
&\quad + 1.17 \times 0.001 \times \lambda^{-8})^{1/2},
\end{aligned}
\tag{7.6}
$$

and

$$
\begin{aligned}
n_i(\lambda) &= (2.63 - 7.94 \times 0.01 \times \lambda^2 - 1.73 \times 0.1 \times \lambda^{-2} \\
&\quad + 8.61 \times 0.01 \times \lambda^{-4} - 1.62 \times 0.01 \times \lambda^{-6} \\
&\quad + 1.13 \times 0.001 \times \lambda^{-8})^{1/2}.
\end{aligned}
\tag{7.7}
$$

The chosen diameter of the cylindrical LSC is 0.4 cm, which is also the thickness of the square LSC. The length of the cylinder, and length of the sides of the square LSCs are all 1 cm. These size parameters are fixed for the wavelength analysis, but are varied between 1 cm and 1 m in the LSC dimension analysis. The ratio of the internal depth to the total diameter for both LSCs is fixed at 0.95, which is randomly chosen and this parameter does not affect the pattern of the following analysis. The shapes of the absorption and emission spectra depend on both wavelength and concentration of dye. We use four values of concentrations for each dye, which are 10^{-4}, 10^{-3}, 10^{-2} and 10^{-1} mol/litre. We assume a constant attenuation coefficient of $\xi_i = 0.035$ cm^{-1} for the host materials. This is to ensure that the attenuation coefficient of the host material is much weaker than that of the external layer, because the dissipative re-absorption and re-emission process occurs in the external layer only. The external

attenuation coefficient ξ_e is given by

$$\xi_e = C_d \times \xi_d + \xi_i, \tag{7.8}$$

where C_d is the concentration of dye and ξ_d is its absorption spectrum with units $\mathrm{mol}^{-1}\mathrm{cm}^{-1}$. It is the number of photons absorbed at a given dye concentration over a given length in cm.

7.4.1 Variation of the species and concentrations of luminescent dyes

Different concentrations of dye are examined in the numerical experiments. The lowest concentration is not guaranteed to optimally absorb sunlight. The optimal absorption of sunlight as a function of external layer thickness and as function of concentration is not determined here. Here, we examine attenuation and frequency shift of the spectrum independently from the absorption of incident light.

Figure 7.3 shows the RI for four kinds of dye with their respective concentrations. The blue, red, green and black curves represent the concentration value of dye 10^{-4}, 10^{-3}, 10^{-2} and 10^{-1} mol/litre, respectively. The length of the cylinder, and length of the sides of the square LSCs are all 1 cm. The following observations can be made.

1. Tables 7.1a and 7.1b show the IRI for cylindrical and square LSCs, respectively. With the same species and concentration of dye, the square LSC always has greater IRI than the cylindrical LSC, which is consistent with the finding in Colantuono et al. (2013), where wavelength dependency is ignored;
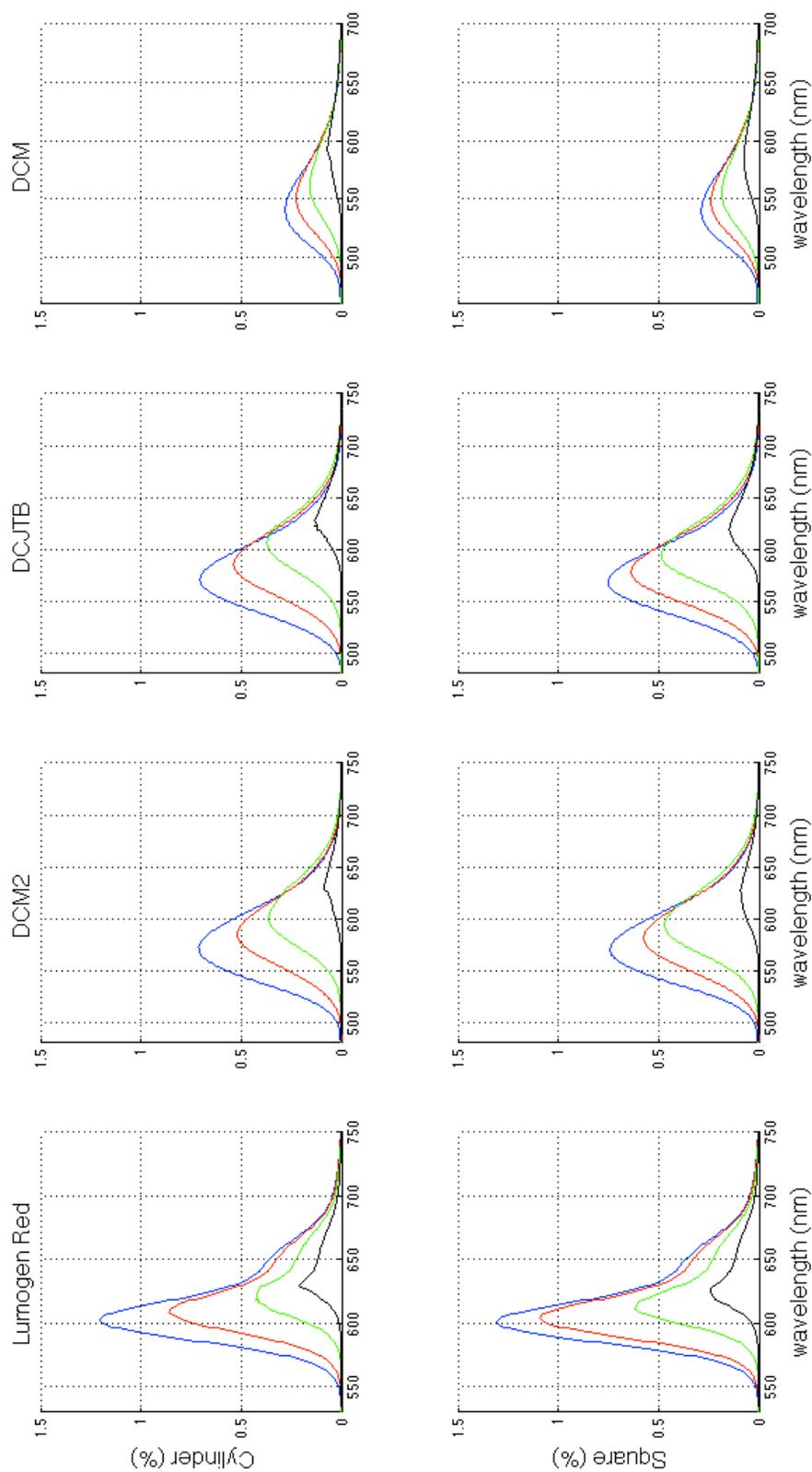
Figure 7.3: RI for four species of dye and two shapes of LSC (i.e. square and cylindrical). The blue, red, green and black curves represent the concentration values of dye 10^{-4}, 10^{-3}, 10^{-2} and 10^{-1} mol/litre, respectively. The emission spectra for all species of dye and concentrations are normalised by the integral of the emission spectrum of Lumogen Red at the concentration value of 10^{-4} mol/l. y-axis shows percentage of the emitted light by Lumogen Red at the concentration value of 10^{-4} mol/l. The length of the cylinder, and length of the sides of the square LSCs are all 1 cm.

Table 7.1a: Integral of residual intensity (IRI) for each dye under each concentration of cylindrical LSC. The emission spectra for all species of dye and concentrations are normalised by the integral of the emission spectrum of Lumogen Red at the concentration value of 10^{-4} mol/l. Therefore, the emitted light of Lumogen Red at the concentration value of 10^{-4} mol/l is 100%. The IRI values in this table show the percentages of the 100% emitted light by Lumogen Red at the concentration value of 10^{-4} mol/l.

Cylindrical LSC (%)	10^{-4} mol/l	10^{-3} mol/l	10^{-2} mol/l	10^{-1} mol/l
Lumogen Red	68.33	49.84	24.81	9.60
DCM2	63.16	44.84	30.27	5.54
DCJTB	60.89	45.37	28.69	8.05
DCM	24.58	19.70	13.63	5.34

Table 7.1b: Integral of residual intensity for each dye under each concentration of square LSC. The emission spectra for all species of dye and concentrations are normalised by the integral of the emission spectrum of Lumogen Red at the concentration value of 10^{-4} mol/l. Therefore, the emitted light of Lumogen Red at the concentration value of 10^{-4} mol/l is 100%. The IRI values in this table show the percentages of the 100% emitted light by Lumogen Red at the concentration value of 10^{-4} mol/l.

Square LSC (%)	10^{-4} mol/l	10^{-3} mol/l	10^{-2} mol/l	10^{-1} mol/l
Lumogen Red	73.41	60.75	32.96	12.11
DCM2	65.70	50.28	39.07	7.04
DCJTB	64.83	54.10	38.53	10.00
DCM	25.24	21.04	16.20	6.42

2. For a given concentration, Lumogen Red always has the highest peak among the four dyes. However, Lumogen Red has the highest IRI for both the cylinder and the square, except when the dye concentration is 10^{-2} mol/l, under which condition the DCM2 and DCJTB are more efficient;

3. For Lumogen Red, the lower concentration of dye, the better the performance; DCM has the same trend. However, when the wavelength of DCM2 and DCJTB is greater than ~ 620 nm, the higher the concentration of dye, the better the performance. This results from a red-shift (shift to longer wavelengths) of the emission spectra of DCM2 and DCJTB when the concentrations of dyes increase. This is caused by a phenomenon called Solvation. As dye concentration

increases the average relative permittivity (dielectric constant) increases, causing a shift in emission for the DCM class dyes, but not for Lumogen Red. This is for quite complex physical reasons to do with the way charge is distributed across the molecules. Taking this into account, the difference caused by the red-shift for the highest concentration 10^{-1} mol/l of DCM2 and DCJTB is only $\sim 1\%$ of the peak value, so can be ignored. There are redshifts for the longer wavelength of DCM, but the difference resulting from these shifts is smaller than 1% and is thus ignored;

4. Figure 7.4 (a) depicts IRI for four species of dye as function of concentration. Colantuono et al. (2013) found that both the cylindrical and square LSCs are sensitive to the variation of the attenuation of the external layer: higher absorption has stronger impact on the cylindrical than the square LSC. However, in Figure 7.4, the percentage loss of the cylindrical LSC with respect to the square LSC as a function of wavelength for each species and concentration of dye is shown. The percentage loss is defined by the RI of the cylindrical and square LSCs:

$$\text{Percentage loss} = \frac{RI_{\text{cyl}} - RI_{\text{sq}}}{RI_{\text{sq}}} \times 100. \tag{7.9}$$

Figure 7.4 explains that, apart from a negligible attenuation difference due to PMMA, the cylindrical and square LSCs have a similar output after a certain wavelength (~ 630 nm), despite the cylindrical LSCs longer optical paths. The overestimation of the attenuation in Colantuono et al. (2013) is a natural consequence of re-absorption being assumed to be independent of wavelength. Since the cylindrical LSC is more sensitive to reabsorption due to long paths like the spiral rays and more interface-crossings, the overestimation in Colantuono et al. (2013) is stronger for the cylindrical than the square LSC.
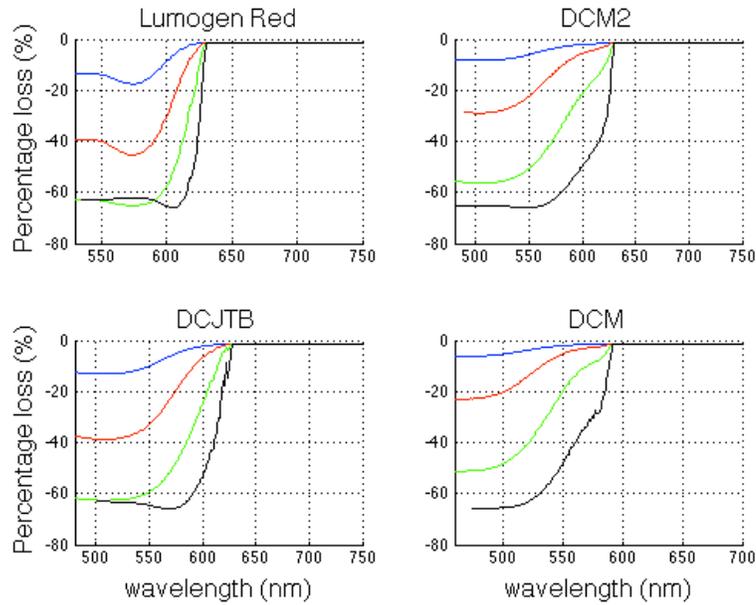
Figure 7.4: Percentage loss of the cylinder with respect to the square LSCs for four species of dye as function of the wavelength. The colors of lines express the same concentrations as in Figure 7.3.

7.4.2 Variations of the length of LSCs

Figure 7.5 shows RI of DCJTB with various lengths of LSCs. All the parameters are kept the same, but the length of the cylinder or side length of the square. The blue, red and black curves represent the same concentration of DCJTB with length 1 cm, 10 cm and 100 cm, respectively. The green dashed curve in Figure 7.5 represents the emission spectrum, which has been normalised by its area: thus the total emission spectrum is 100%.

In summary, from Figure 7.5, we conclude that:

1. The shorter the LSCs, the better the performance;

2. There is a red-shift when the length increases, due to greater attenuation at each wavelength;

3. The three peaks in the sub-figure of cylindrical LSC appear redshifted compared to their counterparts for the square LSC. This implies that the cylindrical LSC

131
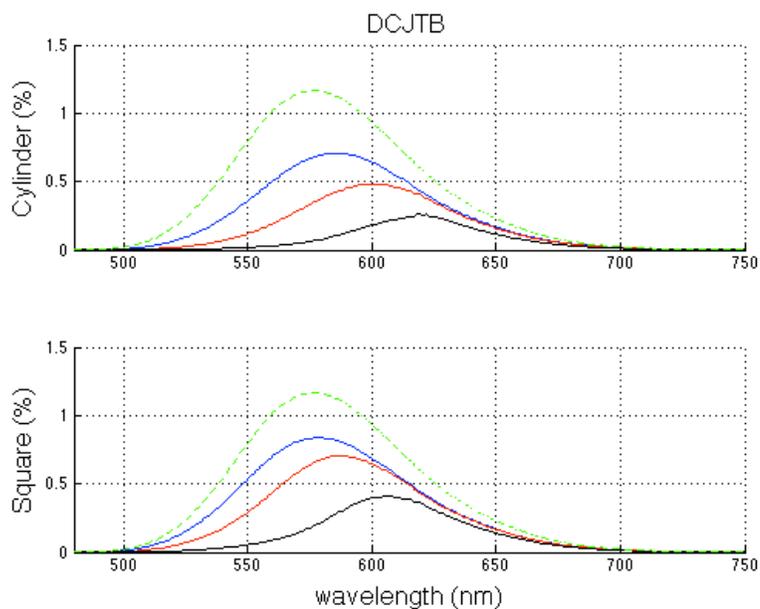
Figure 7.5: RI for DCJTB with various lengths of LSCs. The length of cylinder or the side of square increases following the color of the three solid lines: blue (1 cm), red (10 cm) and black (100 cm). The green dashed line depicts the emission spectrum at the same concentration of DCJTB. The emission spectrum is normalised by its area, thus the integral of the emission spectrum is 100%. y-axis shows percentage of the emitted light by DCJTB at the concentration value 10^{-3} mol/l.

is more sensitive to attenuation than the square LSC, which is consistent with the findings of Colantuono et al. (2013). This higher sensitivity of attenuation of the cylindrical LSC can result from long paths such as spiral rays in the cylinder, and the greater average number of interface-crossings in the cylinder before reaching the edges;

4. As length increases, the reduction of IRI of cylindrical LSC is about linear. However, in the square LSC, the decrease of IRI becomes much greater between 10 cm and 100 cm, compared with that between 1 cm and 10 cm. This phenomenon may be explained that when the length of square exceeds a certain threshold, the impact of long paths becomes stronger.

We only show DCJTB here since the other three species of dye and their concentrations have the similar pattern.

7.4.3 Variation of the species of solar cells

Figure 7.6 shows the generated power (denoted as GP, i.e. the fraction of the power re-emitted by Lumogen Red) of the square LSC including seven kinds of commonly used solar cells, which are crystalline silicon (c:Si), multi-crystalline silicon (mc:Si), amorphous silicon (a:Si), copper indium gallium selenide (CIGS), triple-junction gallium indium arsenide (TJGaInAs), triple-junction gallium indium phosphide (TJGaInP) and gallium arsenide (GaAs). GP is the product of RI and the efficiency of each solar cell. DCJTB is not shown because its performance is very similar to DCM2. Only the square LSC is evaluated; the cylindrical LSC has proportional results.

1. TJGalnAs is the most efficient solar cell of the set, except for certain longer wavelengths. This is because its peak performance happen between ~ 530 nm and ~ 610 nm, which overlaps the peaks of the RI in all cases.

2. CIGS outperforms GaAs at shorter wavelengths ($< \sim 565$ nm); while GaAs performs better than CIGS at longer wavelengths ($> \sim 565$ nm). This is because
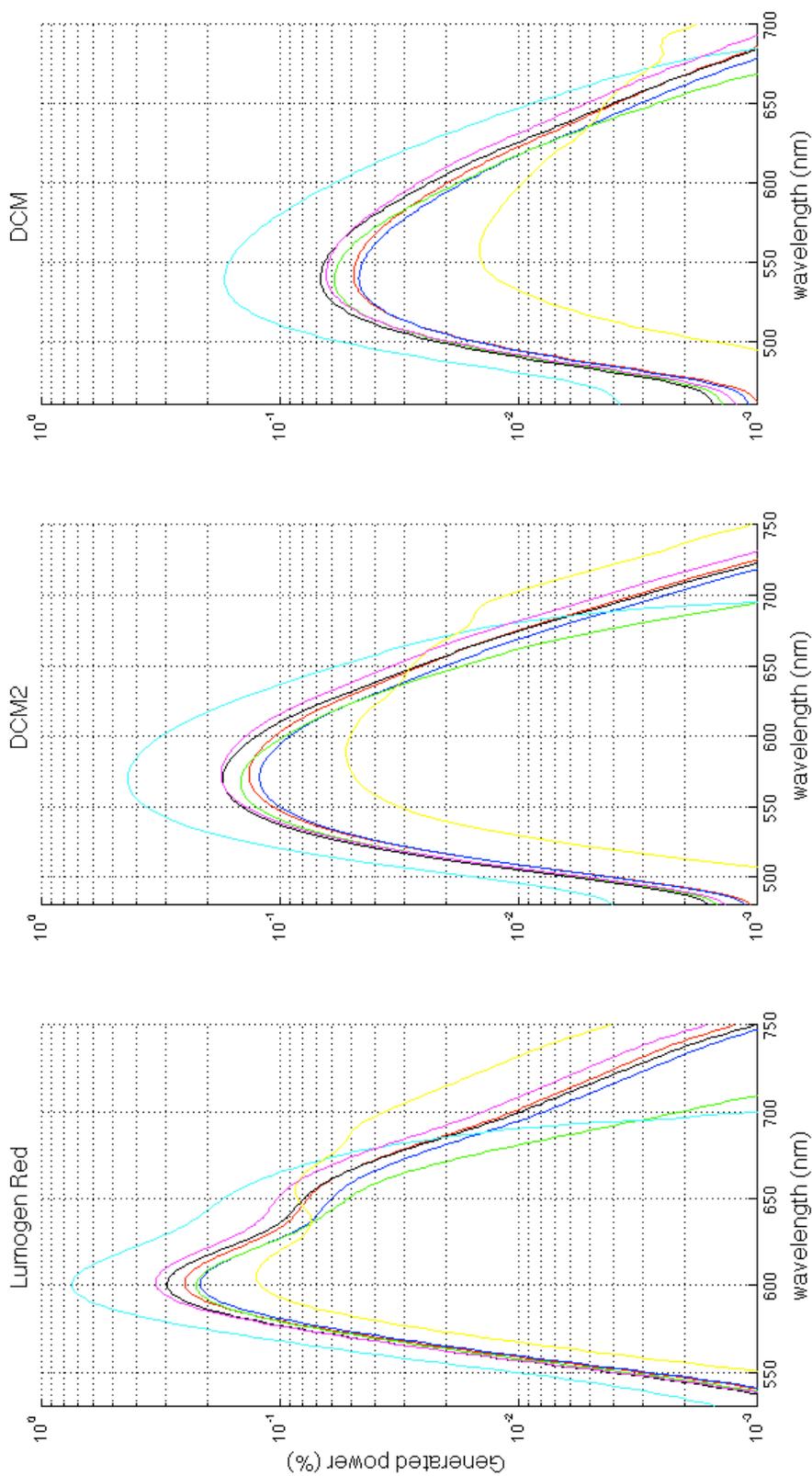
Figure 7.6: The generated power for the square LSC for three species of dye with the concentration value of 10^{-4} mol/l. Red, blue, green, black, cyan, yellow and magenta lines depict five kinds of solar cells for the square LSC, which are c:Si, mc:Si, a:Si, CIGS, TJGaInAs, TJGaInP and GaAs respectively. Each emission spectrum is normalised by the emission spectrum of Lumogen Red, thus the emitted light by Lumogen Red is 100%. y-axis shows the percentage of this 100% emitted light by Lumogen Red at the concentration value of 10^{-4} mol/l. DCJTB is not shown because its performance is very similar to DCM2.

Table 7.2: The integral of the generated power (IGP) for all wavelengths for the square LSC with Lumogen Red, DCM2 and DCM. The concentration is 10^{-4} mol/l. All emission spectra are normalised by the emission spectrum of Lumogen Red, thus the emitted light of Lumogen Red is 100%. The IGP values in this table show the percentages of this 100% emitted light by Lumogen Red at the concentration value of 10^{-4} mol/l. DCJTB is not shown because its performance is very similar to DCM2.

Square LSC (%)	c:Si	mc:Si	a:Si	CIGS	TJGaInAs	TJGaInP	GaAs
Lumogen Red	14.37	12.09	11.89	16.39	38.58	10.77	19.09
DCM2	12.09	10.74	12.08	15.04	37.02	5.95	15.91
DCM	4.41	4.09	4.94	5.83	14.61	1.51	5.77

the peak absorption of CIGS is between $\sim$ 530 nm and 550 nm, whereas for GaAs it is $\sim$ 830 nm;

3. Similarly, CIGS has a better performance than c:Si when the wavelength is shorter than $\sim$ 665 nm; c:Si results in higher GP when the wavelength is longer than $\sim$ 665 nm;

4. c:Si performs similarly to mc:Si at shorter wavelengths ($<\sim$ 510 nm), beyond which wavelength c:Si outperforms mc:Si. This is because the peak absorption of c:Si is $\sim$ 960 nm, whereas for mc:Si it is $\sim$ 690 nm;

5. a:Si outperforms c:Si and mc:Si until the wavelength longer than $\sim$ 580nm and $\sim$ 620 nm, respectively. This is because the peak absorption of a:Si is at $\sim$ 500 nm;

6. TJGaInP, which peak absorption is at $\sim$ 760 nm, is the least efficient solar cell of the set, except for certain longer wavelengths ($>\sim$ 650 nm);

Table 7.2 reveals the integral of the generated power (IGP) for all wavelengths for each solar cell. TJGaInAs has the greatest IGP of the solar cell set, followed by GaAs for Lumogen Red and DCM2, but by CIGS for DCM. Moreover, c:Si, mc:Si and a:Si have generate similar amount of IGP. TJGaInP is the least efficient solar cell among the set.

7.5 Conclusion

We generalised here the Colantuono et al. (2013) model to be capable of computing RI and IRI as a function of wavelength. We also examine four kinds of commonly used luminescent species: Lumogen Red, DCM2, DCJTB and DCM.

Among these four luminescent species, Lumogen Red has a better performance in most cases. By using Lumogen Red, the higher concentration, the lower RI and IRI; and the same trend is observed for the IRI of the whole wavelength range of DCM, as well as DCM2 and DCJTB when the wavelength is smaller than $\sim$ 620 nm. However, by applying DCM2 and DCJTB, when the wavelength is greater than $\sim$ 620 nm, the higher the concentration, the better the performance.

Greater than a certain wavelength ($\sim$ 630 nm), when the absorption spectrum of the dye approaches zero, the cylindrical LSC works as well as the square one despite the cylindrical LSC's longer optical paths. This is because the attenuation due to PMMA is negligible compared to the attenuation due to the dye.

We also found that the longer the LSC, the lower the IRI for both cylindrical and square LSCs; and, the peak of the RI curves shift to longer wavelength due to greater attenuation taking place at shorter wavelengths. The peaks of the RI curves of the cylindrical LSC always occur at longer wavelengths compared to their counterparts in the square LSC. This is because the cylindrical LSC is more sensitive to attenuation. As the LSCs dimension length increases, the IRI of the cylindrical LSC decreases more uniformly when compared with their square counterparts. This means, there is a threshold for square LSC, beyond which the impact of long paths becomes stronger.

Seven commonly used solar cells (c:Si, mc:Si, a:Si, CIGS, TJGalnAs, TJGaInP and GaAs) were evaluated. For Lumogen Red and DCM2, the performance generally decreases in the following order: TJGalnAs, GaAs, CIGS, c:Si, mc:Si, a:Si and TJGaInP; however, for DCM, the order is: TJGalnAs, CIGS, GaAs, a:Si, c:Si, mc:Si and TJGaInP.

Finally, Colantuono et al. (2013) shows for the first time the impact on RI of

giving a physical thickness to the external, emitting layer. The aim of Colantuono et al. (2013) is only to compare the zero-thickness models used before with a model where a non-zero thickness is attributed to external layer. The present work makes a significant advance in actively considering the wavelength dependence. However, direct quantitative comparison between Colantuono et al. (2013) and this work is not possible because Colantuono et al. (2013) do not use physical values of attenuation (i.e. attenuation should depend on wavelength and concentration of dye).

Chapter 8

Conclusion

In this chapter, two main points are presented. First the main contributions of this thesis are summarised, and second some suggestions are given for future work.

8.1 Main contribution of this thesis

Solar energy is a valuable renewable source that can be harnessed to provide electricity and thermal power. In order to efficiently make use of solar energy, more research on the variability of solar radiation and development of the tools for predicting solar radiation is needed.

Solar radiation received on the Earth is affected by many factors: probably the three most important of which are geographic location, local meteorology and topography. This thesis investigates solar radiation in Britain and USA for evidence of climatic effects. We found that British global radiation is generally significantly positively correlated with diffuse radiation in winter, but the correlation is much weaker and non-significant for the other three seasons and annually. In Britain, seasonal/annual cloud cover is significantly negatively correlated with seasonal/annual global radiation but is correlated with diffuse radiation only in winter when there is more cloud. This may be because the main impact of changes in cloud cover is on global (and direct) radiation; however, the diffuse radiation component may be

more affected by aerosols, which disperse solar radiation without greatly reducing its amount.

The variations of the ground-based solar radiation received on the Earth, and British cloud cover are ~ 77 and ~ 44 times that of the extra-terrestrial irradiance, respectively. Therefore, the variation of cloud cover may explain the greater magnitude of global and diffuse radiation on the Earth's surface compared with the coincident change in extra-terrestrial irradiance. We found that British and USA diffuse radiation generally lag the sunspot numbers by ~ 2 years; US global/direct radiation tends lead sunspot numbers by ~ 2 years. But no such correlation occurs between British global/direct radiation and sunspot numbers. This is most likely related to local meteorological variations in atmospheric air masses and circulation, e.g. jet stream, storminess and the North Atlantic Oscillation (NAO) changes, which affect the British climate mainly in winter. As a result, we also analysed the correlation between the NAO and solar radiation in Britain. The winter NAO index is significantly negatively correlated with British global radiation in the west of Britain; however, it is significantly positively correlated with British global radiation in the east of Britain. Moreover, the correlation between the British direct radiation and winter NAO index outperforms its NAO-global radiation correlation counterpart in winter.

Since global radiation data are commonly available, and just a few weather stations measure diffuse radiation in Britain, we analysed four models (the PVGIS, UKCP09, Liu & Jordan and Page models) which either provide both global and diffuse radiation or can deduce the diffuse component from a given global-radiation value. Our results show that the PVGIS model performs best overall out of the four models, followed by the Page, UKCP09 and Liu & Jordan models. Our results also suggest that Britain may have higher diffuse radiation fraction compared with the USA and Canada, and the global average. The USA and Canada region may have a lower diffuse radiation fraction than the global average.

Grid-connected PV systems have a number of advantages and large-scale PV

installations are a potential solution for future cities. In order to accurately estimate solar radiation in any location in a city taking into account urban terrain shading, we proposed a model SORAM. We validated SORAM against the Perez et al. (1990a) model under no shading condition. The difference between SORAM and the Perez et al. (1990a) model outputs is $-3.6 \times 10^{-3}\%$ showing a coherence of these two models. SORAM was also validated against the observed SSF solar radiation data under real shading conditions. The results show a 3.3% MBE, which is lower compared with those from the Perez et al. (1990a) against SSF data 4.6%. Therefore, SORAM overall performs better than the Perez et al. (1990a) model.

For the practical application of our SORAM model, we constructed a smart phone app for fulfilling the same function as SORAM. Instead of using a ray-tracing method in a 3D environment to determine shading conditions in SORAM, we developed a shading detection algorithm, which is based on image processing to evaluate how terrain shading affects PV modules. We validated the app using empirical measurements as well as SORAM: the results show that the app performs as well as SORAM and better than the Perez et al. (1990a) model.

For efficiently harvesting solar energy and reduce the cost of PV application, we investigate four commonly used luminescent species (Lumogen Red, DCM2, DCJTB and DCM) and seven solar cells (c:Si, mc:Si, a:Si, CIGS, TJGalnAs, TJGaInP and GaAs) for the square and cylindrical 2-layer luminescent solar concentrators (LSC). We found that the Lumogen Red performs better than the other three species, and has higher residual intensity (RI) with lower concentration of dyes. However, DCM2 and DCJTB produce higher RI with higher concentration when the wavelength of emitted light is greater than ~ 620 nm. We also found that the longer the LSCs, the lower the integrated RI for both cylindrical and square LSCs, especially for the cylindrical one before ~ 630 nm; otherwise, the cylindrical LSC works as well as the square one. For Lumogen Red and DCM2, the performance generally decreases in the following order: TJGalnAs, GaAs, CIGS, c:Si, mc:Si, a:Si and TJGaInP; however, for DCM, the order is: TJGalnAs, CIGS, GaAs, a:Si, c:Si, mc:Si and TJGaInP.

8.2　Outlook

Although several factors affecting the amount of global, direct and diffuse radiation have been evaluated and new solar radiation models that can evaluate terrain shading have been proposed and validated, the research in this area is still at a very early stage. Further research is recommended on the following topics.

1. As discussed in Chapter 2, if there are no local meteorological effects, global and direct radiation are expected to correlate with and precede sunspot numbers by ~ 2 years; while diffuse radiation is correlated with and lags sunspot numbers by ~ 2 years. Hence, it is necessary to examine solar radiation in more regions on the Earth for checking this rule. Moreover, the reason that solar radiation leads/lags sunspot numbers by ~ 2 years should be investigated. Meantime, the correlation between solar radiation and local meteorological effects, cloud cover conditions, aerosols, temperature, as well as water vapour should also be computed in order to place the above findings in a more comprehensive climatic context.

2. We have found that the winter NAO index is significantly negatively correlated with global radiation in the west of Britain; however, it is significantly positively correlated with global radiation in the east of Britain. Previdi and Veron (2007) found that high latitude North Atlantic (50°N-90°N, 100°W-40°E) cloud cover responses to NAO. The correlation between western and eastern British global radiation and sunspot numbers should be investigated separately. The eastern British global radiation is expected to correlate with sunspot numbers. The correlation between western and eastern British cloud cover and NAO should also be investigated.

3. SORAM, constructed in Chapter 5, can only treat all obstacles as boxes. However, for more accurate evaluation of shading conditions, an algorithm for efficiently detecting more complex shapes should be developed. The practical

efficiency of PV modules is also greatly influenced by the percentage of the shading. This is because partial shading may seriously decrease the available output power, as the cell having the lowest illumination determines the operating current of the whole series string. Packages for PV module arrays that can calculate this partial shading influence and be easily embedded into SORAM should be developed.

4. For models validation in Chapters 5 and 6, we compare hourly values between the models and SSF observations. Monthly and seasonal values can also be evaluated for gaining more insight of the models, e.g. for different heights of the Sun (or various levels of the shading impact), how the models perform?

5. The cylindrical LSC model applied in Chapter 7 only considers one cylinder. Both Colantuono et al. (2013) and Chapter 7 have found that larger dimension LSCs have a decreased efficiency due to their greater attenuation. Cylindrical LSCs are normally placed in an array, parallel to each other. Therefore, the mutual effect on light between two cylindrical LSCs needs to be investigated.

6. In Chapter 7, light is considered as being uniformly emitted across the external layer of the LSCs by luminescent dyes. However, in reality, direct radiation illuminating the LSCs is not uniform. Therefore, if LSC arrays can be combined with SORAM, a complete system for the prediction and optimisation of PV capability may be constructed.

7. During the analysis in Chapter 7, the emission spectrum of the luminescent dye DCM (red dashed line in Figure 8.1) is found to largely overlap with the absorption spectrum of Lumogen Red (blue solid line in Figure 8.1), while the emission spectrum of DCM rarely overlaps with the emission spectrum of Lumogen Red. Therefore, combining these two luminescent species can broaden the usable wavelength of light for either dye. However, in Chapter 7, we found that increasing the concentration of dye normally decreases residual intensity.

Hence, we need to find appropriate choices of concentrations of these two luminescent species. A model for the prediction of the residual intensity of the combination of these two luminescent species should be developed.
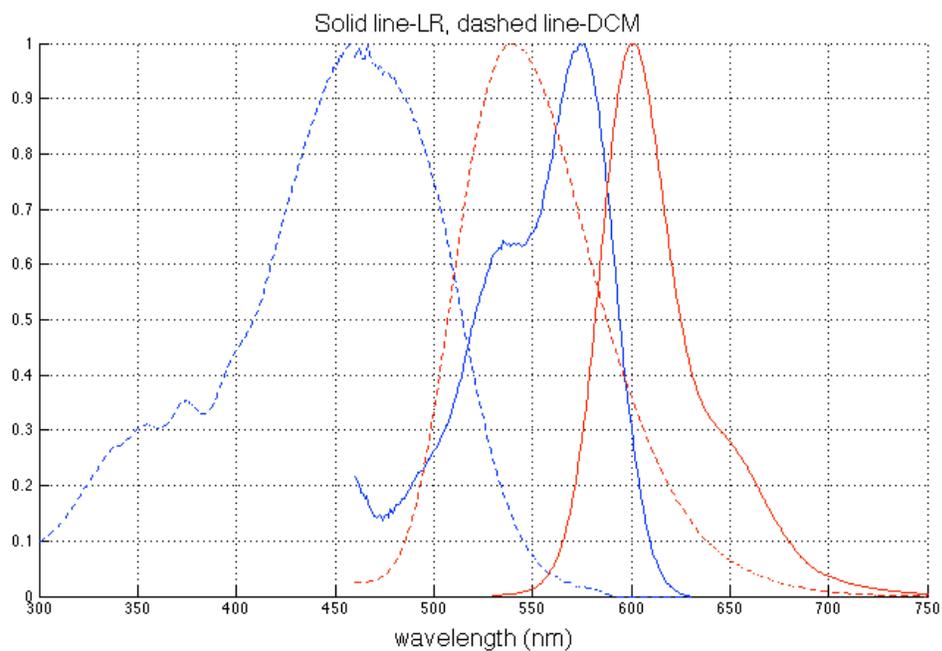
Figure 8.1: Normalised absorption and emission spectra of DCM and Lumogen Red, which are unitless. The blue lines are absorption spectra, and red lines are emission spectra. The dashed lines are for DCM, and the solid lines are for Lumogen Red.

Appendices

Appendix A

Angle of incidence of direct radiation on a PV module

The solar declination δ can be approximately expressed (Cooper, 1969)

$$\delta = 23.45° \sin\left(360° \frac{284 + n}{365}\right). \tag{A.1}$$

where n is the day of the year that can be conveniently obtained from Table A.1 (Klein, 1977).

The angle of incidence θ of direct radiation on a surface can be calculated in the following way and some of the related angles are indicated in Figure A.1.

$$
\begin{aligned}
\cos\theta \;=\;& \sin\delta \sin\phi \cos s \\
& - \sin\delta \cos\phi \sin s \cos\gamma \\
& + \cos\delta \cos\phi \cos s \cos\omega \\
& + \cos\delta \sin\phi \sin s \cos\gamma \cos\omega \\
& + \cos\delta \sin s \sin\gamma \sin\omega.
\end{aligned}
\tag{A.2}
$$

where ϕ is latitude at a position, s is slope of a PV module, γ is azimuth of a PV module, ω is the hour angle.
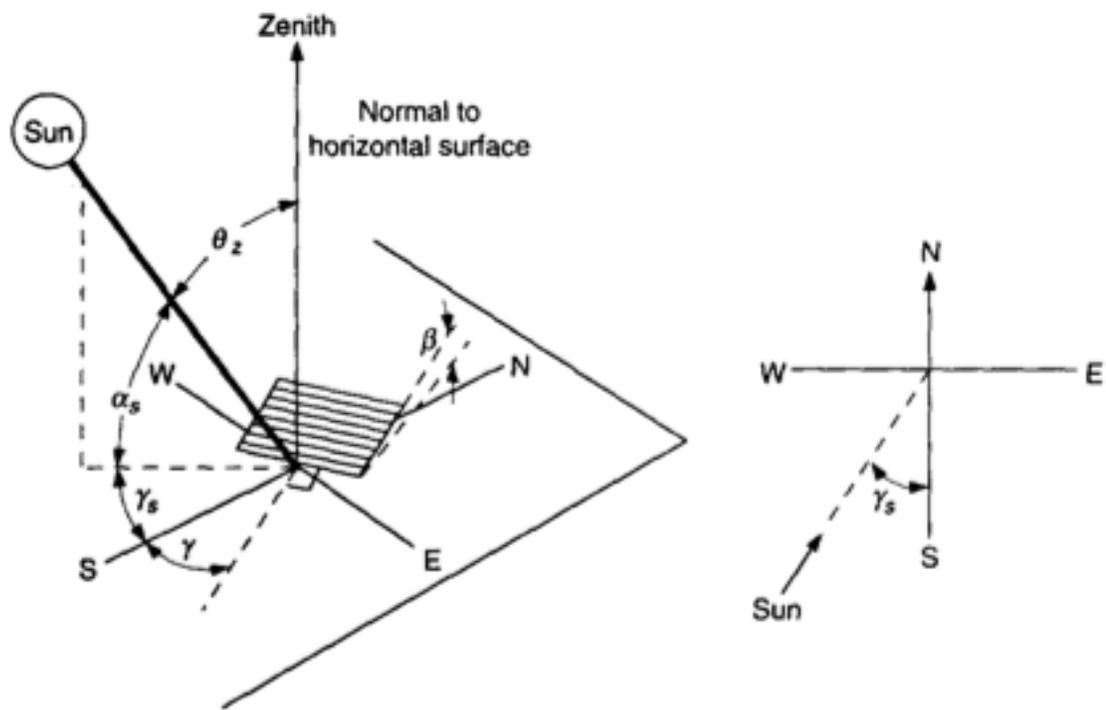
Figure A.1: Geometric relationships between a surface of any particular orientation relative to the Earth at any time and the direct radiation (Duffie and Beckman, 1991).

Table A.1: Recommended average days for each month and values of n by months

| Month | n for ith day of month | The average days for months | | |
		Date	Day of year	Declination
Jan.	i	17	17	-20.9
Feb .	31+i	16	47	-13.0
Mar.	59+i	16	75	-2.4
Apr.	90+i	15	105	9.4
May	120+i	15	135	18.8
Jun.	151+i	11	162	23.1
Jul.	181+i	17	198	21.2
Aug.	212+i	16	228	13.5
Sept.	243+i	15	258	2.2
Oct.	273+i	15	288	-9.6
Nov.	304+i	14	318	-18.9
Dec.	334+i	10	344	-23.0

For horizontal surface the slope s is zero, and the angle of incidence equals the zenith angle θ_z, and Equation A.2 becomes:

$$\cos\theta_z = \cos\phi\cos\delta\cos\omega + \sin\phi\sin\delta \tag{A.3}$$

Conversely, Equation A.3, i.e. zenith angle θ_z can also be deduced in the way shown below. Assuming the spherical coordinates are converted into the Cartesian coordinates,

$$\begin{cases} x = \cos\phi\cos\omega \\ y = \cos\phi\sin\omega \\ z = \sin\phi \end{cases} \tag{A.4}$$

where x-axis goes through local meridian that is described of meridian of observer at Q as shown in Figure A.2, and z-axis points from the center of the Earth to the North Pole, i.e. the same direction as the rotational axis of the Earth. y-axis can be regarded to direct either way, which will not affect the calculation of zenith angle θ_z.

Next step is to rotate the axis of the Earth parallel to the direction of the Sun
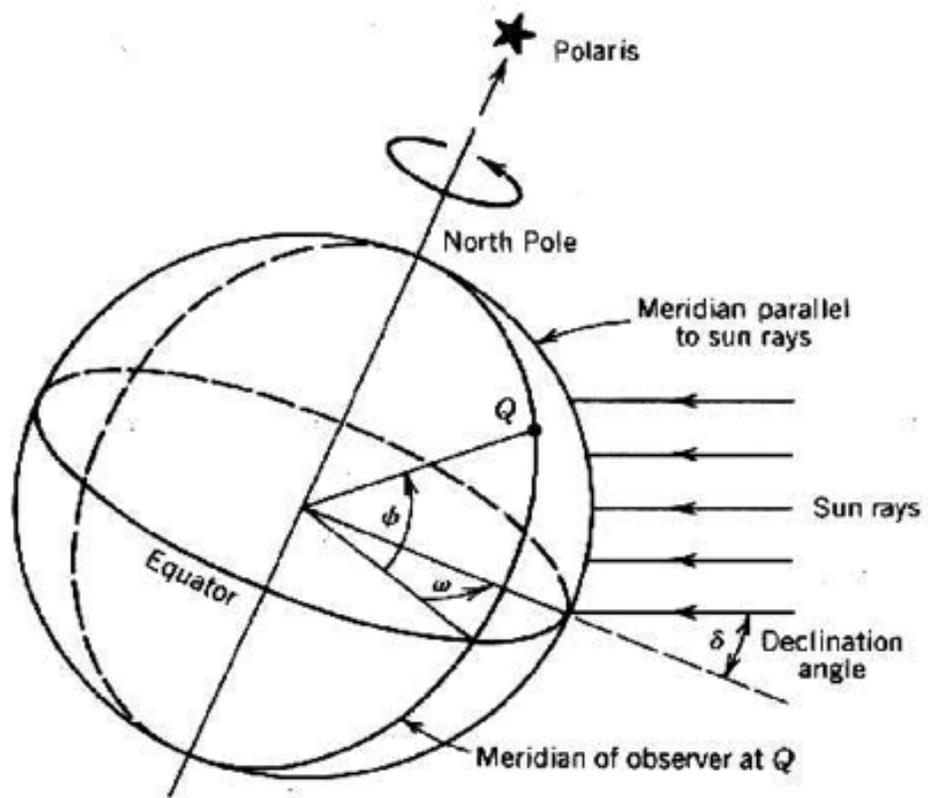
Figure A.2: Variation of the hour angle and the declination angle (Omer, 2010)

rays, that is, to rotate $x - z$ plane the angle of $\left(\frac{\pi}{2} - \delta\right)$ about the y-axis. Thus the rotation matrix is applied,

$$
\begin{bmatrix} x' \\ y' \\ z' \end{bmatrix} = \begin{bmatrix} \cos\xi & 0 & -\sin\xi \\ 0 & 1 & 0 \\ \sin\xi & 0 & \cos\xi \end{bmatrix} \begin{bmatrix} x \\ y \\ z \end{bmatrix} \tag{A.5}
$$

where $\xi = \frac{\pi}{2} - \delta$,

$$
\begin{cases} \sin\xi = \sin\left(\frac{\pi}{2} - \delta\right) = \cos\delta \\ \cos\xi = \cos\left(\frac{\pi}{2} - \delta\right) = \sin\delta \end{cases} \tag{A.6}
$$

Substituting Equations A.4 and A.6 into Equation A.5, the new expression of rotated z' in Cartesian coordinate system is given by

$$
z' = \cos\theta = \cos\theta_z = \cos\phi\cos\delta\cos\omega + \sin\phi\sin\delta \tag{A.7}
$$

where z' is $\cos\theta_z$, or $\cos\theta$ as shown in Figure A.3 with the beam radiation irradiating on the flat surface.

Equation A.7 describes the situation under where slope $s = 0$ and azimuth angle $\gamma = 0$. Now, consider that $s \neq 0$ and $\gamma = 0$ as shown in Figure A.3. The surface has the same angular relationship to direct radiation as a horizontal surface at a latitude of $(\phi - s)$. Equation A.7 is modified to

$$
\begin{aligned}
\cos\theta &= \cos(\phi - s)\cos\delta\cos\omega + \sin(\phi - s)\sin\delta \\
&= \sin\delta\sin\phi\cos s \\
&\quad - \sin\delta\cos\phi\sin s \\
&\quad + \cos\delta\cos\phi\cos s\cos\omega \\
&\quad + \cos\delta\sin\phi\sin s\cos\omega
\end{aligned} \tag{A.8}
$$

149
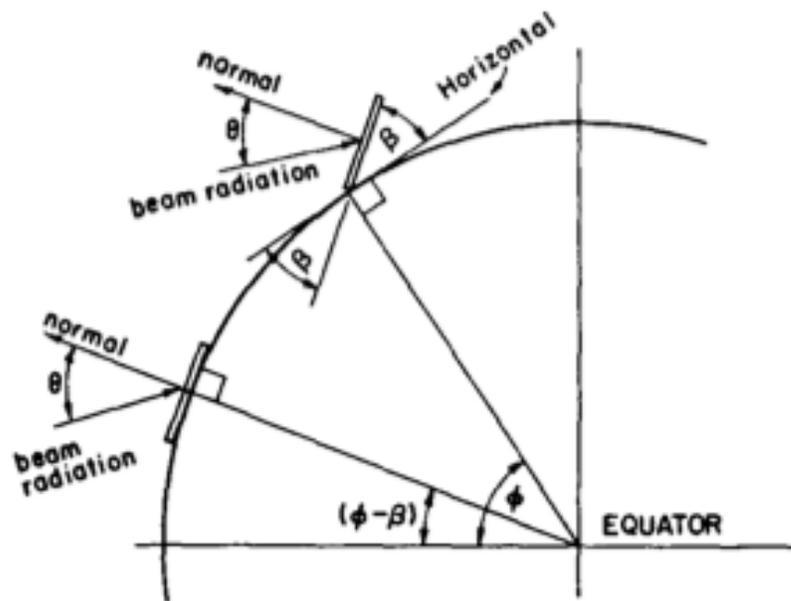
Figure A.3: Beam radiation for a south-facing surface. (Duffie and Beckman, 1991)

For the southern hemisphere, Equation A.8 is modified into

$$\cos\theta = \cos(\phi + s)\cos\delta\cos\omega + \sin(\phi + s)\sin\delta \tag{A.9}$$

Appendix B

Angle of incidence of diffuse radiation on a PV module

In spherical coordinate system, α_d and γ_d represent the altitude and azimuth of a diffuse ray, respectively. In Cartesian coordinate system, the vector of the diffuse ray (assuming originating from a PV module to the sky) $\mathbf{v_1}$ is expressed by

$$
\begin{cases}
x_1 = \cos\alpha_d \cos\gamma_d, \\
y_1 = \cos\alpha_d \sin\gamma_d, \\
z_1 = \sin\alpha_d.
\end{cases}
\tag{B.1}
$$

Similarly, if we assume that α_m and γ are the elevation and azimuth of the vector $\mathbf{v_2}$ that is normal to and originates from the PV module, it can be expressed by

$$
\begin{cases}
x_2 = \cos\alpha_m \cos\gamma, \\
y_2 = \cos\alpha_m \sin\gamma, \\
z_2 = \sin\alpha_m.
\end{cases}
\tag{B.2}
$$

Use the dot product to the get the angle of incidence θ_d between the diffuse ray and the PV module, and note $\alpha_m = \pi/2 - s$,

$$
\begin{aligned}
\cos \theta_d &= \mathbf{v_1} \cdot \mathbf{v_2} \\
&= \cos \alpha_d \cos \gamma_d \cos \alpha_m \cos \gamma_m \\
&\quad + \cos \alpha_d \sin \gamma_d \cos \alpha_m \sin \gamma_m + \sin \alpha_d \sin \alpha_m \\
&= \sin(\alpha_d) \cos s + \cos \alpha_d \sin s \cos(\gamma_d - \gamma). \quad (B.3)
\end{aligned}
$$

Appendix C

The Sun's position

Equation A.3 can be used to solve the sunrise/sunset hour angle, when $\theta_z = 90°$:

$$\cos \omega_s = -\frac{\sin \phi \sin \delta}{\cos \phi \cos \delta} = -\tan \phi \tan \delta, \tag{C.1}$$

Therefore, the hour angle is in the range of $[-\omega_s, \omega_s]$ with $15°$ as the step size for hourly direct radiation.

Solar altitude α_s and solar azimuth γ_s are used to describe the Sun's position. The solar altitude is defined in the range of $0°$ and $90°$, and is given by

$$\alpha_s = 90° - \theta_z. \tag{C.2}$$

The solar azimuth is between $-180°$ and $180°$, and is

$$\gamma_s = C_1 C_2 \gamma_s' + C_3 \left(\frac{1 - C_1 C_2}{2} \right) 180° \tag{C.3}$$

where

$$\sin \gamma_s' = \frac{\sin \omega \cos \delta}{\sin \theta_z} \tag{C.4}$$

$$C_1 = \begin{cases} 1, & \text{if } |\omega| < \omega_{ew} \\ -1, & \text{otherwise} \end{cases} \tag{C.5}$$

$$C_2 = \begin{cases} 1, & \text{if } \phi(\phi - \delta) \geqslant 0 \\ -1, & \text{otherwise} \end{cases} \tag{C.6}$$

$$C_3 = \begin{cases} 1, & \text{if } \omega \geqslant 0 \\ -1, & \text{otherwise} \end{cases} \tag{C.7}$$

$$\cos \omega_{ew} = \frac{\tan \delta}{\tan \phi}. \tag{C.8}$$

Appendix D

Global radiation on a tilted surface on a daily scale

Global radiation on a tilted surface G_s can be expressed by

$$G_s = RG = RK_tG_0 \tag{D.1}$$

where R is the ratio of global radiation on a tilted surface to that on a horizontal surface; G_h is global radiation on a horizontal surface; G_0 is extraterrestrial radiation whereas K_t is defined to be the ratio of global radiation on a horizontal surface to extraterrestrial radiation.

$$K_t = \frac{G_h}{G_0} \tag{D.2}$$

The solar constant G_{sc}, is the energy transmitted from the Sun per unit time, received on a unit area of surface, which is normal to the direct radiation at mean Earth-Sun distance $(1.495 \times 10^{11}m)$ outside of the Earth's atmosphere. A value of 1367 W/m^2 (4921.2 KJ/hm^2) for the mean solar constant is adopted in this project. While the variation of the Earth-Sun distance leads to variation of extraterrestrial radiation flux in the range of $\pm 3\%$. Thus the extraterrestrial radiation is modified

into

$$G_{vsc} = G_{sc}\left(1 + 0.033\cos\frac{360°n}{365}\right) \tag{D.3}$$

where n is the day of the year given for each month in Table A.1.

Therefore the extraterrestrial radiation on a horizontal surface at any given position between sunrise and sunset on the day n of the year is given by

$$
\begin{aligned}
G_0 &= G_{sc}\left(1 + 0.033\cos\frac{360°n}{365}\right)\cos\theta_z \\
&= G_{sc}\left(1 + 0.033\cos\frac{360°n}{365}\right)(\cos\phi\cos\delta\cos\omega + \sin\phi\sin\delta) \tag{D.4}
\end{aligned}
$$

Integrated daily solar radiation H_0 is used in this project, which is obtained by integrating Equation D.4 over the period from sunrise to sunset. If G_{sc} is in kilo joules per hour per square meter, H_0 in kilo joules per square meter is

$$
\begin{aligned}
H_0 &= \frac{24}{\pi}G_{sc}\left(1 + 0.033\cos\frac{360°n}{365}\right) \\
&\quad \times\left(\cos\phi\cos\delta\sin\omega_s + \frac{\pi\omega_s}{180}\sin\phi\sin\delta\right) \tag{D.5}
\end{aligned}
$$

where ω_s is the sunset hour angle, in degrees.

Assuming diffuse and reflected radiation to be isotropic, R can be described as (Liu and Jordan, 1962)

$$R = \left(1 - \frac{D_h}{G_h}\right)R_b + \frac{D_h}{G_h}\frac{(1 + \cos s)}{2} + \rho\frac{(1 - \cos s)}{2} \tag{D.6}$$

where D_h is diffuse radiation, ρ is in the range from 0.2 to 0.7 depending on the extent of snow cover (Liu and Jordan, 1960), R_b depends on the atmospheric cloudiness, water vapour and particulate concentration. While it can be estimated to be the ratio of direct (or extraterrestrial) radiation on tilted surface to that on horizontal

surface. In northern hemisphere and when $\gamma = 0$, it can be expressed by

$$
\begin{aligned}
R_b &= \frac{B_s}{B_h} = \frac{B_n \cos\theta}{B_n \cos\theta_z} = \frac{\cos\theta}{\cos\theta_z} \\
&= \frac{\cos(\phi - s)\cos\delta\cos\omega + \sin(\phi - s)\sin\delta}{\cos\phi\cos\delta\cos\omega + \sin\phi\sin\delta}
\end{aligned}
\tag{D.7}
$$

Therefore the daily R_b is given by

$$
R_{b,day} = \frac{\cos(\phi - s)\cos\delta\sin\omega'_s + \pi/180\,\omega'_s \sin(\phi - s)\sin\delta}{\cos\phi\cos\delta\sin\omega_s + \pi/180 \sin\phi\sin\delta}
\tag{D.8}
$$

where ω'_s is the sunset hour angle for the tilted surface which is given by

$$
\omega'_s = \min[\omega_s, \arccos[-\tan(\phi - s)\tan\delta]]
\tag{D.9}
$$

Appendix E

Publications

Three-dimensional SOlar RAdiation Model (SORAM) and its application to 3-D urban planning

Róbert Erdélyi [a], Yimin Wang [a,*], Weisi Guo [b], Edward Hanna [c], Giuseppe Colantuono [d]

[a] Solar Physics and Space Plasma Research Centre (SP2RC), School of Mathematics and Statistics, University of Sheffield, Sheffield S3 7RH, UK
[b] School of Engineering, University of Warwick, Coventry CV4 7AL, UK
[c] Department of Geography, University of Sheffield, Sheffield S10 2TN, UK
[d] The Sheffield Solar Farm, Department of Physics and Astronomy, University of Sheffield, Sheffield S3 7RH, UK

Communicated by Associate Editor: Frank Vignola

Abstract

The aim of this work is to evaluate the potential direct and diffuse solar radiation aggregated at a point location in an urban area. With the three-dimensional (3D) SOlar RAdiation Model (SORAM) presented here, the paper makes three key contributions. Firstly, the model augments the Perez et al. (1990) model by accounting for the aggregated contribution of diffuse radiation using ray-tracing methods. Secondly, the model demonstrates the use of a randomly generated city building distribution and terrain map to simulate the 3D urban solar radiation exposure at any time or over a selected time period. Thirdly, we validate our results using empirical sunlight data measured from a real urban area (Sheffield Solar Farm), and also validate our results against the Perez et al. (1990) model under conditions of no shading.
© 2013 Elsevier Ltd. All rights reserved.

Keywords: 3D; Shading condition; Solar radiation

1. Introduction

Solar radiation models are used to estimate how much solar irradiance can be collected at a location on the Earth's surface. Most existing models typically do not take into account the effects caused by urban shading (i.e. shadows cast by buildings, trees and other obstacles). The global radiation received on a point over a given time period is composed of direct radiation (i.e. that part which emanates directly from the Sun), diffuse radiation (the other part that is scattered by the Earth's atmosphere) and reflected radiation (reflected by obstacles surrounding the location). In most cases, the reflected radiation is negligible (HEMI, 2000) and is therefore ignored here.

1.1. Motivation

A sustainable city needs to generate a large fraction of its energy consumption using renewable energy sources. Large-scale photovoltaic (PV) solar-energy installations are seen as a potential solution for future cities (Hofierka and Kanuk, 2009). Grid-connected PV systems can aid peak shaving, minimize transmission and distribution losses and increase grid capacity since they generate electricity close to, or even at the consumers' point of use. Especially in great commercial areas, daytime peak load profiles are consistent with solar generation profiles (da Silva Jardim et al., 2008). Accurate local-scale

---

* Corresponding author. Address: Solar Physics and Space Plasma Research Centre (SP2RC), School of Mathematics and Statistics, University of Sheffield, F27 Hicks Building, Hounsfield Rd, Sheffield S3 7RH, UK. Tel.: +44 (0)7734803865.
E-mail address: yimin.wang@sheffield.ac.uk (Y. Wang).

(e.g. city-wide) models of both the spatial and temporal distributions of solar radiation are needed. The aim of this paper is to provide a working model for estimating the total solar energy received at a point on a sloping PV cell surface, particularly those that are subject to intermittent shading from urban terrain. The model we develop is a key enabler for the efficient deployment of PV panels at both the street level and on the walls of buildings. In order for a sustainable city or householder to determine the position, size, optimised slope and azimuth angles of PV installations, this model can be implemented to display the solar radiation distribution for each point on a surface (e.g. roof, walls and ground etc.) of a city or house. Moreover, this model can solve the problem raised in Fartaria and Pereira (2013), which is how to calculate shadow losses caused by 2-axis moving PV module trackers in PV collector fields.

1.2. Review

In the literature several solar-radiation software tools and models have been established. The most widely used software tools are the ArcGIS Solar Analyst (ArcGIS, 2012), the GRASS GIS r.sun (Suri and Hofierka, 2004; Hofierka and Zlocha, 2012), the PVSYST (PVsyst 6 Help, 2013) and PV*Sol (2013). The main drawback of the ArcGIS Solar Analyst is that by using stereographic projection, the whole sky is projected as a flat circle, with inevitable geometric inaccuracies due to the spatial distortion during the translation from 3D to 2D. The description of the methodology of the GRASS GIS r.sun can be found in the article by Suri and Hofierka (2004) with further extension from 2D to 3D version in Hofierka and Zlocha (2012). GRASS GIS r.sun and PVSYST assume an isotropic sky for diffuse radiation. Although this simplification is easy to use, it is imprecise and several anisotropic sky models have been shown to be more accurate (Muneer, 2004). PV*Sol is designed for the calculation of shadows cast only by static obstacles (Fartaria and Pereira, 2013).

There are other models and algorithms used to calculate shading losses like Perpinan (2012); Navarte and Lorenzo (2008) and Lorenzo et al. (2011), which compute shadow shapes with dimensions for each position of the Sun, followed by a calculation of multiple shadows' joint effect. This method is usually complicated as the intersection of the shadows is too complex to calculate and can lead to errors when simplifications are made (Fartaria and Pereira, 2013). Similarly, Fartaria and Pereira (2013) computes shadow losses caused by 2-axis moving PV module trackers. Their paper considers the shaded fraction of the PV array area affected by the shading. This method is precise when considering only PV collector fields that are obstructed by simple regular geometric shapes, but can not adequately cope with complex or combined shapes that are found in urban areas.

In other literature, Melo et al. (2013) and Redweik et al. (2013) also estimate shadow losses at PV surfaces, but when calculating diffuse radiation by using diffuse shading

factor in Melo et al. (2013) or the sky view factor in Redweik et al. (2013), they do not consider the angle of incidence of solar energy contribution from each sky segment. Under the diffuse radiation framework employed in Melo et al. (2013) and Redweik et al. (2013), provided that all the obstacle dimensions are the same, their orientation with respect to the PV cell is not important. Our work improves on this by attempting to refine the Perez et al. (1990) model, enabling it to calculate the angle of incidence for each diffuse ray.

Alternative methods, such as that adopted by Orioli and Gangi (2012), use photographs taken on site to determine the level of shadowing. However, this is not efficient for real-time planning at the city scale. Similarly, the software SOLCEL (Yoo, 2011) is efficient for evaluating a shading/sunlit area on a solar cell module. However, SOLCEL uses the method from Quaschning and Hanitsch (1998) to calculate the shaded area on a PV module, which requires a survey of the surroundings using optical instruments, such as fisheye camera. This method is only valid for one observer point (Quaschning and Hanitsch, 1998). Therefore, SOLCEL is not applicable for large PV systems planning like the city scale. The Nguyen and Joshua algorithm (2012) is based on 2.5D raster data, which limits consideration to roofs but not walls or the reflected component of global radiation. However, Redweik et al. (2013) found the solar radiation incident on the walls is lower than that on the roofs, but due to their large collective area, walls are a significant part of the solar-energy potential in urban areas.

1.3. Contribution

In the first part of this paper, we present a 3D SOlar RAdiation Model (SORAM) that builds on the improved Perez et al. (1990) model, the Reindl et al. (1990) model and Sun–Earth trigonometric relationship models from Duffie and Beckman (1980), and also uses a ray-tracing method (Shirley et al., 2005; Mena-Chalco, 2010), which is not subject to the above limitations. SORAM divides the sky into a large number (typically thousands) of uniformly-spaced sectors. This is in contrast with the well-known Perez et al. (1990) model which calculates the contribution of diffuse radiation from three different regions of the sky (horizon band, circum-solar and the rest of the sky), and has previously been shown to perform well in model inter-comparison studies (Muneer, 2004; Noorian et al., 2008). The first modeling novelty is that we combine a ray-tracing method (Shirley et al., 2005; Mena-Chalco, 2010) with the adjusted Perez et al. (1990) model to determine whether a solar ray (direct or diffuse), can reach a PV cell location in the 3D terrain map. The angle of incidence of each solar ray is taken into account since for a sloping surface, each solar ray from the sky contributes different amounts of solar energy.

In SORAM, we also utilize the model developed by Reindl et al. (1990) to split measured values of hourly global radiation into its direct and diffuse components.

The data thus derived are then corrected for the inclined plane of the PV cell by taking into account geometry (i.e. solar altitude, solar azimuth, and azimuth and elevation of the PV cell), as well as the shadows projected by surrounding objects. By aggregating the direct and diffuse radiation from all the points taking into account the angles of incidence in the sky that are not obstructed by obstacles, SORAM can accurately obtain the tilted global radiation received by a sloping PV cell over any period of time, from 1 h to one year. We validate our results both against the well-known Perez et al. (1990) model without terrain obstacles, and against the global radiation measured by the sensors surrounded by real urban obstacles (Sheffield Solar Farm, 2013).

Different from GRASS GIS r.sun and PVSYST, SORAM calculates solar radiation receipt based on an anisotropic sky. Also, unlike Melo et al. (2013) and Redweik et al. (2013), SORAM takes into account the angle of incidence of each sky segment by deducing the solar-energy contribution for each segment separately, based on the Perez et al. (1990) model for the calculation of diffuse radiation.

SORAM also has several ways of enabling greater future scalability than the other software tools and models mentioned above. The first advantage is because the segment of the sky in SORAM is modular. Therefore, in order to increase modeling accuracy of the anisotropic nature of diffuse radiation, SORAM can be easily scaled to incorporate a more sophisticated method and/or increase the spatial resolution of sky segment. The second advantage of SORAM is that because it uses the angle of incidence from the Sun to a point on a PV cell for each solar (direct and diffuse) ray, it can be used to calculate the solar radiation received by various shapes of panel element such as a cylinder (which is already used in the solar PV industry) and is not limited to just a flat plane surface (McIntosh et al., 2007; Colantuono et al., 2013); in other words, various models of solar concentrators can be embedded into SORAM to operate a comprehensive optimization analysis. However, here, for simplification and because it is widely employed in industry, we just use a flat plane surface in our analysis. The third advantage of SORAM is that since a 2-axis PV tracker moves according to the position of the Sun, meaning that the tracker's coordinates are available, SORAM can easily calculate shading losses resulting from other trackers in the PV collector field.

It is also worth noting that in the field of radio-communications (Boithais, 1987), a number of tools have been developed which predict the propagation of electromagnetic waves (Atoll, 2013). Despite the common electromagnetic nature of radio-communication waves and sun rays, there are some fundamental differences when considering propagation:

1. Propagation path: radio waves are emitted from devices on Earth's surface, whereas sun rays come from a single source in the sky and are parallel. Therefore, radio wave propagation deals mainly with how waves reflect and penetrate structures, whereas solar ray propagation is affected by atmospheric effects as well as how rays intersect ground-level obstacles.
2. Frequency: radio wave propagation ($\sim 10^9$ Hz) can be treated as a wave model, whereas visible solar ray propagation ($\sim 10^{15}$ Hz) is treated as a ray model.

Therefore, the contribution of this paper overlaps to a certain extent with radio-wave propagation research, but is fundamentally different in the aforementioned areas. The common aspects may be important for radio-wave flux estimates in an urban environment.

2. The 3D urban environment

This section describes the 3D urban environment used to demonstrate our proposed methodology. The solar position data in terms of hourly solar altitude, solar azimuth, angle of incidence on a PV cell's surface, and daily solar duration are computed by SORAM based on models found in Duffie and Beckman (1980). Fig. 1 outlines the overall structure of the model flowchart that underpins this body of work. In this figure, the solar altitude, solar azimuth, solar duration and angle of incidence are derived using the solar geometry algorithm summarized in Fig. 2. The parameters marked as "daily" are daily values, otherwise they are hourly values. All parameters are calculated at an hourly temporal resolution.

2.1. Direct and diffuse radiation

For each day, the sunrise time is determined and solar radiation data from that point onwards are integrated until sunset. This is to avoid unnecessary calculations for the night-time hours, to save computation time. Horizontal direct and diffuse radiation data are required to estimate global radiation on a PV cell of a given slope and azimuth. Global solar radiation received by a PV cell can be decomposed into direct and diffuse components. Although horizontal global radiation data are commonly available, horizontal direct and diffuse radiation are scarcely measured variables because of costs; therefore, the widely used model developed by Reindl et al. (1990) is embedded into SORAM to predict hourly direct and diffuse radiation from hourly global radiation on a horizontal PV cell.

Sections 3 and 4 outline the algorithm that estimates direct and diffuse radiation on a PV cell of given slope and azimuth from their counterparts on a horizontal PV cell considering surrounding shading conditions. In SORAM, for visualization and demonstration, a PV cell can be represented by an arbitrary area, which is taken to be a triangle in this particular paper. As shown in Fig. 3, the plan and portrait view of a PV cell are represented by a triangle in a hypothetical city in SORAM. The red dots on the PV cell represent the diffuse rays with
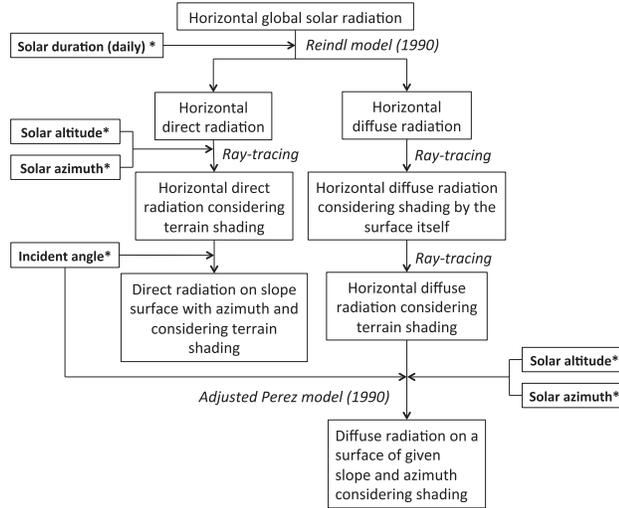
Fig. 1. Flowchart of SORAM. Solar altitude, solar azimuth, solar duration and angle of incidence are derived from the process summarized in Fig. 2. The parameters marked as "daily" are daily values, otherwise hourly values.

their angles of incidence smaller than 0° or greater than 90°.

The angle of incidence of each solar ray is calculated using a solar geometry sub-function, and the resulting flowchart is shown in Fig. 2. The angle of incidence at a given time is assumed constant for the whole map area. The parameters defining the position of the Sun in the sky are calculated on a daily or hourly basis; a list of them can be found in Table 1. For more details, see Duffie and Beckman (1980).

2.2. Shading algorithm

In order to simulate a random urban setting, a number of obstacles (buildings/trees) are incorporated with stochastic width, length and height dimensions, with boundaries of $[1, 10]$, $[1, 10]$ and $[1, 50]$ m respectively (i.e. these values are randomly varied in 1-m increments within these ranges). The aim of using these boundaries is to obtain a realistic representation of the city and solar radiation distribution for visualization. When we incorporate a real urban plan into SORAM, these hypothetical boundaries are no longer necessary. In this work, trees are considered as solid obstacles and their solar energy potential is not considered. The dimension for each building/tree is described by using its two-set cartesian coordinates in this 3D environment, i.e. (x, y, z) and $(x + \text{width}, y + \text{length}, z + \text{height})$. These random obstacles are also randomly placed on a 100×100 m^2 map showing their distribution. Results are sampled at a 1×1 m spatial resolution on this map. Solar altitude varies between $[0°, 90°]$, and the solar azimuth angle ranges between $-180°$ and $180°$ with 0° due south, where east is negative and west is positive.

The time-step size depends on the resolution at which solar radiation is observed. Hourly temporal resolution is sufficient for most applications (Hofierka and Zlocha, 2012), and is consequently adopted in this work.

Ray-tracing (Shirley et al., 2005; Mena-Chalco, 2010) is used in this work to determine if a solar ray is shaded by an obstacle. Shirley et al. (2005) considered an intersection between a 2D ray vector and a rectangle, which can be generalized to between a arbitrary 3D ray and a voxel. Mena-Chalco (2010) implemented the ray-tracing algorithm for detecting if a 3D ray vector intersects with a box (voxel). In our ray-tracing algorithm, contrary to real

Fig. 2. Flowchart of the solar geometry calculation used to derive solar altitude, solar azimuth, solar duration and angle of incidence. The parameters marked as "daily" are daily values, otherwise hourly values.

Fig. 3. The red dots on the PV cell represent the diffuse rays with $\theta_d \leqslant 0°$ or $\theta_d \geqslant 90°$. (a) Plan view of a PV cell represented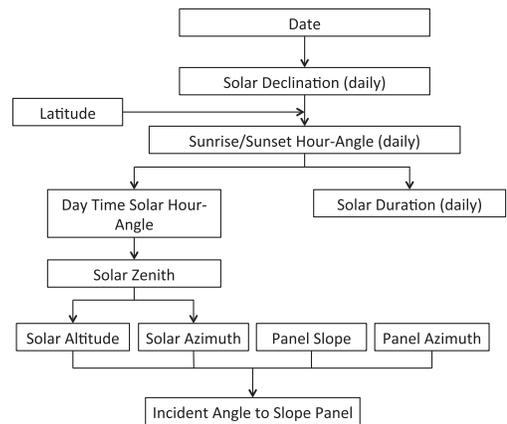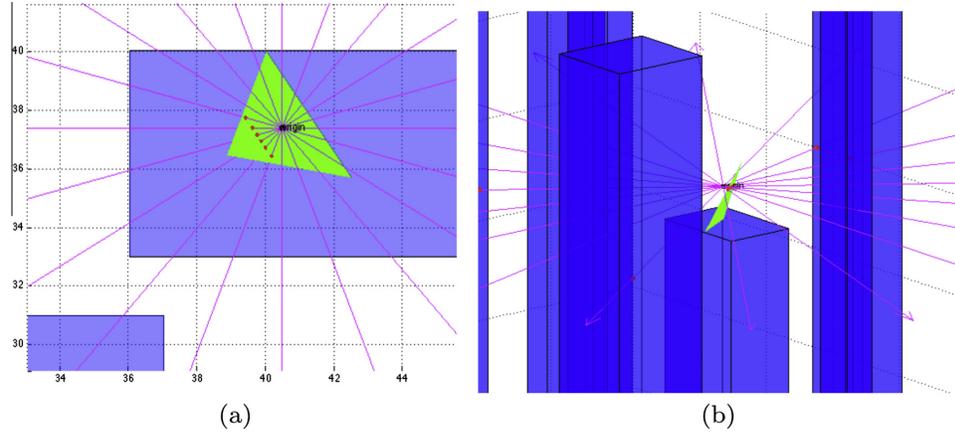 by a triangle in a hypothetical city in SORAM; (b) portrait view of (a). (For interpretation of the references to colour in this figure legend, the reader is referred to the web version of this article.)

Table 1
Nomenclature used in this paper.

Parameter name	Parameter	Range
Angle of incidence from direct radiation	θ	0–90°
Angle of incidence from diffuse radiation	θ_d	0–90°
Solar altitude	α_s	0–90°
Solar azimuth	γ_s	−180° to 180°
Diffuse-ray altitude	α_d	0–90°
Diffuse-ray azimuth	γ_d	−180° to 180°
Surface slope angle	s	0–90°
Surface azimuth angle	γ	−180° to 180°
Horizontal direct radiation	B_h	0–∞
Slope direct radiation	B_s	0–∞
Horizontal diffuse radiation	D_h	0–∞
Slope diffuse radiation	D_s	0–∞
Diffuse radiation (main)	T_m	0–∞
Diffuse radiation (horizon)	T_h	0–∞
Number of solar ray (main)	n_m	0–∞
Number of solar ray (horizon)	n_h	0–∞
Diffuse radiation contribution coefficient (main)	1	1
Diffuse radiation contribution coefficient (circum-solar)	F_1	0–∞
Diffuse radiation contribution coefficient (horizon)	F_2	0–∞

conditions, a PV cell (i.e. a tested point in the 3D urban environment) is regarded as a source emitting rays to the sky segments. The position of the 3D ray vector on the 3D urban environment is determined by the cartesian coordinates of the tested point; the direction of the 3D ray vector is represented by the hourly altitude (α) and azimuth (γ) of direct/diffuse radiation rays, i.e. $(\sin(\gamma_s), \cos(\gamma_s), \tan(\alpha_s))$ or $(\sin(\gamma_d), \cos(\gamma_d), \tan(\alpha_d))$. The subscripts s means direct

solar radiation, and d means diffuse solar radiation. The ray-tracing method is then used between the 3D ray vector and each obstacle. Once a intersection is detected, the distance between the PV cell and the intersection is calculated. A positive distance means the intersection is between the PV cell and the sky, otherwise a negative distance represents an invalid intersection and is discarded.

3. Direct radiation

To predict the tilted direct radiation, a point for mounting a PV panel in SORAM is chosen, called the *origin*. Hourly direct radiation is treated as a ray emanating from the Sun towards of the *origin*. θ is the angle of incidence, i.e. the angle between the direct radiation on a PV cell surface and the normal to that surface.

If $\theta < 0°$ or $\theta \geqslant 90°$, hourly amount of direct radiation associated with the solar ray is excluded from the integration, i.e. $B_s = 0$. Whereas, if $0° \leqslant \theta < 90°$, the ray-tracing algorithm is used to determine whether the direct ray intersects with buildings that are taller than the vertical height of the *origin*. If there is an intersection, $B_s = 0$; if the direct ray is not obstructed by any building, the tilted hourly direct radiation can be estimated by:

$$B_s = B_h \frac{a_0}{a_1},$$
$$a_0 = \max(0, \cos(\theta)), \qquad (1)$$
$$a_1 = \max\left(\cos(85°), \cos\left(\frac{\pi}{2} - \alpha_s\right)\right).$$

where B_s and B_h are the hourly direct radiation on a sloping and horizontal PV cell, respectively, α_s is the solar altitude angle. For more details of these variables, see Duffie and Beckman (1980).

4. Diffuse radiation

In this section, we describe how SORAM converts diffuse radiation from horizontal surface to the sloping one while taking shading into account. As previously mentioned, the Perez et al. (1990) model has demonstrated strong agreement with empirical data. In SORAM, the Perez et al. (1990) model is further developed to take shading due to obstacles into account.

4.1. Augmenting Perez et al. model with ray-tracing

It is observed that, in the atmosphere, there are two main zones causing the anisotropic nature of diffuse radiation: (i) circumsolar brightening resulting from forward scattering by aerosols, and (ii) horizon brightening mostly caused by multiple Rayleigh scattering and retro-scattering in a clear atmosphere (Kano, 1964). In the Perez et al. (1990) model, the circumsolar disk and horizon band are superimposed on the sky hemisphere, creating three distinct isotropic zones (Perez et al., 1987).

In the model proposed by Perez et al. (1990), for simplicity it is assumed that all circumsolar energy is emitted from a point centred on the Sun's position, and the horizon band originates from an arc of a great circle at the base of the atmosphere. The horizon band in SORAM is a great circle that is at the same height as the *origin*, and because it is naturally level with the *origin*, it has no effect on a horizontal PV cell centred on the *origin*.

Without any terrain shading, the relationship between diffuse radiation on a sloping PV cell and a horizontal one may be written as (Perez et al., 1987, 1990):

$$D_s = D_h \left[(1 - F_1) \frac{1 + \cos(s)}{2} + F_1 \frac{a_0}{a_1} + F_2 \sin(s) \right]. \quad (2)$$

where D_s and D_h are the hourly diffuse radiation on a sloping and horizontal PV cell, respectively, a_0 and a_1 have the same definition as in Eqs. 1, s is the slope angle of a PV cell, F_1 and F_2 are the diffuse radiation contribution coefficients for the circumsolar and horizon zones, respectively. They are normalised by the diffuse radiation contribution coefficient for the main zone. Therefore, $(1 - F_1)$ is the ratio of diffuse radiation on a horizontal PV cell from the main zone to the whole sky.

Because of the homogeneity of the three aforementioned sky zones, applying the Perez et al. (1990) model to SORAM and assuming the total diffuse radiation from the main zone is T_m, the number of those diffuse rays is n_m, we note that:

$$1 - F_1 = \int_{-\pi}^{\pi} \int_0^{\frac{\pi}{2}} \frac{T_m}{n_m} \sin(\alpha_d) \, d\alpha_d d\gamma_d, \quad (3)$$

where α_d and γ_d are the altitude and azimuth angles for each diffuse ray, respectively. Thus, the diffuse radiation contribution of each ray in the sky is,

$$\frac{T_m}{n_m} = \frac{1 - F_1}{\int_{-\pi}^{\pi} \int_0^{\frac{\pi}{2}} \sin(\alpha_d) \, d\alpha_d d\gamma_d},$$
$$= \frac{1 - F_1}{2\pi}, \quad (4)$$

Moreover, the angle of incidence of a diffuse ray is

$$\cos(\theta_d) = \cos\left(\frac{\pi}{2} - \alpha_d\right) \cos(s),$$
$$+ \sin\left(\frac{\pi}{2} - \alpha_d\right) \sin(s) \cos(\gamma_d - \gamma), \quad (5)$$

where γ is the azimuth angle of a PV cell.

Therefore, without any terrain shading, the diffuse radiation from the main zone both on the front and back of a sloping PV cell is,

$$\int \frac{T_m}{n_m} \cos(\theta_d) \, d\theta_d, = \frac{1 - F_1}{2\pi} \cos(s) \int_{-\pi}^{\pi} \int_0^{\frac{\pi}{2}} \sin(\alpha_d) \, d\alpha_d d\gamma_d,$$
$$= (1 - F_1) \cos(s). \quad (6)$$

This part of the diffuse radiation contribution is for the whole main zone of the sky. This means when a diffuse ray comes from back of a PV cell ($\theta < 0°$ or $\theta > 90°$), a negative value contributes to this integration, which should be zero. Thus, the diffuse radiation contribution shaded by a PV cell needs to be added, which is,

$$(1 - F_1) \frac{1 - \cos(s)}{2}. \quad (7)$$

Therefore in reality, when there is no terrain shading, the diffuse radiation from the main zone on a sloping PV cell is,

$$(1 - F_1) \cos(s) + (1 - F_1) \frac{1 - \cos(s)}{2},$$
$$= (1 - F_1) \frac{\cos(s) + 1}{2}. \quad (8)$$

which satisfies Perez et al. (1987), Perez et al. (1990) as shown in Eq. 2. Note that in SORAM, the part of diffuse radiation contribution comes from back of a PV cell is detected and set to be zero.

Similar to the direct radiation, the conversion of horizontal to inclined diffuse radiation from the circumsolar zone is,

$$F_1 \frac{a_0}{a_1}. \quad (9)$$

Assuming the total diffuse radiation from the horizon zone is T_h and the number of those diffuse rays is n_h, we have:

$$F_2 \sin(s) = \int \frac{T_h}{n_h} \cos(\theta_d) \, d\theta_d,$$
$$= \frac{T_m}{n_m} \int_{\gamma - \frac{\pi}{2}}^{\gamma + \frac{\pi}{2}} \sin(s) \cos(\gamma_d - \gamma) \, d\gamma_d, \quad (10)$$

Thus,

$$\frac{T_h}{n_h} = \frac{F_2}{\int_{\gamma-\frac{\pi}{2}}^{\gamma+\frac{\pi}{2}} \cos(\gamma_d - \gamma)\,d\gamma_d}. \tag{11}$$

To sum up, for each diffuse ray in the main, circumsolar and horizon zone, the energy contributions are

$$\frac{1 - F_1}{\int_{-\pi}^{\pi} \int_0^{\frac{\pi}{2}} \sin(\alpha_d)\,d\alpha_d d\gamma_d} \cos(\theta_d), \tag{12}$$

$$F_1 \frac{a_0}{a_1}, \tag{13}$$

$$\frac{F_2}{\int_{\gamma-\frac{\pi}{2}}^{\gamma+\frac{\pi}{2}} \cos(\gamma_d - \gamma)\,d\gamma_d} \cos(\theta_d). \tag{14}$$

4.2. Shading from slope surface and terrain

Figs. 3 and 4 show an arbitrary example where the triangle represents a PV cell with a slope of 50° and an azimuth angle 60° southwest facing in SORAM. A half sphere with altitude $\alpha_d \in [0°, 90°]$ and azimuth $\gamma_d \in [-180°, 180°]$, respectively, is centred on the *origin*. Vectors in Fig. 3 and 4 represent twenty diffuse rays ($\alpha_d = 0°$).

Let the number of vectors when $\alpha_d = 0°$ be N. To guarantee the uniform representation of the sky, the number of vectors for any elevation should be $N \cos(\alpha_d)$. It is worth noting that as the slope angle increases, the number of independent vectors converges to one.

There are two kinds of shading: one results from the sloping PV cell itself, and the other is from surrounding obstacles including buildings. If $\theta_d < 0°$ or $\theta_d \geqslant 90°, D_s = 0$. Whereas, if $0° \leqslant \theta_d < 90°$, ray-tracing algorithm is used to determine whether or not the diffuse ray intersects with buildings. If there is an intersection, $D_s = 0$; otherwise, if a diffuse ray emanates from the main, the circumsolar or the horizon zone, this ray's energy is given by Eqs. 12,13 or 14, respectively, and is therefore integrated to the diffuse portion, see Fig. 4.

Finally, when all diffuse rays are aggregated, the diffuse portion is multiplied by the hourly observed horizontal diffuse radiation to obtain the tilted diffuse radiation. This is then added to the direct radiation calculated from Section 3 at the same time-step to obtain the tilted global radiation.

5. Results and evaluation

5.1. Hypothetic results

Integrating results from the above calculations for a certain time period for each point on the map, a contour plot is constructed, as shown in Fig. 5. Fig. 5a shows stacked contours for a sequence of height levels spaced by 20 m, in each case considering shading from the hypothetical distribution of buildings. Next, Fig. 5b with its chosable parameters (height, slope and azimuth) displays the solar radiation distribution on the ground due to shading with its chosable parameters.

SORAM can also deduce the optimised slope and azimuth angle for any selected location in a city. This is accomplished by repeatedly running SORAM for a given range of slope and azimuth angles.

5.2. Evaluation of SORAM

The Sheffield Solar Farm (SSF) is part of Project Sunshine operating at the University of Sheffield, UK, allowing real-world testing of photovoltaics. Nine months of hourly global radiation data were collected by the SSF with two different pyranometers at a 12.7° tilt, 45° southeast facing and 45° southwest facing, respectively. Fig. 6a shows a Google Maps image of the Hicks Building at the University of Sheffield, UK and the resulting map in SORAM. The green triangle represents the position of the pyranometer from the Sheffield Solar Farm. Fig. 6b and c show a graphical sketch of how SORAM takes obstacles into account when determining the amount of diffuse radiation reaching the pyranometer. The blue lines represent the edges of surrounding buildings that can cast shadows on the green triangle representing the pyranometer position. The magenta vectors in Fig. 6b and c indicate the part of diffuse radiation when the slope angle of the pyranometer (green triangle) is 12.7°, and the actual stepsize of azimuth used in SORAM is one-tenth or smaller than shown in this figure. Fig. 7 shows the global radiation distribution over the sampled area around Hicks building. The blue lines in Fig. 7a and b depict the edges of buildings of the sampled area based on a Google Map and SORAM. All the obstacles such as buildings and trees are approximated by voxels. Fig. 7c displays the 3D simulation of global radiation distribution at heights of 0 m and 11.3 m over area defined in Fig. 7a and b, based on SORAM and accounting for the various buildings present.

The performance output of SORAM is shown in Tables 2 and 3. The evaluation includes the mean bias error (MBE), given by

$$\text{MBE} = \frac{\sum_n (\text{model}_i - \text{measured}_i)}{n}, \tag{15}$$

where n is the number of data points and i denotes a given event, and root mean square error (RMSE),

$$\text{RMSE} = \left\{ \frac{\sum_n (\text{model}_i - \text{measured}_i)^2}{n} \right\}^{0.5}. \tag{16}$$

Experiments about the step sizes of α_d and γ_d have been done in SORAM, i.e. resolution of the segment of the diffuse radiation from the sky. The differences of MBE and RMSE between experiments should be smaller than 1%, because 1% increase/decrease is very important in PV industry. Without any terrain shading, the MBE and RMSE are calculated in the way that SORAM produces the modelled data, and the output from Perez et al.
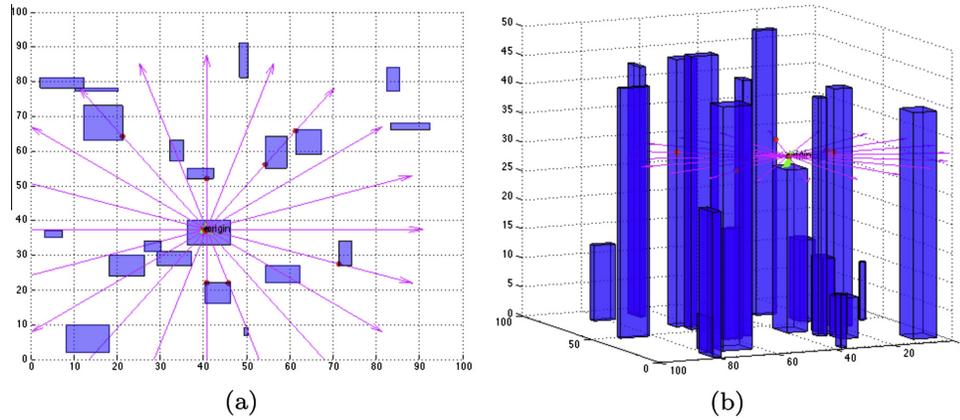
Fig. 4. The red dots on buildings mean the diffuse ray intersect a building and are therefore not collected by the PV cell; while the red dots on the PV cell represent the diffuse rays with $\theta_d \leqslant 0°$ or $\theta_d \geqslant 90°$. (a) Plan view of a hypothetical city in SORAM; (b) portrait view. (For interpretation of the references to colour in this figure legend, the reader is referred to the web version of this article.)
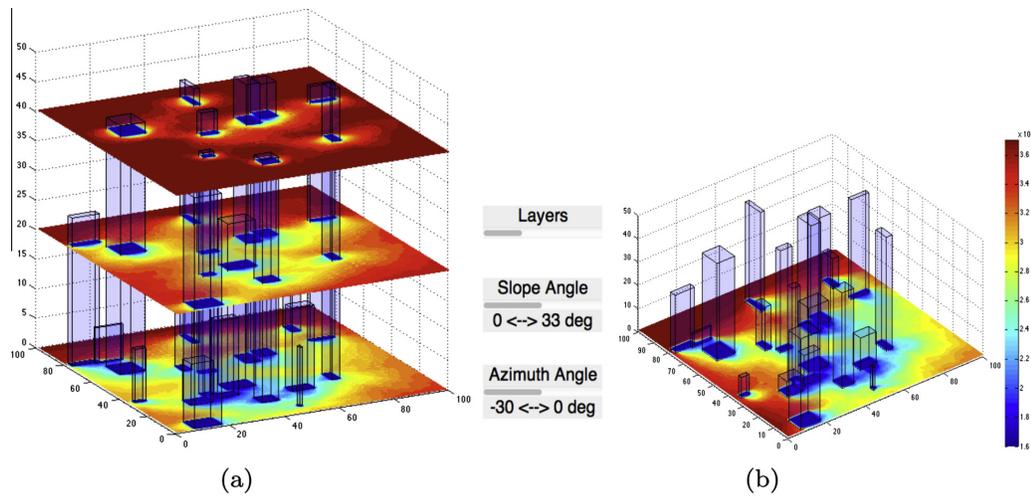
Fig. 5. Solar radiation distribution in the hypothetical city introduced in Fig. 4 computed by SORAM: (a) contours on various heights; and (b) contours with chosable parameters: height, slope and azimuth angles of PV cells.

(1990) model is treated as the measured data. In this case, the maximum step size of α_d and γ_d is 6°. Under terrain shading, SORAM with various step sizes produces the modelled data, and SSF gives the measured data. In this case, the maximum step size of α_d and γ_d is 2°. These experiments were done with 1° increment, and start from 1° for the step sizes of α_d and γ_d due to computer limitation and time.

In Table 2, SORAM outputs the modelled data, and the data from the Perez et al. (1990) model is treated as the measured data. The performance is evaluated using the ratio of sloping diffuse radiation to horizontal diffuse radiation: this step is to check if the improved diffuse model in

SORAM matches the Perez et al. (1990) model. This table shows a $-3.6 \times 10^{-3}\%$ underestimation of SORAM against the Perez et al. (1990) model, and the RMSE is $3.4 \times 10^{-2}\%$. In order to evaluate how consistent SORAM is with the Perez et al. (1990) model, the step size of α_d and γ_d of 1° is used. These results indicate that the formulae deduced in Section 4 are consistent with the Perez et al. (1990) model.

Similarly, Table 3 shows the comparison between SORAM and the observed SSF data, and, between the Perez et al. (1990) model and the observed SSF data. The performance is evaluated using the global irradiance since this step is to validate SORAM. The "SORAM" shown

Fig. 6. (a) GoogleMap's image of the Hicks Building at the University of Sheffield, UK; the green triangle represents a PV cell (i.e. the position of the pyranometer from the Sheffield Solar Farm); (b), (c) A graphical sketch of how SORAM takes obstacles into account when determining the amount of diffuse radiation reaching the PV cell. (For interpretation of the references to colour in this figure legend, the reader is referred to the web version of this article.)
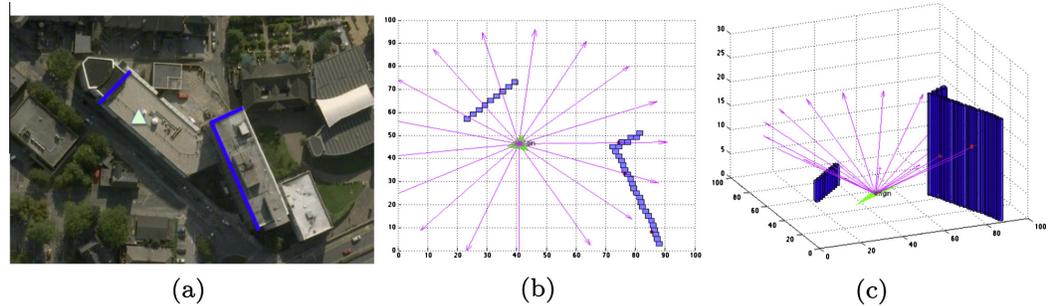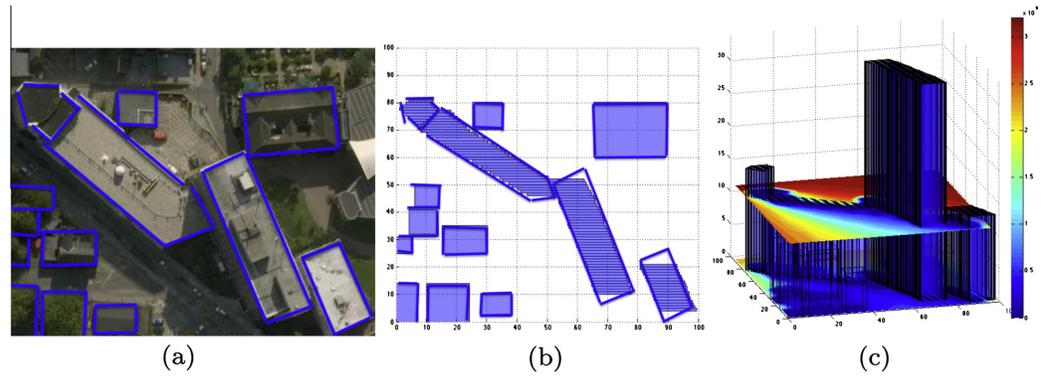

Fig. 7. (a) GoogleMap image of Hicks Building and its immediate surroundings at the University of Sheffield, UK; (b) plan view of (a); (c) 3D simulation of global radiation distribution at heights of 0 m and 11.3 m over area defined in (a) and (b), based on SORAM described in main text and accounting for the various buildings present. The blue lines in (a) and (b) depict the margins of buildings of the sampled area both from a Google Map and SORAM. All the obstacles such as buildings and trees are approximated by voxels. (For interpretation of the references to color in this figure legend, the reader is referred to the web version of this article.)

Table 2
Output performance of SORAM vs the Perez et al. (1990) model. The output is the ratio of diffuse radiation on a sloping PV cell to a horizontal one. The minus sign in MBE means the output from SORAM underestimates that from the Perez et al. (1990) model.

Orientation	Mean	MBE	RMSE
45° SE	1.1	-2.8×10^{-5}	1.9×10^{-4}
45° SW	1.0	-4.9×10^{-5}	5.3×10^{-4}
Percent error		$-3.6 \times 10^{-3}\%$	$3.4 \times 10^{-2}\%$

Table 3
Output performance of SORAM and Perez et al. models (1990) vs observed data from the Sheffield Solar Farm. The unit of mean global irradiance, MBE and RMSE is KJ m^{-2} h^{-1}. The minus sign in MBE of SORAM means the output from SORAM underestimates that from the Sheffield Solar Farm measured global radiation data.

Surface	Mean global	SORAM		Perez et al. model	
Orientation	Irradiance	MBE	RMSE	MBE	RMSE
45° SE	912.1	45.8	177.2	72.6	196.5
45° SW	794.0	−13.2	121.5	9.6	103.5
Percent error		3.3%	17.4%	4.6%	17.3%

in Table 3 depicts that SORAM ran under real shading conditions around the *origin*. In this case, SORAM gives the modelled data, and SSF gives the measured data. The shading is mainly caused by two parts of Hicks building with absolute heights (higher than the *origin*) of 21.9 m and 4.3 m respectively, as shown in Fig. 6. Note that the Perez et al. (1990) model is not able to integrate the shading effect from the surroundings. Therefore the diffuse radia-

tion produced by SORAM is smaller than the Perez et al. (1990) model due to shading (Table 3). Considering computation time, the step size of α_d and γ_d is 2° for this table.

Furthermore, SSF's horizontal global radiation has been measured under the same shading conditions (the green triangle in Fig. 6 shows the position of the SSF's

pyranometers), and used to predict the tilted direct and diffuse radiation for the tilt-orientated PV cell. However, in order to calculate solar radiation on a shaded sloping PV cell, SORAM input should be unshaded horizontal global radiation, which is not available in Sheffield. Therefore, we expected that SORAM modelled output would underestimate the solar energy. The evaluation, between the 45° SW pyranometer from SSF and SORAM modelled output under the same configuration and shadow effects as shown in SORAM in Table 3, meets the expectation whose MBE is -13.2 KJ m^{-2} h^{-1}; however, for the 45° SE case, it does not. There are at least three reasons for these errors, regardless of the overestimation or underestimation. The first reason is the complexity of the 45° SE surroundings, where only the Hicks building (main shadow) is taken into account, whereas several buildings of unknown heights that could cast shadows on the pyranometer are not included in SORAM. Secondly, the modelled solar radiation is sensitive to the positions of the pyranometer (the triangle in Fig. 6b and c) and the buildings, while the real-life map in SORAM (Fig. 6b and c) is just an approximation constructed from Google Map: thus this approximation may produce errors. Thirdly, it is believed that the largest errors are introduced by the embedded Perez et al. (1990) model, which treats the solar radiation contribution within each sky zone as uniform, and from errors in the solar-radiation measurements.

The absolute averaged MBE of SORAM with shading against the observed data is 3.3% while RMSE is 17.4%: MBE (RMSE) is smaller than (similar to) the MBE (RMSE) of 4.6% (17.3%) obtained using the Perez et al. (1990) model against measured data. Overall, SORAM shows a better and more accurate performance than the Perez et al. (1990) model.

6. Conclusion

In this paper, we propose a numerical model (SORAM) for evaluating the direct and diffuse solar radiation on a sloping PV cell in an urban environment. We believe this is a key enabler technology with great potential for the mass deployment of solar PV cells in current and future sustainable cities.

The paper makes three key contributions. First, the established Perez et al. (1990) model is combined with a ray-tracing algorithm to improve the accuracy of anisotropic diffuse radiation modeling, taking into account the angle of incidence of each solar ray. Second, dynamic 3D shading from urban obstacles (buildings/trees) is integrated into the model. Third, the model is validated using empirical measurement.

More specifically, the paper utilizes the Reindl et al. model (1990) to convert global horizontal radiation to direct and diffuse radiation. The direct radiation on a PV cell of a given slope and azimuth is determined following Duffie and Beckman (1980) and Muneer (2004), together with a ray-tracing algorithm. The Perez et al. (1990) model

is adapted with a ray-tracing algorithm, in order to transform diffuse radiation from a patch in the sky to a specific ray. The combined algorithm is then used to compute the shading effect from the urban terrain buildings. Finally, we aggregate the direct and diffuse radiation received.

SORAM without shading is validated against the Perez et al. (1990) model. A -3.6×10^{-3}% underestimation show that under conditions of no shading SORAM works as well as the Perez et al. (1990) model. SORAM with shading is evaluated against the observed SSF solar radiation data. The results show a 3.3% MBE and a 17.4% RMSE, while these values are respectively 4.6% and 17.3% when the outputs from the Perez et al. (1990) model are compared with SSF data. Therefore, SORAM overall performs better than the Perez et al. (1990) model.

The proposed model has been applied to a sample area in order to demonstrate its capabilities. Error analysis shows that SORAM can be effectively used in many applications including solar energy (PV and thermal) installations and environmentally friendly urban design. A further development of SORAM will focus on flexibility of shapes of obstacles and integrating reflected radiation by different materials such as glass and trees.

For queries about the SORAM computer code, please contact the corresponding author. For queries about the experimental data used here, please contact Dr. Alastair Buckley (alastair.buckley@sheffield.ac.uk) from the Sheffield Solar Farm (www.sheffieldsolarfarm.group.shef.ac.uk) who is the PI of SSF.

References

ArcGIS Help 10.1., 2012. [Internet]. http://resources.arcgis.com/en/help/main/10.1/index.html#/Understanding_solar_radiation_analysis/009z000000t8000000/.

Atoll, F., 2013. http://www.forsk.com/atoll/.

Boithais, L., 1987. Radio Wave Propagation. McGraw-Hill Book Company, New York.

Colantuono, G., Buckley, A., Erdelyi, R., 2013. Ray-optics modelling of rectangular and cylindrical 2-layer solar concentrators. J. Lightw. Technol. 31 (7), 1033–1044.

da Silva Jardim, C., Rther, R., Salamoni, I.T., de Souza Viana, T., Rebechi, S.H., Knob, P.J., 2008. The strategic siting and the roofing area requirements of building-integrated photovoltaic solar energy generators in urban areas in Brazil. Energy Build. 40, 365–370.

Duffie, J.A., Beckman, W.A., 1980. Solar Engineering of Thermal Processes. John Wiley & Sons, Inc., pp.13–45.

Fartaria, T.O., Pereira, M.C., 2013. Simulation and computation of shadow losses of direct normal, diffuse solar radiation and albedo in a photovoltaic field with multiple 2-axis trackers using ray tracing methods. Solar Energy 91, 93–101.

HEMI, 2000. The Solar Analyst 1.0 User Manual Draft. Helios Environmental Modeling Institute 568 (HEMI), LLC. Kansas, KS.

Hofierka, J., Kanuk, J., 2009. Assessment of photovoltaic potential in urban areas using opensource solar radiation tools. Renew. Energy 34, 2206–2214.

Hofierka, J., Zlocha, M., 2012. A new 3-D solar radiation model for 3-D city models. Trans. GIS, 2012 16 (5), 681–690.

Kano, M., 1964. Effect of a Turbid Layer on Radiation Emerging from a Planetary Atmosphere. In: Doctoral Dssertation. University of California, Los Angeles.

Lorenzo, E., Navarte, L., Munoz, J., 2011. Tracking and back-tracking. Prog. Photovolt.: Res. Appl. 19, 747–753.

Melo, E.G., Almeida, M.P., Zilles, R., Grimoni, J.A.B., 2013. Using a shading matrix to estimate the shading factor and the irradiation in a three-dimensional model of a receiving surface in an urban environment. Solar Energy 92, 15–25.

Mena-Chalco, J.P., 2010. Ray/box Intersection. http://www.mathworks.co.uk/matlabcentral/fileexchange/26834-raybox-intersection.

Muneer, T., 2004. Solar radiation and daylight models. Elsevier Butterworth-Heinemann, pp. 165..

McIntosh, K., Yamada, N., Richards, B., 2007. Theoretical comparison of cylindrical and square-planar luminescent solar concentrators. Appl. Phys. B 88, 285–290.

Navarte, L., Lorenzo, E., 2008. Tracking and ground cover ratio. Prog. Photovolt.: Res. Appl. 16, 703–714.

Noorian, A.M., Moradi, I., Kamali, G.A., 2008. Evaluation of 12 models to estimate hourly diffused irradiation on inclined surfaces. Renew. Energy 33, 1406–1412.

Orioli, A., Gangi, A.D., 2012. An improved photographic method to estimate the shading effect of obstructions. Solar Energy 86, 3470–3488.

Perez, R., Ineichen, P., Stewart, R., Menicucci, D., 1987. A new simplified version of the Perez diffuse irradiance model for tilted surfaces. Solar Energy 39 (3), 221–231.

Perez, R., Ineichen, P., Seals, R., Michalsky, J., Stewart, R., 1990. Modeling daylight availability and irradiance components from direct and global irradiance. Solar Energy 44 (5), 271–289.

Perpinan, O., 2012. Cost of energy and mutual shadow in a 2-axis tracking PV system. Renew. Energy 43, 331–342.

PV*Sol, 2013. http://www.solardesign.co.uk/pv.php.

PVSYST, 2013. PVsyst 6 Help. http://files.pvsyst.com/help/index.html.

Quaschning, V., Hanitsch, R., 1998. Irradiance calculation on shaded surfaces. Solar Energy 62 (5), 365–375.

Redweik, P., Catita, C., Brito, M., 2013. Solar energy potential on roofs and facades in an urban landscape. Solar Energy 97, 332–341.

Reindl, D.T., Beckman, W.A., Duffie, J.A., 1990. Diffuse fraction correlations. Solar Energy 45 (1), 1–7.

Sheffield Solar Farm, 2013. http://www.sheffieldsolarfarm.group.shef.ac.uk.

Shirley, P., Gleicher, M., Marschner, S.R., Reinhard, E., Sung, K., Thompson, W.B., Willemsen, P., 2005. Fundamentals of Computer Graphics. A K Peters, Ltd., pp. 218–228.

Suri, M., Hofierka, J., 2004. A new GIS-based solar radiation model and its application to photovoltaic assessments. Trans. GIS 8 (2), 175–190.

Yoo, S.H., 2011. Simulation for an optimal application of BIPV through parameter variation. Solar Energy 85, 1291–1301.

Bibliography

ArcGIS (2012). ArcGIS Help 10.1. Available from http://resources.arcgis.com/en/help/main/10.1/index.html#/Understanding_solar_radiation_analysis/009z000000t8000000/.

Atoll, F. (2013). Atoll wireless network engineering software. Available from http://www.forsk.com/atoll/.

BADC (2012). Radiation observation data – columns in the ro table. Available from http://badc.nerc.ac.uk/data/ukmo-midas/RO_Table.html.

Bard, E. and Frank, M. (2006). Climate change and solar variability: What's new under the sun? *Earth and Planetary Science Letters*, 248(1-2):1–14.

Batchelder, J. S., Zewail, A. H., and Cole, T. (1979). Luminescent solar concentrators. I: Theory of operation and techniques for performance evaluation. *Appl. Optics*, 18(18):3090–3110.

Batchelder, J. S., Zewail, A. H., and Cole, T. (1981). Luminescent Solar Concentrators. II. Experimental and Theoretical Analysis of Their Possible Efficiencies. *Appl. Optics*, 20:3733.

Benford, F. and Bock, J. E. (1939). A time analysis of sunshine. *Trans. of the American Illumination Engineering Soc.*, 34:200.

Bigg, G. R. (2003). The Oceans and Climate. *Cambridge University Press*.

Boithais, L. (1987). *Radio Wave Propagation.* McGraw-Hill Book Company, New York.

Burt, T. P. and Howden, N. J. K. (2013). North Atlantic Oscillation amplifies orographic precipitation and river flow in upland Britain. *Water Resources Research*, 49(6):3504–3515.

Canny, J. (1986). A computational approach to edge detection. pattern analysis and machine intelligence. *IEEE Transactions on, PAMI*, 8(6):679–698.

Clarke, P., Munawwar, S., Davidson, A., Muneer, T., and J, K. (2007a). Building services engineering research and technology. *BUILDING SERV ENG RES TECHNOL*, 28:189.

Clarke, P., Munawwar, S., Davidson, A., Muneer, T., and Kubie, J. (2007b). Technical note: An investigation of possible improvements in accuracy of regressions between diffuse and global solar radiation. *Bld Serv. Eng. Res. Technol.*, 28:189–197.

Colantuono, G., Buckley, A., and Erdélyi, R. (2013). Ray-Optics Modelling of Rectangular and Cylindrical 2-Layer Solar Concentrators. *Lightwave Techonology, Journal of.*, 31:1033–1044.

Colantuono, G., Wang, Y., Hanna, E., and Erdélyi, R. (2014). Signature of the North Atlantic Oscillation on British solar radiation availability and PV potential: the winter zonal seesaw. in review.

Cooper, P. I. (1969). Absorption of radiation in solar stills. *Solar Energy*, 12(3):333–345.

Cowley, J. P. (1978). The distribution over Great Britain of global solar radiation on a horizontal surface. *Met. Mag*, 107:357.

Currie, M., Mapel, J., Heidel, T., Goffri, S., and Baldo, M. (2008). High-efficiency organic solar concentrators for photovoltaics. *Science*, 321:226–228.

da Silva Jardim, C., Rther, R., Salamoni, I. T., de Souza Viana, T., Rebechi, S. H., and Knob, P. J. (2008). The strategic siting and the roofing area requirements of building-integrated photovoltaic solar energy generators in urban areas in brazil. *Energy and Buildings*, 40:365–370.

d'Almedia, G. A., Koepke, P., and Shettle, E. P. (1991). Atmospheric Aerosols: Global Climatology and Radiative Characteristics. *A. Deepak Publishing*, page 561.

Davy, R. J. and Troccoli, A. (2012). Interannual variability of solar energy generation in Australia. *Solar Energy*, 86:3554–3560.

Debije, M. and Verbunt, P. (2012). Thirty years of luminescent solar concentrator research: Solar energy for the built environment. *Adv. Energy Mater.*, 2:12–35.

Derrien, M. and LeGLeau, H. (2005). MSG/SEVIRI cloud mask and type from SAFNWC. *Int. J. Rem. Sens*, 26(21):4707–4732.

Dinccer, F. (2011). The analysis on photovoltaic electricity generation status, potential and policies of the leading countries in solar energy. *Renewable and Sustainable Energy Reviews*, 15:713–720.

Duffie, J. A. and Beckman, W. A. (1991). *Solar engineering of thermal processes.* A Wiley-Interscience Publication, 2 edition.

EEA (2007). The pan-European environment: glimpses into an uncertain future. *EEA Report*, (4):29.

Ely, C. R., Brayshaw, D. J., Methven, J., Cox, J., and Pearce, O. (2013). Implications of the North Atlantic Oscillation for a UK-Norway Renewable power system. *Energy Policy*, 62(0):1420–1427.

Erdélyi, R., Wang, Y., Guo, W., Hanna, E., and Colantuono, G. (2014). Three-dimensional SOlar RAdiation Model (SORAM) and its application to 3-D urban planning. *Solar Energy*, 101:63–73.

Fartaria, T. O. and Pereira, M. C. (2013). Simulation and computation of shadow losses of direct normal, diffuse solar radiation and albedo in a photovoltaic field with multiple 2-axis trackers using ray tracing methods. *Solar Energy*, 91:93–101.

Geyserland (2014). Geyserland observatory. Available from http://www.geyserlandobs.org/sun.html.

Goetzberger, A. and Greubel, W. (1977). Solar energy conversion with fluorescent collectors. *Appl. Phys.*, 14:123–139.

Goldschmidt, J. C., Peters, M., Bosch, A., Helmers, H., Dimroth, F., Gunz, S. W., and Willeke, G. (2009). Increasing the efficiency of fluorescent concentrator systems. *Sol. En. Mater. Sol. Cells*, 93:176–182.

Greatbatch, C. B. (2000). The North Atlantic Oscillation. *Stoch. Env. Res. Risk Assess.*, 14:213–242.

Green, A. P., Butler, K. T., and Buckley, A. R. (2013). Tuning of the emission energy of fluorophores using solid state solvation for efficient luminescent solar concentrators. *App. Phys. Lett.*, 102:133501.

Hanna, E., Cappelen, J., Allan, R., Jonsson, T., le Blancq, F., Lillington, T., and Hickey, K. (2008). New insights into North European and North Atlantic surface pressure variability, storminess and related climatic change since 1830. *Journal of Climate*, 21(24):6739–6766.

Hathaway, D. H. (2012). The solar wind. Available from http://solarscience.msfc.nasa.gov/SolarWind.shtml.

HEMI (2000). *The Solar Analyst 1.0 User Manual Draft.*

Hofierka, J. and Kanuk, J. (2009). Assessment of photovoltaic potential in urban areas using open source solar radiation tools. *Renewable Energy*, 34:2206–2214.

Hofierka, J. and Zlocha, M. (2012). A New 3-D Solar Radiation Model for 3-D City Models. *Transactions in GIS*, 16(5):681–690.

Huld, T., Muller, R., and Gambardella, A. (2010). Integrating CM SAF data with PVGIS for Estimation of Solar Energy System Performance. *JRC*.

Hurrell, J. (2013). Hurrell North Atlantic Oscillation (NAO) Index (PC-based). Available from `https://climatedataguide.ucar.edu/climate-data/hurrell-north-atlantic-oscillation-nao-index-pc-based`.

Hurrell, J. W. (1995). Decadal trends in the North Atlantic Oscillation: Regional temperatures and precipitation. 269:676–679.

Hurrell, J. W., Kushnir, Y., Ottersen, G., and Visbeck, M. (2003). An Overview of the North Atlantic Oscillation, in "The North Atlantic Oscillation: Climatic Significance and Environmental Impact". *Geophysical Monograph*, 134.

Ineichen, P. (2008). Comparison and validation of three global-to-beam irradiance models against ground measurements. *Solar Energy*, 82:501–512.

IPCC (2001). Natural Climate Variations - Natural Forcing of the Climate System. Available from `http://www.ipcc.ch/ipccreports/tar/wg1/041.htm`.

IPCC (2013). Solar Forcing of Climate. Available from `http://www.grida.no/publications/other/ipcc%5Ftar/?src=/climate/ipcc_tar/wg1/244.htm`.

Jäger-Waldau, A. (2007). Photovoltaics and renewable energies in europe. *Renewable and Sustainable Energy Reviews*, 11:1414–1437.

Jerez, S., Trigo, R. M., Vicente-Serrano, S. M., Pozo-Vázquez, D., Lorente-Plazas, R., Lorenzo-Lacruz, J., Santos-Alamillos, F., and Montávez, J. P. (2013). The Impact

of the North Atlantic Oscillation on Renewable Energy Resources in Southwestern Europe. *Journal of Applied Meteorology and Climatology*, 52(10):2204–2225. doi: 10.1175/JAMC-D-12-0257.1.

Kano, M. (1964). *Effect of a Turbid Layer on Radiation Emerging from a Planetary Atmosphere*. PhD thesis, University of California, Los Angeles.

Kasarova, S. N., Sultanova, N. G., Ivanov, C. D., and Nikolov, I. D. (2007). Analysis of the dispersion of optical plastic materials. *Optical Materials*, 29(11):1481–1490.

Kiehl, J. T. and Trenberth, K. E. (1997). Earth's Annual Global Mean Energy Budget. *Bulletin of the American Meteorological Societsy*, 78(2):197–208.

Klein, S. A. (1976). Calculation of monthly average insolation on tilted surfaces. *Solar Energy*, 19:325–329.

Klein, S. A. (1977). Calculation of monthly average insolation on tilted surfaces. *Solar Energy*, 19(4):325.

Koepke, P., Hess, M., Schult, I., and Shettle, E. P. (1997). Global aerosol dataset. *Report N 243, Max-Plank-Institut fur Meteorologie*, page 44.

Kristjánsson, J. E., Kristiansen, J., and Kaas, E. (2003). Solar activity, cosmic rays, clouds and climate – an update. *Advances in Space Research*, 34:407–415.

Lang, K. R. (1995). *Sun, Earth and Sky*. Springer, 4 edition.

Lang, K. R. (2005). *The Sun from Space*. Number 67-69. Springer.

Laungrungthip, N., McKinnon, A., Churcher, C., and Unsworth, K. (2010). *Sky detection in images for solar exposure prediction*. LAP Lambert Academic Publishing.

Liepert, B. and Tegen, I. (2002). Multidecadal solar radiation trends in the United States and Germany and direct tropospheric aerosol forcing. *Journal of Geophysical Research*, 107:41–53.

Liu, B. Y. H. and Jordan, R. C. (1960). The interrelationship and characteristic distribution of direct, diffuse and total solar radiation. *Solar Energy*, 4(3):1–19.

Liu, B. Y. H. and Jordan, R. C. (1962). Daily insolation on surfaces tilted toward the equator. *Trans. ASHRAE*, pages 526–541.

Lorenzo, E., Navarte, L., and Muñoz, J. (2011). Tracking and back-tracking. *Prog. Photovolt: Res. Appl.*, 19:747–753.

Majewski, D., Liermann, D., Prohl, P., Ritter, B., Buchhold, M., Hanisch, T., Paul, G., Wergen, W., and Baumgardner, J. (2002). The Operational Global Icosahedral–Hexagonal Gridpoint Model GME: Description and High-Resolution Tests. *Monthly Weather Review*, 130(319).

Mayes, J. and Wheeler, D. (1997). *Regional Climates of the British Isles*. Routledge. 390 pp.

McIntosh, K. R., Yamada, N., and Richards, B. S. (2007). Theoretical comparison of cylindrical and square-planar luminescent solar concentrators. *Applied Physics B: Lasers and Optics*, 88(2):285–290.

Melo, E. G., Almeida, M. P., Zilles, R., and Grimoni, J. A. B. (2013). Using a shading matrix to estimate the shading factor and the irradiation in a three-dimensional model of a receiving surface in an urban environment. *Solar Energy*, 92:15–25.

Mena-Chalco, J. P. (2010). Ray/box Intersection. Available from http://www.mathworks.co.uk/matlabcentral/fileexchange/26834-raybox-intersection.

Mercado, L. M., Bellouin, N., Sitch, S., Boucher, O., Huntingford, C., Wild, M., and Cox, P. M. (2009). Impact of changes in diffuse radiation on the global land carbon sink. *Nature*, 458:1014–1018.

Mestel, L. (1984). Solar magneto-hydrodynamics. *American Scientist*, 72(3):289–290.

Mueller, R. W., Matsoukas, C., Behr, H. D., Gratzki, A., and Hollmann, R. (2009). MAGIC - The CM-SAF operational scheme for the satellite based retrieval of solar surface irradiance - a LUT based eigenvector hybrid approach. *Remote Sensing of Environment*, 113:1012–1024.

Müller, R. W. and Trentmann, J. (2010). Algorithm Theoretical Baseline Document Direct Irradiance at Surface. pages 7–11.

Muneer, T. (2004). *Solar radiation and daylight models.* Number pp. 165. Elsevier Butterworth-Heinemann.

Murphy, J. M., Sexton, D. M. H., Jenkins, G. J., Boorman, P. M., Booth, B. B. B., Brown, C. C., Clark, R. T., Collins, M., Harris, G. R., Kendon, E. J., Betts, R. A., Brown, S. J., Howard, T. P., Humphrey, K. A., McCarthy, M. P., McDonald, R. E., Stephens, A., Wallace, C., Warren, R., Wilby, R., and Wood, R. A. (2009). UK Climate Projections Science Report: Climate change projections. Technical report, Met Office Hadley Centre, Exeter.

Myers, D. R. (2003). Solar radiation modelling and measurements for renewable energy applications: data and model quality. Technical report, National Renewable Energy Laboratory.

Myers, D. R., Emery, K. A., and Stoffel, T. L. (1989). Uncertainty Estimates for Global Solar Irradiance Measurements Used to Evaluate PV Device Performance. *Solar Cells*, 27:455–464.

Navarte, L. and Lorenzo, E. (2008). Tracking and ground cover ratio. *Prog. Photovolt: Res. Appl.*, 16:703–714.

Nguyen, H. T. and Pearce, J. M. (2012). Incorporating shading losses in solar photovoltaic potential assessment at the municipal scale. *Solar Energy*, 86:1245–1260.

177

NOAA (2014). The first climate model. Available from `http://celebrating200years.noaa.gov/breakthroughs/climate_model/welcome.html`.

Noorian, A. M., Moradi, I., and Kamali, G. A. (2008). Evaluation of 12 models to estimate hourly diffuse irradiation on inclined surfaces. *Renewable Energy*, 33:1406–1412.

Omer, S. (2009-2010). Introduction to weather data resources. Handouts for Nottingham Uni. MSc.

OpenCV (2013). Opencv (open source computer vision). Available from `http://opencv.org`.

Orgill, J. F. and Hollands, K. G. (1977). Correlation equation for hourly diffuse radiation fraction on a horizontal surface. *Solar Energy*, 19(4):357–359.

Orioli, A. and Gangi, A. D. (2012). An improved photographic method to estimate the shading effect of obstructions. *Solar Energy*, 86:3470–3488.

Page, J. K. (1961). The estimation of monthly mean values of daily total short-wave radiation on vertical and inclined surfaces from sunshine records for latitudes 40n-40s. *Proc. UN Conf. on New Sources of Energy*, 35(5):98.

Pearce, J. M. (2002). Photovoltaics - a Path to Sustainable Futures. *Futures*, 34(7):663–674.

Perez, R., Ineichen, P., Seals, R., Michalsky, J., and Stewart, R. (1990a). Modeling daylight availability and irradiance components from direct and global irradiance. *Solar Energy*, 44(5):271–289.

Perez, R., Ineichen, P., Stewart, R., and Menicucci, D. (1987). A new simplified version of the Perez diffuse irradiance model for tilted surfaces. *Solar Energy*, 39:221–231.

Perez, R., Seals, R., Zelenka, A., and Ineichen, P. (1990b). Climatic evaluation of models that predict hourly direct irradiance from hourly global irradiance: prospects for performance improvements. *Solar Energy*, 44(2):99–108.

Perpinan, O. (2012). Cost of energy and mutual shadow in a 2-axis tracking pv system. *Renew. Energy*, 43:331–342.

Polyanskiy, M. (2013). Refractive index database. Available from `http://refractiveindex.info`.

Pozo-Vázquez, D., Tovar-Pescador, J., Gamiz-Fortis, R., Esteban-Parra, M. J., and Castro-Diez, Y. (2004). NAO and solar radiation variability in the European North Atlantic region. *Geophysical Research Letters*, 31:L05201.

Previdi, M. and Veron, D. E. (2007). North Atlantic cloud cover response to the North Atlantic oscillation and relationship to surface temperature changes. *Journal of Geophysical Research: Atmospheres*, 112:D07104.

Prior, J. and Tempest, S. (2010). *The Met Office Book of the British Weather*. Met Office David and Charles.

PVGIS (2010). Pvgis radiation databases. Available from `http://re.jrc.ec.europa.eu/pvgis/apps4/databasehelp_en.html`.

PVGIS (2012). Solar radiation model r.sun and its implementation in GRASS GIS. Available from `http://re.jrc.ec.europa.eu/pvgis/solres/solmod3.htm`.

PV*Sol (2013). Software for Photovoltaics. Available from `http://www.solardesign.co.uk/pv.php`.

PVSYST (2013). PVsyst 6 Help. Available from `http://files.pvsyst.com/help/index.html`.

Quaschning, V. and Hanitsch, R. (1998). Irradiance calculation on shaded surfaces. *Solar Energy*, 62:365–375.

Ramanathan, V., Crutzen, P., Kiehl, J., and Rosenfeld, D. (2001). Aerosols, climate and the hydrological cycle. *Science*, 294(5549):2119–2124.

Reames, D. V., Tylka, A. J., and Chee, K. N. (2001). Solar Energetic Particles and Space Weather. *Space Technology and Applications Internaltional Forum*.

Redweik, P., Catita, C., and Brito, M. (2013). Solar energy potential on roofs and facades in an urban landscape. *Solar Energy*, 97:332–341.

Rehman, S. (1999). Empirical model development and comparison with existing correlations. *Applied energy*, 64:369–378.

Reindl, D. T., Beckman, W. A., and Duffie, J. A. (1990). Diffuse fraction correlations. *Solar Energy*, 45:1–7.

REN21 (2010). Renewable 2010 Global Status Report.

Rowan, B. C., Wilson, L. R., and Richards, B. S. (2008). Advanced material concepts for luminescent solar concentrators. *IEEE Journal of selected topics in quantum electronics*, 14(5):1312–1322.

Sanchez-Lorenzo, A., Calbó, J., and Martin-Vide, J. (2008). Spatial and Temporal Trends in Sunshine Duration over Western Europe (1938-2004). *Journal of Climate*, 21:6089–6098.

Shirley, P., Gleicher, M., Marschner, S., Reinhard, E., Sung, K., Thompson, W., and Willemsen, P. (2005). *Fundamentals of Computer Graphics*. A K Peters, Ltd.

Sloof, L., Bende, E., Burgers, T., Budel, T., Pravettoni, M., Kenny, R., Dunlop, E., and Büchtemann, A. (2008). A luminescent solar concentrator with 7.1efficiency. *Phsy. Stat. Sol. Rapid Res. Lett.*, 2:257–259.

Smestad, G., Ries, H., Winston, R., and Yablonovitch, E. (1990). The thermodynamic limits of light concentrators. *Solar Energy Materials*, 21:99–111.

Soti, R., Farkas, E., Hilbert, M., Farkas, Z., and Ketskemety, I. (1996). Photon transport in luminescent solar concentrators. *Journal of Luminescent*, 68:105–114.

Steven, M. D. and Unsworth, M. H. (1980). Shade-ring corrections for pyranometer measurements of diffuse solar radiation from cloudless skies. *Quart. J. R. Met. Soc.*, 106:865–872.

Swanson, R. M. (2009). Photovoltaics Power Up. *Science*, 324(5929):891–892.

The Sheffield Solar Farm (2013). The Sheffield Solar Farm. Available from `http://www.sheffieldsolarfarm.group.shef.ac.uk`.

Trigo, R. M., Osborn, T. J., and Corte-Real, J. M. (2002). The North Atlantic Oscillation influence on Europe: climate impacts and associated physical mechanisms. *Climate Research*, 20:9–17.

UK Meteorological Office (2006). MIDAS Land Surface Stations data (1853-current). Available from `http://badc.nerc.ac.uk/view/badc.nerc.ac.uk__ATOM__dataent_ukmo-midas`.

UK Meteorological Office (2011). Met Office Pyranometer. Available from `http://badc.nerc.ac.uk/view/badc.nerc.ac.uk__ATOM__dpt_11694844581612671`.

UK Meteorological Office (2012a). Met Office Integrated Data Archive System (MIDAS) Land and Marine Surface Stations Data (1853-current), [Internet].NCAS British Atmospheric Data Centre. Available from `http://badc.nerc.ac.uk/view/badc.nerc.ac.uk__ATOM__dataent_ukmo-midas`.

UK Meteorological Office (2012b). Met Office Surface Data Users Guide. Available from `http://badc.nerc.ac.uk/data/ukmo-midas/ukmo_guide.html`.

UK Meteorological Office (2013). National Meteorological Library and Archive Fact sheet 17 - Weather observations over land. Available from `http://www.metoffice.gov.uk/learning/library/publications/factsheets`.

van Sark, W. G. J. H. M., Barnham, K. W. J., Slooff, L. H., Chatten, A. J., Büchtemann, A., Meyer, A., McCormack, S. J., Koole, R., Farrell, D. J., Bose, R., Bende, E. E., Burgers, A. R., Budel, T., Quilitz, J., Kennedy, M., Meyer, T., Donegá, C. D. M., Meijerink, A., and Vanmaekelbergh, D. (2008). Luminescent Solar Concentrators – A review of recent results. *Opt. Exp.*, 16(26):21773–21792.

Šuri, M. and Hofierka, J. (2004). A New GIS-based Solar Radiation Model and Its Application to Photovoltaic Assessments. *Transactions in GIS*, 8:175–190.

Wang, Y., Colantuono, G., Green, A. P., Erdélyi, R., and Hanna, E. (2014a). Numerical spectral-based simulation of rectangular and cylindrical 2-layer luminescent solar concentrators. being submitted.

Wang, Y., Erdélyi, R., Hanna, E., and Colantuono, G. (2014b). Development of smart phone application to estimate the shading effect of obstacles. in review.

Wang, Y., Hanna, E., and Erdélyi, R. (2014c). Global and diffuse radiation and climate change. in review.

Weber, W. H. and Lambe, J. (1976). Luminescent greenhouse collector for solar concentrator prototypes. *Applied Optics*, 15(10):2299–2300.

Wells, C. V. (1992). Measurement Uncertainty Analysis Techniques Applied to PV Performance Measurements, Proceedings Photovoltaic Performance and Reliability Workshop. Technical report, National Renewable Energy Laboratory.

Woollings, T. (2010). Dynamical influences on european climate: an uncertain future. *Phil. Trans. R. Soc. A*, 368:3733–3756.

Yoo, S. H. (2011). Simulation for an optimal application of BIPV through parameter variation. *Solar Energy*, 85:1291–1301.

Young, D. R. and Smith, W. K. (1983). Effect of Cloud cover on Photosynthesis

and Transpiration in the Subalpine Understory Species Arnica Latifolia. *Ecological Society of America*, 64(4):681–687.

Zell, H. (2013). Solar storm and space weather. Available from `http://www.nasa.gov/mission_pages/sunearth/spaceweather/#q13`.

Zhai, L., Platt, T., Tang, C., Sathyendranath, S., and Walne, A. (2013). The response of phytoplankton to climate variability associated with the North Atlantic Oscillation. *Deep Sea Research Part II: Topical Studies in Oceanography*, 93(0):159–168.